Synthesis and Thermodynamic Investigation of Boron Allotropes

by

Anthony B. Cerqueira

Submitted in partial fulfilment of the requirements

for the degree of Master of Science

at

Dalhousie University

Halifax, Nova Scotia

August 2011

DALHOUSIE UNIVERSITY

DEPARTMENT OF CHEMISTRY

The undersigned hereby certify that they have read and recommend to the Faculty of Graduate Studies for acceptance a thesis entitled "Synthesis and Thermodynamic Investigation of Boron Allotropes" by Anthony B. Cerqueira in partial fulfilment of the requirements for the degree of Master of Science.

Dated: 26 August, 2011

Supervisor: _____

Readers: _____

_____

_____

DALHOUSIE UNIVERSITY

DATE: 26 August, 2011

AUTHOR: Anthony B. Cerqueira

TITLE: Synthesis and Thermodynamic Investigation of Boron Allotropes

DEPARTMENT OR SCHOOL: Chemistry

DEGREE: M.Sc. CONVOCATION: October YEAR: 2011

_____

Signature of Author

For Family, Foxes and Friends.

When you have eliminated the impossible,

whatever remains,

however improbable,

must be the truth.

- *Sherlock Holmes*

Table of Contents

Index of Tables

Index of Figures

Abstract

The focus of the present research is to find the relative thermodynamic stability of α-boron and β-boron via heat capacity measurements. Efforts to synthesize α-boron through the application of vapour-liquid-solid theory resulted in the discovery of a new chemical vapour deposition approach. The heat capacities of both synthesized α-boron and commercial (99.5%) β-boron were determined using relaxation calorimetry over the temperature range 0.2 K to 400 K. These data, in combination with literature information, allowed the calculation of the Gibbs energy of the α-boron to β-boron transition from 0 K to 1985 K. It was found that the transition from α-boron to β-boron was thermodynamically favourable at all temperatures up to 1985 K with a value of $\Delta G_t(T = 300\text{ K}) = -10\text{ kJ mol}^{-1} \pm 1\text{ kJ mol}^{-1}$ and $\Delta G_t(T = 1985\text{ K}) = -15\text{ kJ mol}^{-1} \pm 1\text{ kJ mol}^{-1}$.

List of Abbreviations and Symbols Used

AC - adiabatic calorimetry

CFS – Cold Field Source

CVD - chemical vapour deposition

EDS – energy dispersive spectrometry

IRM - Institute for Research and Materials at Dalhousie University

POS – partially occupied sites

PPMS- physical property measurement system from Quantum Design

RC - relaxation calorimetry

SEM - scanning electron microscopy

SDD – silicon drift detector

VLS – Vapour-liquid-solid synthesis

XRD - X-Ray Diffraction

2c2e – two-centre, 2 electron bond

2c3e – two-centre, 3 electron bond

3N, 4N & 5N – reagent purity, 99.9, 99.99, 99.999 respectively

A, B – constants for the physical property measurement system

B_{10} unit - β-rhombohedral boron bridging lattice structure

B_{12} unit – α-Boron lattice structure

B_{84} unit - β-rhombohedral boron lattice structure

C – heat capacity

C_e – eutectic composition point

C_P – heat capacity at a constant pressure

C_V – heat capacity at a constant volume

d - interplanar spacing

G - Gibbs energy, thermodynamic stability

H - enthalpy

J – Molecular flux of gas molecules in a chemical vapour deposition system

M - molar mass

n - gas density of a chemical vapour deposition system

N - number of molecules in a chemical vapour deposition system

p - Pressure

P – Power applied to physical property measurement system

R - ideal gas constant

S - entropy

$S_t\ (T=0)$ – transition entropy at 0 K

S_α – entropy of α-Boron from 0 K to some higher temperature

S_β – entropy of β-Boron from 0 K to some higher temperature

T – temperature in K

T_0 – Temperature of heat sink

T_1 – initial temperature

T_2 – final temperature

T_e – eutectic temperature point

U – internal energy

$\boldsymbol{v}$ - absolute value of the velocity vector

V - Volume

$\boldsymbol{v_m}$ - mean velocity

α_l - coefficient of thermal expansion

β_T - isothermal compressibility

$\Delta G_t(T)$ – Gibbs energy of transition with respect to temperature

ΔH – change in enthalpy

$\Delta H_t\ (T=0)$ – transition enthalpy at 0 K

$\Delta H_t\ (T=x)$ – enthalpy change due to the transition of α-boron to β-boron at some characteristic temperature

$\Delta H_t(T)$ – enthalpy of transition with respect to temperature

ΔH_α – enthalpy of α-Boron from 0 K to some higher temperature

ΔH_β – enthalpy of β-Boron from 0 K to some higher temperature

δq_{rev} – infinitesimally small quantity of reversibly transferred heat

ΔS – change in entropy

$\Delta S_t(T)$ – entropy of transition with respect to temperature

δT – change in temperature

θ - x-ray diffraction angle

λ - x-ray wavelength

τ_1 and τ_2 - time constant ratio for the heat capacitance to the thermal conductance of the sample and platform respectively

δU – change in internal energy

Ω – number of entropic microstates

Acknowledgements

First and foremost I would like to acknowledge and thank my supervisor, Prof. Mary Anne White for her help, support, and guidance during my time at Dalhousie University. I would like to thank past and present members of the M.A. White research group and auxiliary staff who have always been supportive of my research efforts: Kimberly Miller, Andrew Ritchie, Alex Bourque, Louis Desgrosseilliers, Carl Romao, and Dr. Ran Chen. A special thanks to Dr. Cathy Whitman and Michel Johnson whose insight and tireless efforts were invaluable.

The synthetic and XRD characterization work on α-boron would not have been possible without the experience and care of Andrew George.

Translation of the work by Machaldze in Georgian was thanks to Dr. Elena Smirnova and the Russian work of Naumov by Dr. Alexey Tikhomirov.

Financial support for this research came from the Dalhousie University Department of Chemistry, and NSERC.

Chapter 1 Introduction

Despite widespread use, many important details concerning boron are relatively unknown. Most summaries found in textbooks list the element as a black semiconductor, possessing nonmetallic nature and three valence electrons. More extensive literature surveys reveal an element still surrounded in mystery more than 200 years after its discovery despite the dedicated efforts of many researchers[1] and an international conference devoted to it since 1959.[2] The uncertainty around boron includes structural complexity, unverified polymorph thermodynamics, and unexpected bonding arrangements.[3] The frontiers of boron research remain open to exploration and the present work is directed to understanding the thermodynamic stability of the key allotropes: α-boron and β-boron.

1.1 History of Boron Research

Boron was discovered in 1808 by two competing groups. French researchers Louis Jacques Thênard and Louis Joseph Gay-Lussac[4] made the claim of discovery first, but their rival Humphrey Davy[5] from England was only days behind. Subsequent analysis by Henri Moissan[6], 87 years later, showed that neither group had actually prepared pure boron, as both samples had more than 50% impurities. It took over 100 years since the 'discovery', in 1909, for boron of relatively high purity to be prepared with confidence.[7] Once the existence of the element was established, research turned to cataloguing the

polymorphs or allotropes, although early researchers were unaware that boron was not yet available in a high purity.

Allotropism is an elemental property which describes the ability of an element to exist in multiple structural forms, *i.e.*, to exhibit polymorphism. These forms are still pure elemental constructs but the difference in bonding arrangements can have significant effects on the properties of each allotrope. For instance, diamond and graphite are both allotropes of carbon, with one being extremely hard, and the other soft enough for use in writing.

Allotrope research concerning boron proved to be of equal complexity and misdiscovery as the original element synthesis. The first effort to find polymorphs in 1857 by Friedrich Wohler and Henri Sainte-Claire Deville[8,9] resulted in three possibilities, all of which were later studied by Moissan and found to be compounds.[1] In the 1950s Laubengayer *et al.* of Cornell University and General Electric discovered the so-called *I*-tetragonal phase[10], but as will be explained in more detail below, this proved to be a compound also.[11] Successful polymorph synthesis was finally achieved and verified in 1957 with the fabrication of β-boron, an extremely complex structure that remained uncharacterized for seven years after its discovery.[12] In 1958 McCarty *et al.*[13] of General Electric discovered the α-boron phase and although it was understood readily, the unique icosahedral structure was novel. *II*-tetragonal boron was synthesized by Claude Talley of the Polytechnical Institute of Brooklyn in 1960[14], and remained structurally unidentified due to its complexity for another 19 years.[1] The most recent addition to the polymorph picture was in 2006 with the synthesis and characterization of the high pressure phase γ-

boron[15] bringing the total characterized forms to four. In the proceeding sections these four polymorphs will be explored in more detail.

When it comes to thermodynamic research concerning boron, the previous 30 years have been marked with uncertainty.[3] Experimental investigation indicated that α-boron irreversibly transforms into β-boron above a range of temperatures such as 1913 K[16] or 1985 K[17] via three metastable phases. Other works suggest that the transition remains thermodynamically favourable at lower temperatures and instead kinetics interfere.[18] Computational modelling has been similarly conflicted, with no consensus on the ground states of α and β-boron.[15,18,19,20,21,22] The confusion around boron in computational work stems from its novel properties and still uncertain characterization. Consideration of the literature shows the unit cell of β-boron has undergone multiple structural assignments,[18] with the most current introducing partially occupied sites (POS).[23] Similarly α-boron, despite the significantly simpler unit cell, possesses three-centre bonds,[24,25] and an electron count that would normally favour metallicity, but strong localization provokes insulating states.[15] Such factors as crystal structure, POS, bonding and electronic states have non-trivial effects on the results of computational studies. Thus some efforts reported α-boron more stable,[19,20] while others determined β-boron to be more stable.[15,18] Due to these problems, the aim of the current work has been experimental determination of phase stability, an avenue which has been limited in the past by the confluence of inadequate measurement resolution on available instruments and poor yielding synthetic methods resulting in low purity samples.[26] Advancements in relaxation calorimetry have opened the way for more precise measurement of small samples.

1.2 Boron Applications

Boron has an atomic mass of 10.811 amu and a density 2.34 g/cm^3. It is lighter than aluminium, and stronger than steel. It possesses a high melting point (2450 °C), is harder than corundum (9.5 on Moh's scale), and has a low volatility.[27] Despite these basic parameters, the systematic investigation of the properties of pure boron remains in its infancy.. The majority of known information can be found in Landolt-Bornstein, Non-Tetrahedrally Bonded Binary Compounds II: Supplement to Vol. III/17g.[28]

Boron and boron compounds have a wide range of applications resulting in approximately 100 tonnes of boron produced annually world wide.[3] Boron nitride, which possesses a graphite-like structure, is widely applied in heavy industry as a high temperature solid lubricant for tasks requiring chemical resistance.[29,30] Zirconium diboride is employed on space vehicles heat tiles because of the chemical inertness and thermal shock resistance.[31] Hafnium diboride possesses a strong neutron capture ability making it useful for nuclear power control rods.[32,33] Titanium diboride possesses high mechanical strength and is thus employed in wear resistant coatings.[34] Magnesium diboride displays an unusually high superconducting temperature (39 K) for a binary compound, which has found application in MRI.[35,36] Composites of aluminium and boron carbide are under consideration as construction materials.[3] Ferroboron, an alloy of iron and boron, hardens steel, while boron carbide is employed as coatings on prototype combat armour.[3] Boron oxide is used in Pyrex™ glassware, lowering the working temperature compared to pure quartz, adding mechanical strength and lowering the thermal expansion, while not

compromising the chemical inertness. Pure boron is employed as igniters in airbags, and reinforcement for materials that need strength without adding weight, such as airplane components.[3]

1.3 Boron Allotropes

Boron is thought to possess at least 16 different allotropes[20,18], although only four have been studied in any detail: α, β, γ and tetragonal. Amorphous boron subsists as a randomized collection of linked icosahedra possessing a brown colour. As it crystallizes, the α-phase orders the icosahedra into planes. Adding pressure transforms boron into the γ-phase, which introduces boron atoms within the plane spaces. The β-phase has a total structural rearrangement relative to α-phase; it is a complex form that is not easily depicted. The α,and β phases are rhombohedral, while γ-phase is orthorhombic, but there is possibly also a tetragonal form at high temperature;[3] this form is controversial.

To map fully the thermodynamic stability of all boron phases is a project beyond the scope of this work. Thus efforts here have been directed to the most likely candidates for stability at ambient conditions, α-boron and β-boron, which are explained in greater detail in the proceeding sections.

1.3.1 Amorphous boron

The amorphous form of boron is a brown solid lacking in any periodic long-range order. On the short range it consists of randomly oriented icosahedra, which are the

common sub-structural unit in crystalline boron. Opinions differ concerning which crystalline form the amorphous system is most like. Some propose α-rhombohedral boron[37] as the ideal, even going so far as to suggest the amorphous phase is nothing more than heavily faulted layered crystals[38] or micro crystals.[39] Other works point to the similarity between β-rhombohedral boron and short-range amorphous order, stating that they hold similar properties and often co-exist in deposition.[40] This lack of consensus is rooted in the synthetic product. In the proceeding sections it will be shown that preparation of each crystalline phase of boron requires varying synthetic conditions and the amorphous structure can mirror the circumstances employed to create it on small scale. For example, vapour deposition is shown to form micro crystals[39] while pyrolysis produces β-like forms.[40]

1.3.2 α-Boron

The α-rhombohedral boron allotrope has a reddish colour, belongs to the space group $R\bar{3}m$, with lattice parameters of $a = b = c = 5.057 \pm 0.003$ Å and $\alpha = \beta = \gamma = 58.06° \pm 0.05°$.[26] The unit cell has 12 atoms making a complete regular icosahedron as seen in Figure 1.1.[41] Conventionally called the 'B_{12}' unit in boron research, employing conventional methods to understand the electronic structure has each boron atom covalently bond with five nearest neighbours resulting in 10 valence electrons per vertex. The two-electron interpretation of covalency can be considered too simplistic for counting electrons in these polyhedra. A robust interpretation can be found by considering Wade's rules from the polyhedral skeletal electron pair theory.[1] According to Wade, a

complete, or *closo,* icosahedron requires cn+2 electrons for stabilization, with n as the number of vertices and c as the number of valence electrons per vertex. In a general case it can be shown that α-boron would require a total of 38 valence electrons for a closed-shell system, whereas an isolated boron icosahedron possesses only 36 valence electrons.

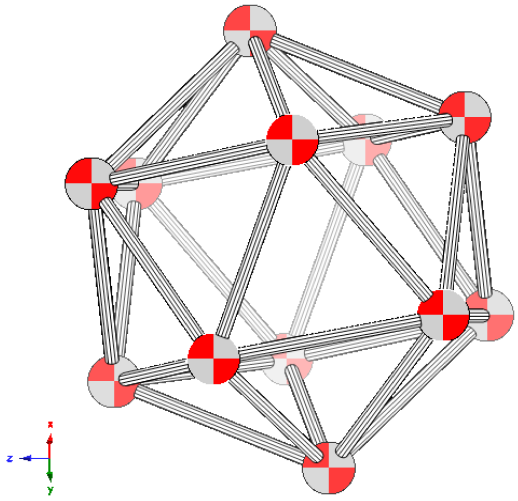

Figure 1.1: Contents of an α-boron unit cell constructed using parameters from Callmer.[44] All vertices are boron atoms. The displayed edges map out the geometric shape, but do not accurately represent the bonds. View is along the (1 1 1) direction.

To better understand the electronic system of α-boron, the work of Bullett[42] is depicted in Table 1.1 and can be summarized into three bond classes comprising 12 non-bonding, 13 bonding and 23 antibonding orbitals. As mentioned, ideal stability arises with the creation of a closed-shell system requiring a total of 38 electrons. The 13 bonding orbitals, representing intra-icosahedral bonding that forms the icosahedra, require 26 electrons. This leaves 10 electrons to fill 12 external covalent bonds. Six of these external bonds can be formed using the common approach to bonding resulting in six, two-

electron, two-centre bonds (2e2c) from one icosahedron to another along the *z* direction as seen in Figure 1.2. The final six bonds have only four electrons requiring an unconventional arrangement known as a two-electron, three-centre bond (2e3c) throughout the *xy* plane as depicted in Figure 1.3. Figure 1.4 depicts a cross-section of the total α-boron bonding system. Due to the third centre these atypical bonds result in the effective addition of two electrons to any one B_{12} unit closing the shell without disrupting Wade's rule.[43] These bonds are longer than the traditional links as shown by the bond lengths in Table 1.2, and at temperatures above 1500 K they increase the reactivity of α-boron.[42]

Table 1.1: Energy levels and molecular orbitals for a regular B_{12} icosahedron.[42]

Energy /eV	Degeneracy	Irreducible representation	Orbital component	Bonding character
13.9	3	T_{2u}	σ	Anti
12.7	5	V_g	Mixed	Anti
9.5	3	T_{1u}	Mixed	Anti
5.8	3	T_{1g}	π	Anti
3.5	5	V_u	π	Anti
1.1	4	U_g	π	Anti
-3.8	5	V_g	Mixed	Non
-4.7	3	T_{2u}	σ	Non
-4.8	3	T_{1u}	Mixed	Non
-6.6	4	U_u	π	Bonding
-8.1	1	S_g	σ	Non
-10.4	5	V_g	Mixed	Bonding
-14.9	3	T_{1u}	Mixed	Bonding
-23.2	1	S_g	σ	Bonding

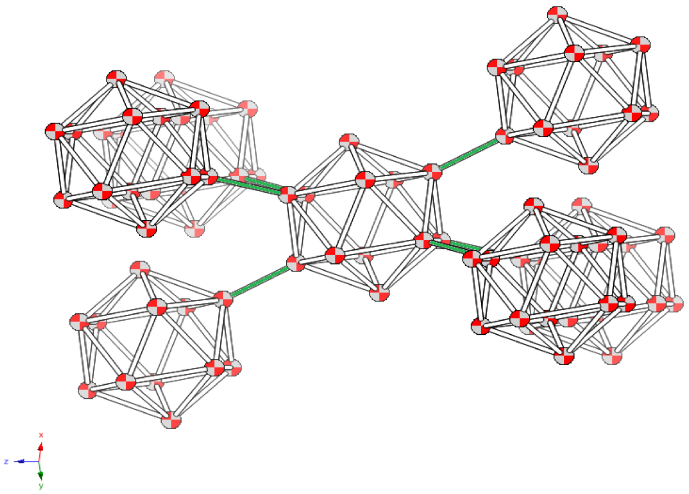

Figure 1.2: α-boron units bonded along the z-axis via two electron, two-centre bonds depicted in green. Construction parameters from Callmer.[44] Looking along (1 1 1) direction.

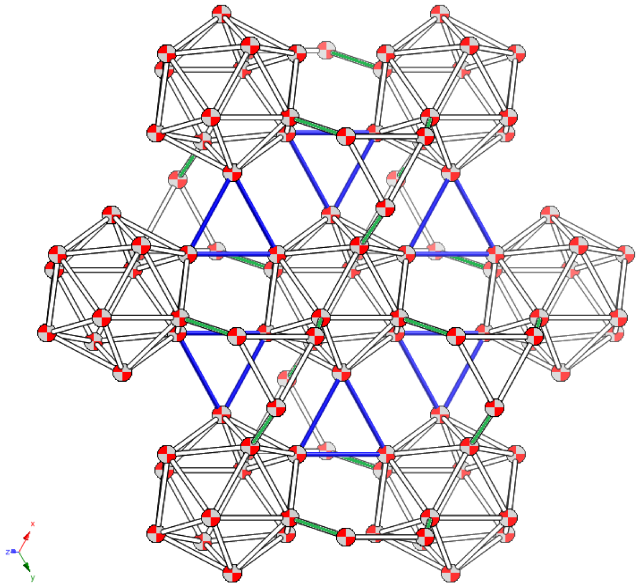

Figure 1.4: Combined image of two-centre (green) and three-centre (blue) bonds of α-boron. Construction parameters from Callmer.[44]

Bond Type	Bond Length /Å
Intra-Icosahedral	1.71
Inter-Icosahedral	1.73-1.79
Three-Centre Bonds	2.03

Table 1.2: α-boron bond lengths within and between icosahedra.[42]

1.3.3 β-Boron

The *β*-rhombohedral boron allotrope forms from *α*-boron at temperatures above 1913 K,[16] possesses a black metallic shine and although icosahedra still make the foundation of the structure, it is far more complex than *α*-boron. Current understanding places the unit cell with 106.66 atoms (discussed below in detail) in a rhombohedral arrangement with a space group of $R\bar{3}m$ and lattice constants of $a = b = c = 10.145$ Å and $\alpha = \beta = \gamma = 65.28°$.[15,20,43] Previous determinations listed 314.7 atoms for a hexagonal structure, with an identical space group and lattice constants of $a = b = 10.9251$ Å, $c = 23.8143$ Å.[44] The structure of *β*-boron leads to a complex array of features and minor structures that can be difficult to depict in a combined manner. To facilitate discussion the various parts of the structure will be broken down into a series of fragments.

While building a picture of the idealized *β*-boron unit cell, the root component remains the B_{12} unit seen in *α*-boron (Figure 1.1). Unlike *α*-boron, the icosahedra in *β*-boron are not arrayed in sheets, but instead are surrounded by 12 pentagonal pyramids.

The apex of each pyramid is bonded to one vertex of an icosahedron, making a larger structure known as the B_{84} unit which can be seen in Figure 1.5. Note the presence of the B_{12} in the centre and that the outer surface consists of one half of an icosahedron. Setting two B_{84} fragments in close proximity produces a bridging icosahedron. The size of the B_{84} unit limits such connections to six, leaving six further pentagonal pyramids in need of icosahedral completion. The introduction of a new structural fragment, depicted in Figure 1.7, and called B_{10}, acts as a bridging unit due to the arrangement of three pentagonal pyramids all sharing the same apex. The three pyramids form three more icosahedra on three adjacent B_{84} units, an example of which can be seen in Figure 1.8. The B_{10} fragments also act as a bridge out of the plane to another B_{10} through a single atom intermediary. Although composed of two B_{10} units, this inter-planar binding fragment is often called B_{57} and is used in some literature as the origin of the unit cell. The B_{57} unit can be seen in Figure 1.9 and is a composed of the previously listed structural fragments. Each B_{10}, providing 20 atoms, is bonded to 3 pentagonal pyramids from the B_{84} fragment forming 3 linked icosahedra and adding an extra 36 atoms.[24]

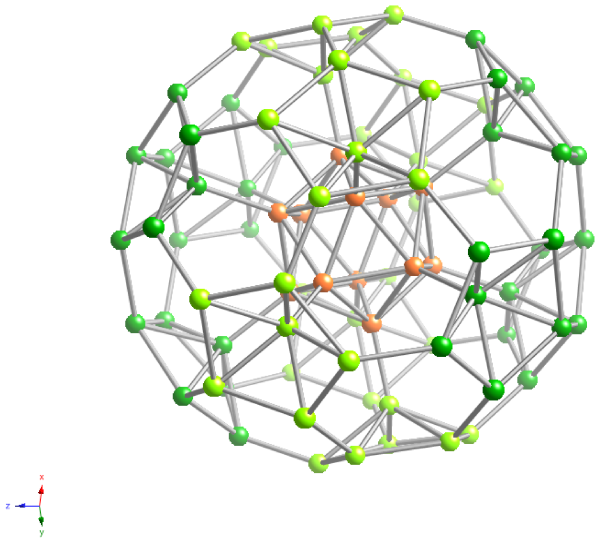

Figure 1.5: B_{84} unit of β-boron showing the central icosahedron (orange) surrounded by pentagonal pyramids (green). The apex of each pyramid is bonded to the central icosahedron. Constructed from parameters by Callmer.[44]

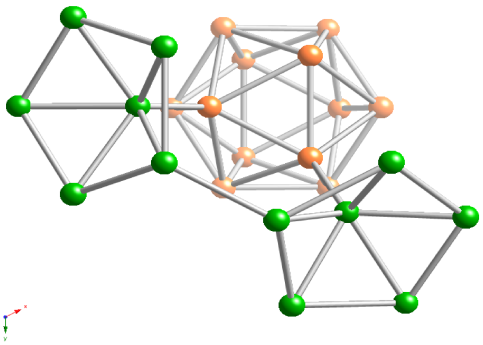

Figure 1.6: A fragment of the B_{84} unit of β-boron, shown in Figure 1.5 depicting two pentagonal pyramids (green) each with a bond to the central icosahedron (orange). Parameters for construction from Callmer.[44]

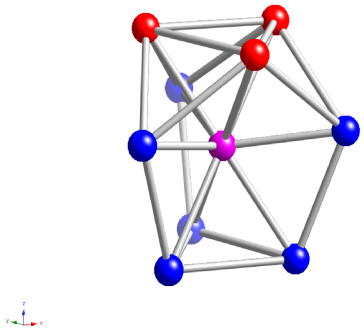

Figure 1.7: B_{10} unit of β-boron composed of three pentagonal pyramids all sharing the same apex (purple). The triangle made by the top three atoms (red) bonds to other B_{10} units via a one boron bridge not shown. Parameters for construction from Callmer.[44]

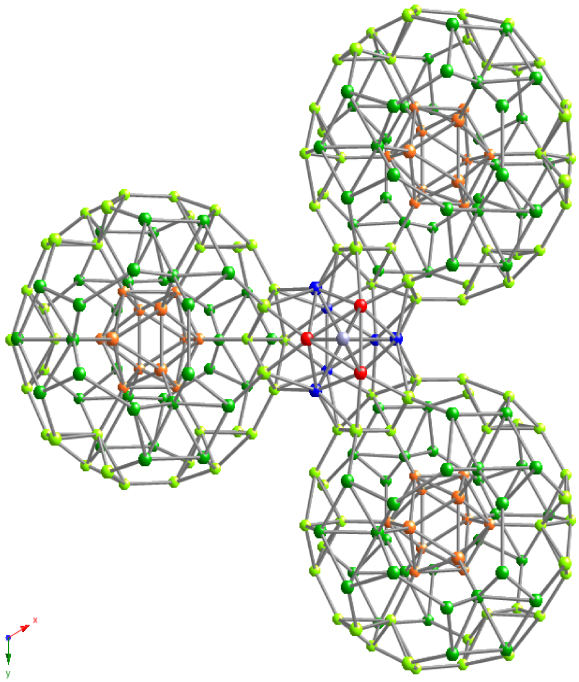

Figure 1.8: Three B_{84} units of β-boron bonded to a B_{10} unit of β-boron. Parameters for construction from Callmer.[44]

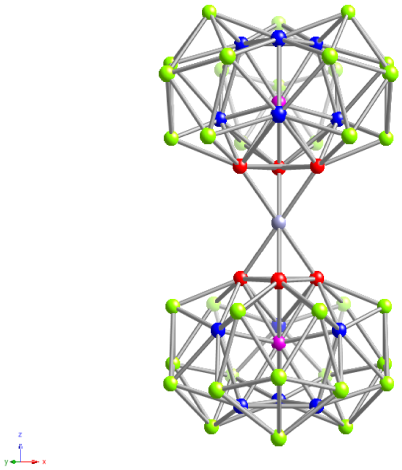

Figure 1.9: A B_{57} unit of β-boron made from bonding two B_{10} (red+ blue+ fushia) units along the z-axis and including some of the B_{84} pentagonal pyramids (green). Constructed from work by Callmer.[44]

The sum total of these structural fragments reveals a perfect rhombohedral unit cell of 105 atoms with an electron deficiency of five, and approximately 1.66 more boron atoms are needed to complete the electronic component. The resulting unit cell would break rhombohedral symmetry and increase the unit cell to 106.66. These additions introduce partially occupied sites (POS) to the structural picture, leading to points in the lattice with an amount of boron varying from unit cell to unit cell.

Current research remains conflicted on the nature, number and occupancy of these POS and resulting variations sit as the foundation of the computational uncertainty.[15,18,19,20] Leading theory employs the work of Slack *et al.*[45] who introduce a total of four POS which are depicted in Figure 1.10, Figure 1.11 and Figure 1.12. This is an addition to the two sites introduced earlier by Callmer[41] which are visible in Figure 1.10 and Figure 1.13.

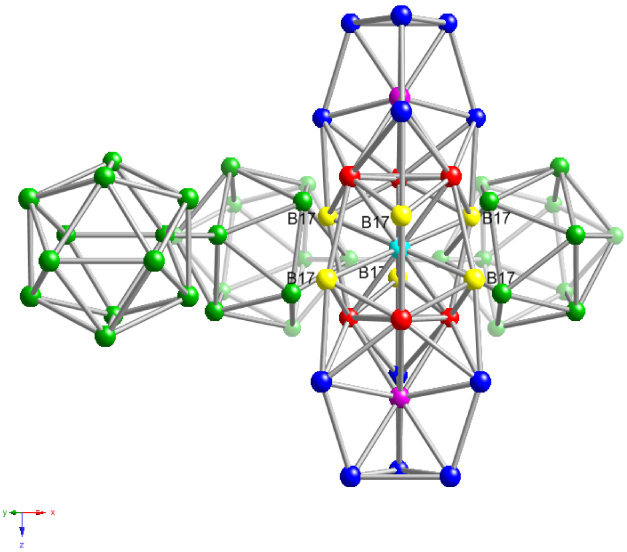

Figure 1.10: Image of two B_{10} units of β-boron with the Slack B17 POS displayed in yellow assisting in the gap bridging.[45] Callmer also lists the red sites as POS.[44]

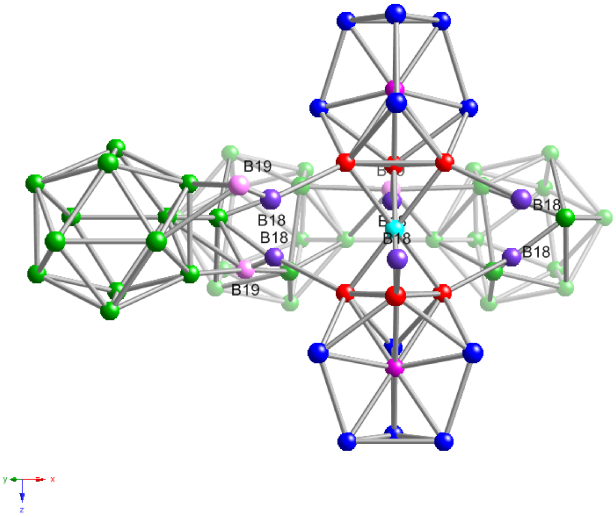

Figure 1.11: Image of two B_{10} units of β-boron with Slack B18 (purple) and B19 (pink) POS.[45]

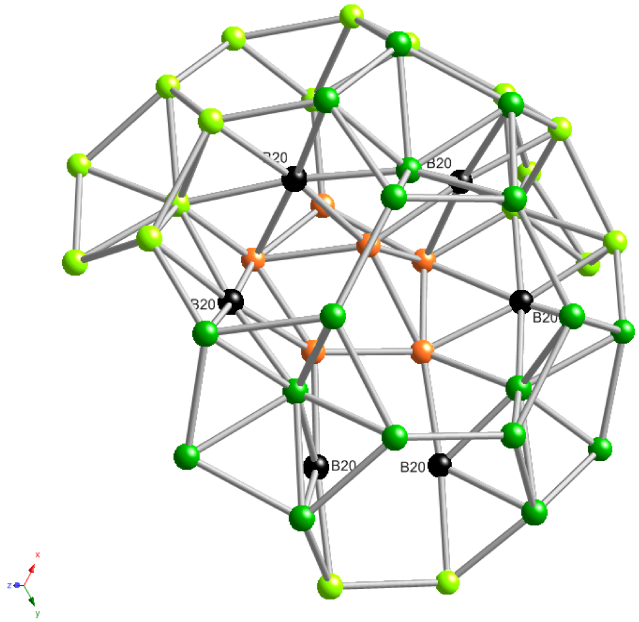

Figure 1.12: Image of B_{84} fragment of β-boron with the Slack B20 POS in black.[45]

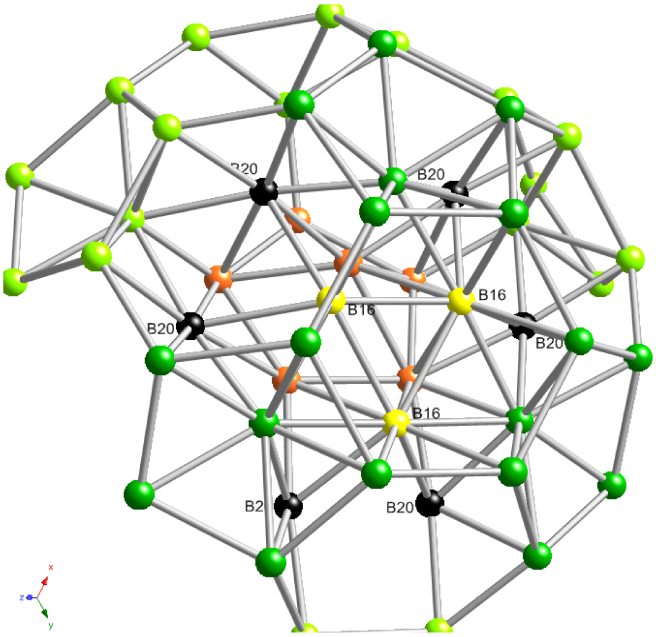

Figure 1.13: Image of B_{84} fragment with the Callmer[44] *B16 POS in yellow and the Slack*[45] *B20 POS in black.*

1.3.4 γ-Boron

The orthorhombic γ-boron phase was more recently discovered by Oganov *et al.*[15] It is formed from *β*-boron by applying 19 to 89 GPa of pressure at 1800 to 2450 K. The structure appears analogous to *α*-boron except for the addition of two interstitial boron atoms between the icosahedra. Despite the similarities to *α*-boron, the orthorhombic unit cell of γ-boron contains 28 atoms in the space group *Pnnm,* with lattice parameters of a = 5.043 Å, b = 5.612 Å, c = 6.921 Å and $\alpha = \beta = \gamma = 90°$.[15] Figures 1.14 and 1.15 depict the bonding of a pair of boron atoms (2B) with the neighbouring B_{12} units. These additions transform the lattice into an analogue of rock salt, with icosahedra acting as one component while the boron pairs are the other. Thus the pairs act as electron donors making γ-boron a 'boron boride' (B_2^+ B_{12}^-), giving the system a unique ionic character which is unexpected for an elemental solid. The present theory suggests high pressures and diffuse orbitals, of a quantity less than metallic character, triggers this oddity.[15]

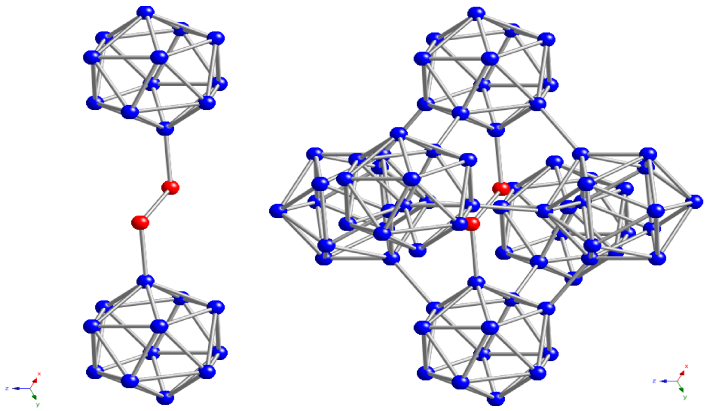

Figure 1.14: γ-boron bonding between B_{12} icosahedron (blue) and 2B pairs (red). Right image depicts full local bonding, left image a cross section for clarity. Constructed from parameters by Oganov.[15]

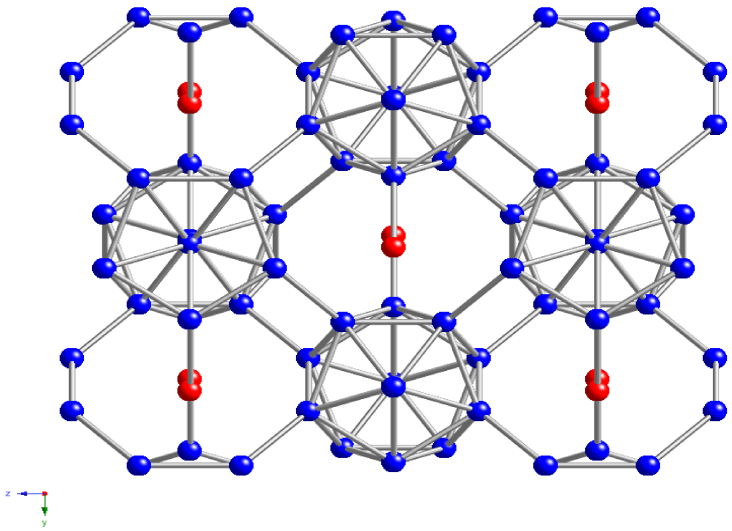

Figure 1.15: γ-boron lattice. Note the rock salt structure of repeating 2B (red) and B_{12} (blue) units. Constructed from parameters by Oganov.[15]

1.3.5 Tetragonal "Phase" of Boron

Early accounts of boron allotrope research[42,46] list two tetragonal forms called *α*-tetragonal and *β*-tetragonal or *I* and *II* respectively. Characterized in the late 1950s, *I*-tetragonal was considered the first known crystal form of boron and entered the literature as the eminent example of crystalline boron. Twenty years after *I*-tetragonal appeared in publications and textbooks, Amberger and Ploog demonstrated that the phase relied on impurities of C, N, or Be to provide stability, making it a compound.[1,3,]

Of the tetragonal phases only *II*-tetragonal is presently considered a pure boron allotrope, however there is still some controversy. First synthesized in 1960 by Talley[47] as a polycrystal, x-ray diffraction was used to derive the structure which revealed the space group $P4_122$ with lattice parameters of $a = b = 10.12$ Å, $c = 14.14$ Å and $\alpha = \beta = \gamma = 90°$

with a unit cell of 192 atoms. A single crystal was fabricated in 1978[47] but no subsequent attempts have yet been successful, leading to current researchers questioning the validity of *II*-tetragonal as an allotrope of boron.[3]

1.4 Aim

The goal of the present work is to determine the experimental thermodynamic stability of the main boron allotropes, α-boron and β-boron, by high-accuracy determination of the heat capacity of each allotrope.

Chapter 2 Background

2.1 Thermodynamic Theory

Thermodynamics remains a rigorous and exact branch of science uniting five fundamental properties of matter: volume, pressure, temperature, internal energy and entropy, through powerful equations. Because of this utility and elegance it is possible to use a handful of experimentally derived properties to describe the related thermal processes and predict results of interest to chemists, such as thermodynamic stability.

2.1.1 Thermodynamic Stability

In a general sense the stability of a material reflects the ability it has to retain a set of properties over time. For mundane considerations a stable chemical can exist in a given state until acted upon by external forces, while an unstable one will undergo a transformation until it becomes stable. This broad description is not the complete picture and chemists tend to consider chemical stability as a function of two characteristic forms: kinetic and thermodynamic.

Thermodynamic stability is the state where a chemical is in equilibrium with the surroundings, existing in the lowest possible energy state. Thermodynamically stable systems will exist *ad infinitum* unless the conditions are altered. Thermodynamic stability tells you if a reaction or physical process should occur for a given set of external

conditions.

Kinetic stability focuses on qualifying the ability of the system to change over time rather than the relative energy. Thus a kinetically stable system does not readily undergo a transition for a given set of conditions, but might.

These two forms of stability are not mutually exclusive, nor are they mutually inclusive. A system can be kinetically stable, while not being at the lowest possible energy state meaning a transition is favourable, but restricted. An example of such is the amorphous glassy state of $SiO_{2\,(s)}$. Upon cooling a liquid melt, it becomes energetically favourable to solidify to the lowest energy state, an ordered crystal. However if the system temperature cools too quickly, it restricts atomic movement, limiting the ability of the system to reach thermodynamic stability, halting the transition at the vitreous, kinetically favoured, state. Many chemical states are thermodynamically stable under a given set of conditions and kinetically stable once removed from them. Diamond is one such example, being thermodynamically stable at high temperatures and pressures, but kinetically stable with respect to graphite at standard state conditions.

The most important parameter for thermodynamic stability at constant temperature and pressure is known as Gibbs energy (G). Named after J. W. Gibbs, one of the founders of thermodynamics, the Gibbs energy is defined as:

$$G = H - ST \tag{2.1}$$

where H is the enthalpy, S is the entropy, and T is the temperature. In the simplest case,

the lower a system's Gibbs energy the more thermodynamically stable it is, at constant pressure (as for the experiments herein). However to find the Gibbs energy of a system using equation (2.1) requires knowledge of the three terms *H*, *S* and *T*.

2.1.2 Heat Capacity Overview

Heat capacity (*C*) is the rate of change in energy with respect to temperature. At constant volume it is defined as:

$$C_V = \left(\frac{\partial U}{\partial T} \right)_V \tag{2.2}$$

where *U* is the internal energy. At constant pressure the heat capacity is defined as:

$$C_P = \left(\frac{\partial H}{\partial T} \right)_P \quad . \tag{2.3}$$

2.1.3 Entropy from Heat Capacity

The concept of entropy is a measure of the internal disorder of a system at a given state. It is an extensive thermodynamic property, meaning the value is fundamentally linked to the quantity of material, and entropy is a state function, so that the change in entropy is independent of path. It is difficult to measure entropy directly, but due to the interrelated nature of thermodynamic properties it is possible to calculate the change in entropy via the heat capacity.[48] For instance if one considers the state function for the change in entropy (*dS*):

$$dS = \frac{\delta q_{rev}}{T} \tag{2.4}$$

where δq_{rev} is an infinitesimally small quantity of reversibly transferred heat, and T is the temperature in Kelvin. This relationship can be combined with the isobaric (constant pressure) temperature change:

$$\delta q_{rev} = C_p dT \quad , \tag{2.5}$$

to give an integral from which the entropy of a system can be derived from the heat capacity:

$$\Delta S = \int_{T_1}^{T_2} \frac{C_p}{T} dT \quad . \tag{2.6}$$

This relationship is further simplified by the third law of thermodynamics which says that the entropy of a perfect crystal is zero at zero Kelvin. The third law can be rationalized by two factors: first for any system at zero Kelvin, all thermal energy is removed; secondly a crystal with no defects, *i.e.* perfect, has no internal disorder once thermal energy is removed. Thus entropy can be considered zero at absolute zero for a perfect crystal.

As no sample is completely free of defects, it is an approximation to consider the current work to follow the third law. This approximation is considered valid due to the use of very high purity samples. The third law allows entropy to be quantified absolutely by setting T_1 as zero and integrating the experimental heat capacity via equation (2.6) to the temperature of interest, T_2.

2.1.4 Enthalpy from Heat Capacity

Enthalpy, *H*, represents the total heat content of a system in a given state at constant pressure. This energy includes the internal energy *(U),* which forms the system and the energy required to oppose the environment to establish a system's pressure and volume. Defined as:

$$H = U + pV \tag{2.7}$$

the enthalpy is also an extensive state function making it dependent on quantity of material in a state but not the path taken to any given state.

As C_P is defined in terms of enthalpy and temperature, as seen in equation (2.3), it is possible to derive the enthalpy of a system by integrating the heat capacity with respect to temperature at constant pressure, or:

$$\Delta H = \int_{T_1}^{T_2} C_p dT \quad . \tag{2.8}$$

2.1.5 Transition Stability

The goal of the current work is exploration of the transition between α-boron and β-boron for the purpose of mapping phase stability. This requires the calculation of the Gibbs energy of transition ($\Delta G_t(T)$) across the entire temperature profile. $\Delta G_t(T)$ is a

specific case of the general Gibbs relationship seen in equation (2.1) which compares the enthalpy and entropy of transition via:

$$\Delta G_t(T) = \Delta H_t(T) - T\Delta S_t(T) \quad . \tag{2.9}$$

The transition values of *G, H* and *S* represent the absolute difference between α-boron and β-boron along with the intrinsic energy needed for the transition or to put it more succinctly

$$\Delta H_t(T) = \Delta H_t(T=0) - \Delta H_\alpha + \Delta H_\beta \tag{2.10}$$

and

$$\Delta S_t(T) = \Delta S_t(T=0) - S_\alpha + S_\beta \quad . \tag{2.11}$$

The terms ΔH_α, ΔH_β and S_α, S_β are the enthalpies and entropies of each allotrope from 0 K to some higher temperature respectively, derived from the heat capacity via the theory outlined above. The terms ΔH_t *(T=0)* and ΔS_t *(T=0)* are the transition enthalpy and entropy at 0 K respectively. ΔS_t *(T=0)* is considered zero based on the third law of thermodynamics, although as will be discussed later it could be non-zero, but ΔH_t *(T=0)* must be calculated from a thermodynamic cycle.

2.1.6 Thermodynamic Cycle

A thermodynamic cycle, as seen in Figure 2.1, can be used to find the enthalpy and entropy of transition at 0 K through the relationships

$$\Delta H_t(T=0) = H_t(T=X) + \Delta H_\alpha - \Delta H_\beta \tag{2.12}$$

where H_t *(T=X)* is the enthalpy of the spontaneous transition from *α*-boron to *β*-boron at some characteristic temperature denoted by *X*.

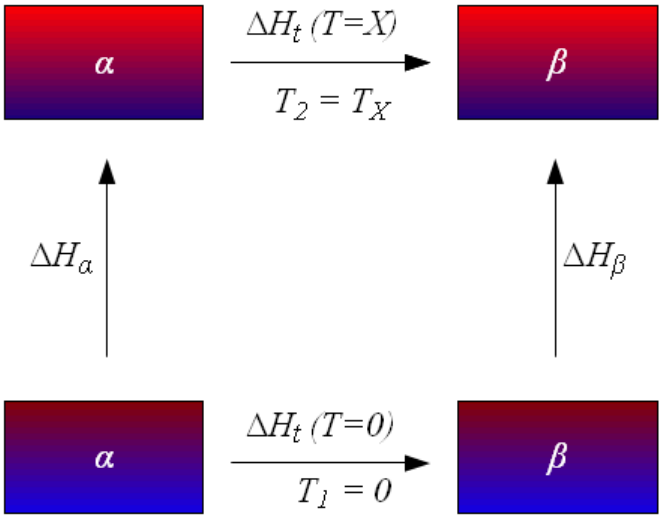

Figure 2.1: Thermodynamic cycle depicting the relationship between α-boron and β-boron enthalpy. T_1 is zero, and T_2 is some characteristic temperature, X, where α-boron transforms to β-boron. All of these terms are used in equation (2.12).

2.2 Synthetic Theory

Synthesis of boron was carried out by two methods: vapour-liquid-solid synthesis and chemical vapour deposition.

2.2.1 Vapour-Liquid-Solid Synthesis Overview

Vapour-liquid-solid synthesis (VLS) was first developed by W. C. Ellis and R. S. Wagner at Bell Telephone Laboratories in 1964. VLS extends the theory of solution

chemistry to temperatures and conditions beyond the ambient range. Working at very high temperatures and pressures, VLS still holds fundamental theoretical similarities to relatively basic reaction chemistry.[49] The fundamental component of VLS is the liquid/vapour interface which operates via binary phase diagrams.

Binary diagrams display the relationship between the concentration of two distinct substances and the temperature. The crucial aspect of binary diagrams for VLS synthesis is the formation of a eutectic, a concentration which depresses the melting temperature of the pure elements. The binary phase diagram shown in Figure 2.2 will be used to elaborate how the eutectic drives the fundamental mechanism of VLS.[50]

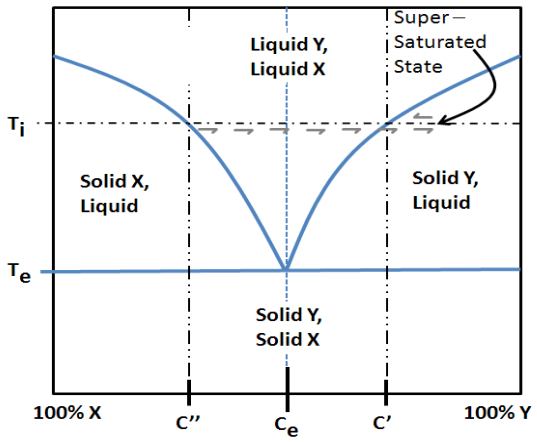

Figure 2.2: Simplified binary phase diagram of a two component generic system X & Y.

A binary phase diagram of the $X - Y$ system has a eutectic at composition C_e and temperature T_e. For VLS the system is held at some temperature T_i, above the eutectic temperature, where the eutectic composition will be totally liquid. The system, at temperature T_i, begins with a high percentage of component X resulting in a solid. Should component Y be introduced as a vapour it will deposit changing the composition of the

system to *C″*. At this composition the system will begin to transition from completely solid to completely liquid and component *Y* will begin to concentrate along the surface. As more component *Y* is introduced the concentration gradient of the system will encourage diffusion through the liquid to the solid below, increasing the overall concentration of component *Y* in the system. As the concentration of component *Y* increases, the system moves across the binary phase diagram from concentration *C″* to *C′*. Eventually the liquid will saturate with component *Y* resulting in an unstable system should more component *Y* be added via vapour deposition. Under these conditions the liquid will begin to precipitate component *Y* forming a crystal on the substrate. Since component *Y* is still present in the vapour phase the liquid solution continues to saturate and precipitate, growing a long column, or whiskers, that are crystals as depicted in Figure 2.3. This is why it is named vapour-liquid-solid, because the reactants shift through all phases of matter.

As component *X* functions similar to a catalyst, it is not consumed. Thus an infinite amount of component *Y* crystals can be synthesized, provided that vapour is made available. In practice this does not occur as there are competing side reaction from the pyrolytic deposition of amorphous component *Y* which interfere with whisker growth. Pyrolytic deposition comes about from the decomposition of the source chemical due to elevated temperature and interferes in VLS via two methods. First a film might develop along the surfaces, halting the ability of component *X* to accept *Y* vapour. Second, the amorphous component *Y* can flake off and fall among any grown crystals disrupting the cap of component *X*, or sheering the whiskers apart.[51]

VLS was employed to successfully synthesize *α*-boron in the masters thesis of

Joseph Sitarik.[50] In Sitarik's work boron vapour was component *Y* and a series of transition metals served as component *X*. The resulting whiskers were 2 mm in length and 25 μm in diameter.[52] Efforts to reproduce this synthesis were moderately successful and are discussed in further detail in the following sections.

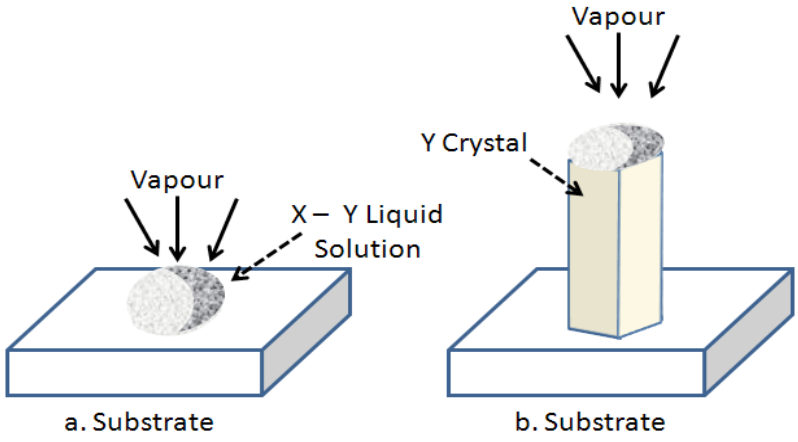

Figure 2.3: Whisker of component Y growing from X – Y eutectic system using VLS.

2.2.2 Chemical Vapour Deposition

During the course of the present VLS experimentation, discoveries lead to the creation of a new synthetic method that employs the principles of chemical vapour deposition (CVD). The details of the synthesis will be explained more fully in following sections however below is the theory of vapour transport in CVD.

CVD relies on the decomposition of precursor materials to vapours which chemically combine on a substrate to form the desired product. CVD is employed in a wide range of industries and applications to reliably produce pure solid films.

The theory of CVD[53] relies on two fundamental points: the flow of gas through a reaction chamber and the deposition of that gas on a surface. The movement of gas molecules through space follows a Maxwell distribution of velocities (*f(v)*) showing the probability of a particle having a speed which can be understood as:[53]

$$f(v)=\sqrt{\frac{2}{\pi}\boldsymbol{v}^2\left(\frac{M}{2\pi RT}\right)^3}\,\mathrm{e}^{\frac{-M\boldsymbol{v}^2}{2RT}} \tag{2.13}$$

where $\boldsymbol{v}$ is the magnitude of the velocity vector, M the molar mass, R is the ideal gas constant and T the temperature. This description results in a mean velocity $(\boldsymbol{v}_m)$ of:[53]

$$\boldsymbol{v}_m=\sqrt{\frac{8RT}{\pi M}} \quad . \tag{2.14}$$

Thus if the velocities of all molecules in the gas are approximated as the mean velocity every molecule within $t\times\boldsymbol{v}_m$ distance from the surface will collide with the surface. The precise number of molecules depends on the gas density, n:

$$n=\frac{N}{V} \tag{2.15}$$

where N is the number of molecules, and V is the volume. Despite simplifying the velocities of all molecules, the vector direction of those velocities plays an important role. Although all gas molecules are assumed to travel at the same speed, not all of them travel toward the surface, as can be seen in Figure 2.4. Contact is possible so long as a molecule

has some component of the velocity moving toward the surface, but this consideration removes half the possible vectors. Of the remaining non-perpendicular vectors it is considered reasonable that half of the molecules are close enough to strike the surface in the time available resulting in a molecular flux *(J)* of:

$$J = \frac{n v_m}{4} \quad . \tag{2.16}$$

Combining equations (2.13), (2.14), (2.16) outlines the maximum possible deposition flux of:[53]

$$J = 3.51 * 10^{22} \frac{P}{\sqrt{M T}} \tag{2.17}$$

where P is pressure in Torr, M is in g mol^{-1} and J is in molecules cm^{-2} s^{-1}. This equation, known as the Knudsen equation after the Danish physicist Martin Knudsen, is the upper bound on the rate of CVD.[53]

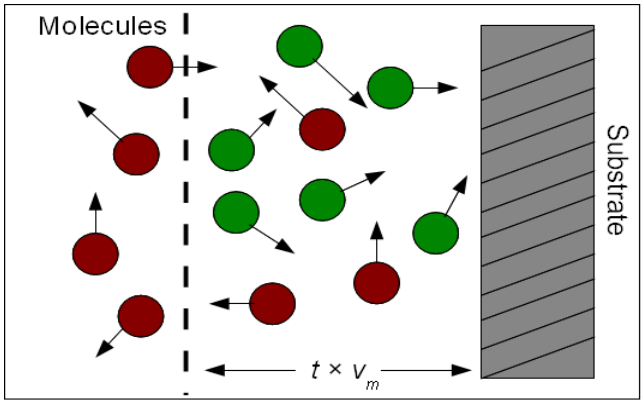

Figure 2.4: Approximation of gas flux toward substrate. Molecules shaded green will reach the surface, those shaded red will not. Adapted from Principles of Chemical Vapor Deposition.[53]

2.3 Instrument Theory

The focus of this section is a description of the instruments used throughout the project including: The Physical Property Measurement System, X-ray Diffraction and Scanning Electron Microscope.

2.3.1 Physical Property Measurement System

The Physical Property Measurement System (PPMS) from Quantum Design, depicted in Figure 2.5, is a commercially available instrument that can be used to measure a variety of physical and electrical properties through exchangeable analysis components called 'pucks'.

Figure 2.5: The Physical Property Measurement System. Components are, from left to right: Measurement chamber, ^{3}He probe, Computational hardware, User interface.

The PPMS is able to use relaxation calorimetry to determine heat capacity of materials at constant pressure, C_P, through use of the micro-calorimeter shown in Figure 2.6.[54]

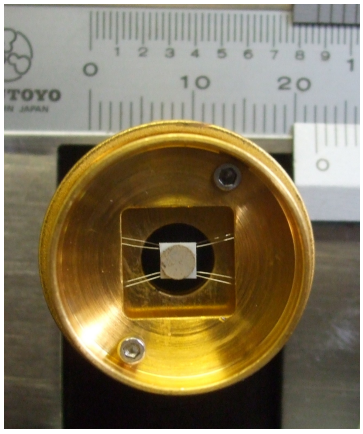

Figure 2.6: ^{4}He micro-calorimeter 'puck' in stand with pressed α-boron pellet mounted on the platform.

The micro-calorimeter is capable of measuring heat capacity of small samples (1 to 200 mg), in vacuum ($P < 10^{-4}$ Torr) and low temperatures (0.35 K to 400 K). The instrument is also capable of operating under a magnetic field (± 9 Tesla), and has a high heat capacity resolution (10 nJ K^{-1} at 2 K).[54]

Each micro-calorimeter puck has a commercial Cernox™ sensor and a thin film resistive ruthenium oxide (RuO) heater attached to the underside of the sapphire (Al_2O_3) platform. Both are connected to the rest of the puck via platinum wires, providing means for measurements as well as a link to the heat sink and structural support. A schematic of this system can be seen in Figure 2.7.

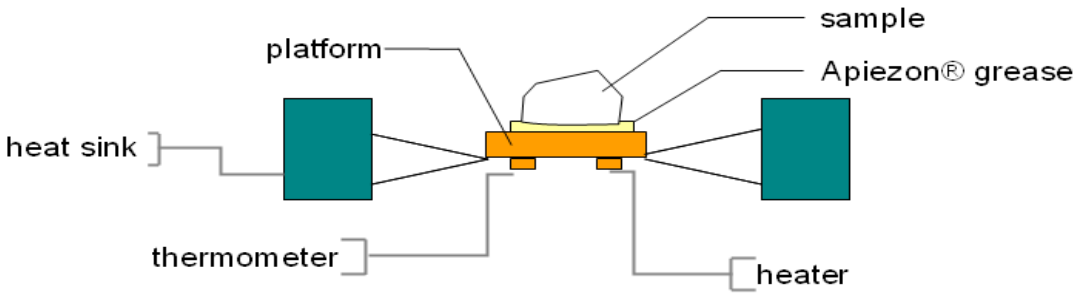

Figure 2.7: Cross section of micro-calorimeter schematic displaying sample on measurement platform and surrounding heat sink.

Since the Cernox™ sensor is located under the platform, the observed temperature is attributed to be that of the sample and grease. This is made possible due to the high thermal contact between the platform and sample imparted by the conducting grease. Initial calibration of the puck and measurement of an addendum containing only grease allows their heat capacities to be removed from the final measurement of any sample. A second thermometer is located on the heat sink which provides the temperature of the heat sink, T_0.

The PPMS operates as a relaxation calorimeter and related measurements require high vacuum conditions of ~0.01 mTorr. This ensures that all heat travels along the system described by the theoretical equations outlined in section 2.3.2, *i.e.,* losses due to convection with the atmosphere are minimized.

Thermally conductive grease from Apiezon® is used between the sample and the platform to ensure adequate thermal contact, and thus accurate measurements. Table 2.1 depicts the operating properties of greases selected for the experiments.

Table 2.1: Properties of experimental greases.[55,56]

	Apiezon® N	Apiezon® H
Melting Temperature/K	312 – 322	NA
Vapor Pressure/Torr	6×10^{-10}	1.7×10^{-9}
Thermal conductivity/W m^{-1} K^{-1}	0.194 (303 K) 0.095 (2K)	0.216 (303 K)
Working Range/K	2 – 300	210 – 390
Limitations	Phase change at $T > 320$ K	Contact loss at $T < 210$ K

For measurements below 300 K Apiezon® N grease was employed as it remains chemically and physically stable along the temperature range, has a low vapour pressure, and is thermally conductive at low temperatures.[55] Above 300 K, Apiezon® H grease was used as Apiezon® N grease undergoes a phase change to a liquid at temperatures greater than 320 K causing loss of thermal contact.[56]

A main consideration is the sample size which must be kept within a certain range. If the sample is too large, the time required for heating and relaxation will increase, and further if the thermal conductivity of the sample is poor, temperature gradients in the sample can build up, and significant error will be introduced. The lower sample size limit resides at the detection sensitivity of the technique. As the sample decreases in size, the signal to noise ratio degrades rendering the results meaningless. The optimal sample size is material dependent but in general high thermally conductive materials can have a larger size range. As an example, the thermal conductivity of sapphire (Al_2O_3) and zirconium tungstate (ZrW_2O_8) are ~40 W m^{-1} K^{-1} and ~0.8 W m^{-1} K^{-1},[57] respectively at room temperature. This results in a sample size restriction for zirconium tungstate to ~10 mg

for accurate relaxation calorimetry measurements, while sapphire has been tested up to 30 mg without issue.[58] In comparison to this β-boron has a recorded thermal conductivity of ~ 50 W m^{-1} K^{-1}, implying that samples can be in the range of sapphire or larger without issue.[59,60]

2.3.2 Relaxation Calorimetry

The general approach of relaxation calorimetry is depicted in Figure 2.8. A system is heated with constant power from an ambient state causing a rise in temperature. The power is then discontinued and the temperature relaxes to near the ambient state during which the heat capacity can be calculated.[61]

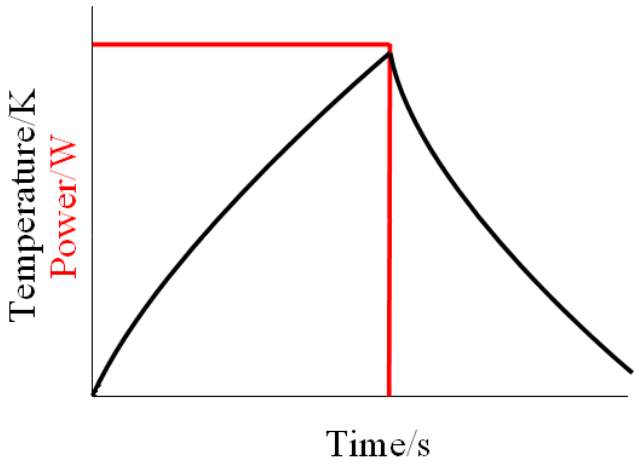

Figure 2.8: A system is heated from an ambient state with constant power causing a rise in temperature. The power is then discontinued and the temperature relaxes to the ambient state.

The relaxation component of the PPMS can be used to measure the heat capacity via the mathematics outlined in the following sections. This is broken down into two

cases: the simple one-tau model and complex two-tau[62] method. Both treatments rely on the same fundamental system arrangement depicted in Figure 2.9. In this depiction, T_x, T_a and T_0 are the temperatures of the sample, platform, and heat sink, respectively. The heat capacity is represented via C_x for the sample and C_a for the platform, both at constant pressure. K_1 and K_2 are the thermal conductances between platform and heat sink, and sample and platform, respectively.

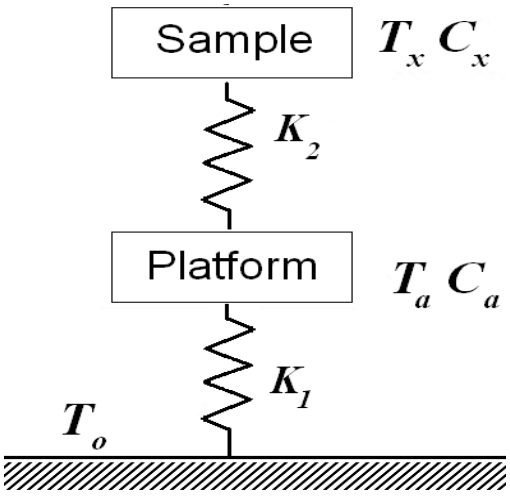

Figure 2.9: Graphical representation of the theoretical relaxation calorimetry system. T is the temperature, C the heat capacity at constant pressure, and K the thermal conductance between sections. Adapted from work by Lashley et al.[63]

2.3.2.1 Two-Tau Method

The two-tau method is the more complex and complete of the theoretical treatments available. This complexity is introduced to account for the finite thermal conductance between the sample and the platform. This treatment is employed for systems of poor thermal contact, meaning heat is unable to transfer between systems

through a surface. Usually poor contact is the result of an irregular surface or the need of a thermally conducting grease. Since the flow of heat from the sample to the platform is not instantaneous the resulting mathematical description for the relaxation of the temperature of the platform is:[62,63]

$$T_a(t) = T_0 + A\,\mathrm{e}^{-t/\tau_1} + B\,\mathrm{e}^{-t/\tau_2} \tag{2.18}$$

where t is time, A and B are constants dependent on the system, and there are two time constants, τ_1 and τ_2. The tau values are a ratio of the heat capacity with the corresponding thermal conductance:

$$\tau_1 = \frac{C_a}{K_1} \tag{2.19}$$

$$\tau_2 = \frac{C_x}{K_2} \tag{2.20}$$

and by expanding the terms and simplifying one can find the two heat capacities as:[62,63]

$$C_a = P(t) - K_1[T_a(t) - T_0] + K_2[T_x(t) - T_a(t)] \tag{2.21}$$

$$C_x = -K_2[T_x(t) - T_a(t)] \tag{2.22}$$

which allows the determination of the sample heat capacity provided that an addenda measurement of the platform has been collected for subtraction.

2.3.2.2 One-Tau (or Simple) Method

The two-tau method is the more general description, pivotal for applying relaxation calorimetry to unknown samples but for cases of good thermal contact, for example an addenda measurement with only a thin layer of grease, the temperature relaxation can be characterized more directly. The simple one-tau method approximation is given by:

$$T_a(t) = T_0 + \Delta T\, \mathrm{e}^{-t/\tau_1} \tag{2.23}$$

Where this works under the assumption that the sample and platform act as one functional unit. The terms ΔT and τ, can be expanded as:[62,63]

$$\Delta T = \frac{P}{K_1} \tag{2.24}$$

$$\tau_1 = \frac{C_x + C_a}{K_1} \tag{2.25}$$

where P is the power applied. Once again the mathematics can be simplified, as shown by:[63]

$$(C_x + C_a) = K_1(T_a + T_0) + P \quad . \tag{2.26}$$

Relaxation calorimetry relies on the fundamental equations (2.21), (2.22) and

(2.26) to describe the thermal relaxation and the choice of the two-tau or simple method depends on the degree of thermal contact between the sample and platform.

2.3.2.3 Method Advantages and Disadvantages

The unique properties of relaxation calorimetry provide opportunities for materials research not available from alternate calorimetic methods, however the technique is not perfect. The accuracy of relaxation calorimetry is comparable to the traditional adiabatic calorimetry as seen in Table 2.2.

Table 2.2: Accuracy of relaxation calorimetry (RC) and the leading technique of adiabatic calorimetry (AC). Adapted from Bachmann et al.[61]

Method	Defining relation	Time constant	Useful sample size	Conditions for 1% accuracy
Pulse (AC)	$C=\Delta Q/\Delta T$	τ_1 very long	>200 mg	$5\tau_1$ > pulse length > $5\tau_2$
Step (RC)	$C=K\tau_1$	$\tau_1 > 5\tau_2$	1-100 mg	$\tau_1 >> \tau_2$

The focus of relaxation calorimetry on thermal relaxation allows accurate measurements within a range of 1 to 200 mg as opposed to the 200 mg or more requirements of specialized adiabatic calorimetry. The low limit on valid sample size for relaxation calorimetry allows analysis of materials where synthesis produces small amounts of product. That same focus restricts the ability of relaxation calorimetry to gain information on transition states, and increases the experimental margin of error with respect to adiabatic calorimetry.[64] To provide accurate measurements with such low masses the percent contribution of sample with respect to background has to be > 20 %. As explained in the work of Kennedy *et al.*[58] sample contributions less than 20% do not provide

accurate measurements. Relaxation calorimetry requires less time than adiabatic, since it does not have long data collection times, however it is still limited by the rate of relaxation. Taking a general case depicted in Figure 2.10, a very small increase in temperature has a relaxation time t_1, while a larger increase has a much larger relaxation time, t_2. The precise value of this effect is sample dependent but the trend is generally viewed across all relaxation calorimetry experiments. This temperature dependence requires using cryogenic liquids to retain a reasonable operating time, introducing high operating costs and the need for specialized equipment. The requirement for commercial relaxation calorimeters stands in contrast to the custom built adiabatic calorimeters of the past. As a result of these factors measurements using the Physical Property Measurement System for relaxation calorimetry cannot take place at a temperature above 400 K. Working near the upper limit with the newer equipment and methods requires less patience than the past, but it is still non-trivial.

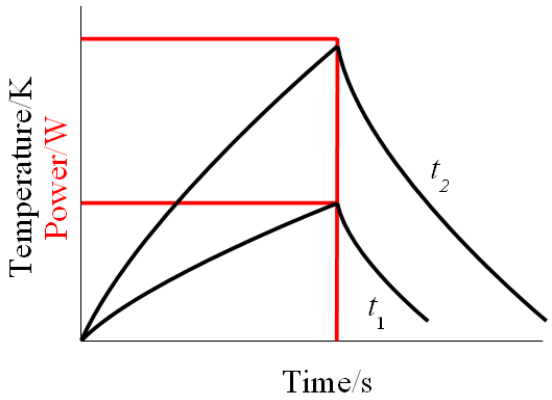

Figure 2.10: General form of relaxation times vs. temperature. Increasing the temperature rise increases the time for relaxation to the ground state resulting in $t_2>>t_1$.

2.3.3 X-ray Diffraction

X-ray diffraction (XRD) is a nondestructive analysis technique with good reliability for the characterization of crystalline materials.

Crystalline solids are ordered arrays of atoms held together in a lattice possessing a periodic nature. As a result of this order, crystals can be explained by a unit cell – the minimum volume that holds translational symmetry. The unit cell can be used to map a crystal of infinite size and is described by three vectors: ***a***, ***b*** and ***c*** and three angles: α, β, and γ as depicted in Figure 2.11 for the rhombohedral case.

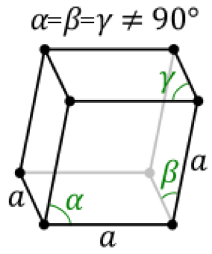

Figure 2.11: Rhombohedral unit cell where a = b = c.

X-rays are scattered by electrons which are themselves localized to the atomic sites of a crystal lattice. Thus a plane of x-rays directed at a sample will, due to the periodic nature of crystalline materials, create a primary reflected beam and a secondary 'diffracted' one. This diffracted beam is related to the interplanar spacing *(d)* of the crystalline phase according to the mathematical relationship of 'Bragg's Law' which states that:[65]

$$n\lambda = 2\mathrm{d}\sin(\theta) \tag{2.27}$$

where n is an integer, λ is the wavelength of the x-ray radiation, and θ is the x-ray diffraction angle. Thus a detector positioned at some angle 2θ can collect the diffracted x-rays, but only if beam paths cause what is called 'constructive interference'. Constructive interference occurs when the beams diffracted from different layers have identical phases, which will create an amplified signal. The opposite is destructive interference, where the phases of the two waves are exactly in opposition, removing the signal. The combined effect is a series of peaks and troughs.

For Bragg diffraction, interference is based on the path length experienced by rays coming from alternate planes. The extended path introduced by the plane spacing increases the distance by $2d\sin(\theta)$ and can be seen in Figure 2.12.

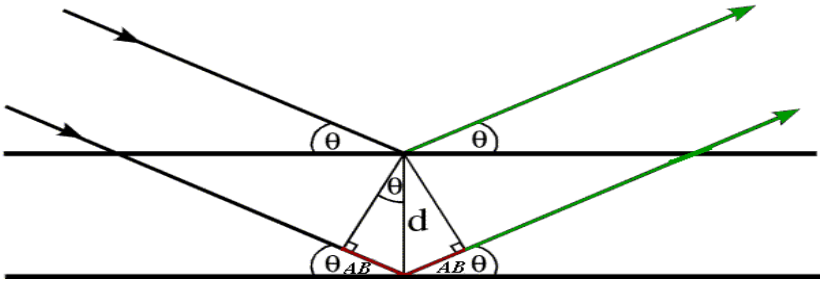

*Figure 2.12: Bragg's Diffraction. The distance travelled by the second reflected beam is longer than the primary beam by 2**AB**.*

Thus via Bragg's law (2.27), constructive interference can only occur if the path length increases by an integer number of the incident wavelength, or $n\lambda$. The resulting diffraction maxima, or Bragg peaks, are akin to a finger print, allowing the characterization of crystalline samples.

In the employed XRD system the wavelength remains constant, and the angle varies as measurements are taken. Thus if the wavelength of the x-ray at some angle 2θ matches the path increase of the *d* spacing, constructive interference occurs and a peak of some intensity will be observed. The resulting pattern has the 'angle' of diffraction related to the interplaner spacing *(d)*, while the intensity of the peaks relates to the strength of the diffraction in the sample.

Details on the instrument can be found in section 3.2.1.

2.3.4 X-ray Spectroscopy

During the course of synthesis and analysis questions arose as to the character and nature of the systems both during and after the synthesis. There was also a degree of uncertainty in x-ray diffraction assignments of possible impurities. To answer these questions scanning electron microscopy (SEM) and energy-dispersive spectrometry (EDS) were deemed viable methods for determining the purity and composition of the samples.

In 1935 Max Knoll developed the scanning electron microscope.[66] As is the case in all microscopy, the SEM relies on the changes in the incident beam, in this case, induced by electronic interactions with the sample material as it is scanned along the surface.[67] The versatility of SEM comes from the numerous possible interactions between the beam and sample, two of which are of chief interest toward the questions raised by this work: low-energy secondary electrons, and energy-dispersive spectroscopy.

2.3.4.1 Secondary Electrons

The incident beam of energized electrons is able to ionize loosely bound outer shell atomic electrons during inelastic scattering. The released low-energy secondary electrons propagate through the material and, should they pass through the surface, will be free for collection by a detector. The secondary electrons possess variable escape velocities as a function of their initial binding energy and distance travelled, providing a high resolution image of the sample surface.[67]

2.3.4.2 Energy-dispersive X-ray Spectroscopy

Discovered in 1968 by Fitzgerald *et al.*,[68] energy-dispersive spectroscopy (EDS) is an analysis technique capable of mapping elemental composition with spacial resolution. The fundamental theory of EDS can be understood by considering a lone atom, as in Figure 2.13.

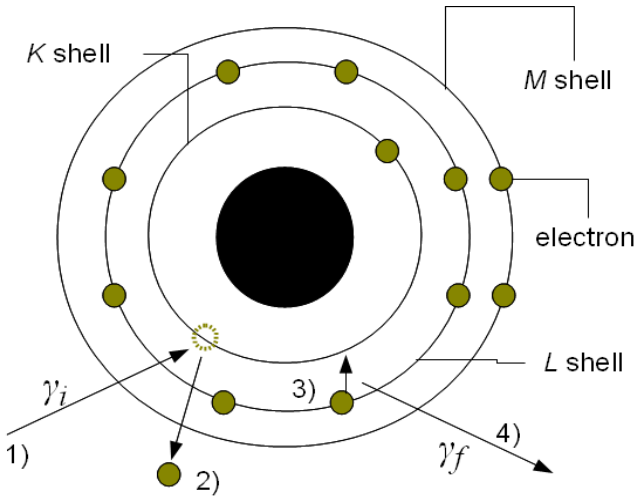

Figure 2.13: Energy shell diagram for magnesium depicting the steps of characteristic x-ray generation. 1) The incident beam interacts with the atom, 2) the imparted energy ejects an inner shell electron, 3) an atomic electron of higher energy fills the vacancy, 4) this releases an x-ray corresponding to the energy loss from the L shell to the K.

An atom, magnesium in Figure 2.13, possesses a quantity of electrons situated in orbitals, or shells. These shells exist at some discrete energy level of increasing magnitude with radius and ranked starting from K. If an external source of energy, such as the electron beam, interacts with the atom it will impart energy to the system. This energy is of sufficient quantity to excite an electron from the inner shells to either one of the outer shells, or to overcome the binding energy and completely free the electron from the atom. The now vacant inner shell is quickly occupied by atomic electrons of higher energy, releasing a characteristic x-ray. The eneries of the emitted x-rays depend on the relative difference between the atomic orbitals, which depends on the atom.[67]

The released x-ray eventually reaches a detector made of a Si-Li dielectric pair. The x-ray interacts with the pair, producing an electron at the junction; this electron is swept from the surface and counted. The SiLi detector needs to be kept at low temperatures to prevent Li drift through the material with the electron sweep. Most SiLi detectors possess a beryllium window limiting the ability to resolve lighter elements.

Another form of detector is the silicon drift detector (SDD) which also generates electrons from incoming x-rays. However it contains no Li, allowing it to resolve lighter elements. It is cooled via Peltier cooling instead of liquid nitrogen.

Chapter 3 Experimental Methods

3.1 Synthesis

Allotrope acquisition and synthesis is broken down into α-boron and β-boron.

3.1.1 α-boron

The synthesis of α-boron followed two fundamental approaches, VLS synthesis and CVD synthesis. The following chapters explain the experimental approaches.

3.1.1.1 Vapour-Liquid-Solid Chemicals

α-boron synthesis via VLS theory[50] is presented in section 2.2.1. All materials for α-boron VLS synthesis were obtained commercially and used without further purification. Table 3.3 shows a list of all chemicals employed, their suppliers and purities.

Table 3.1: Chemicals, suppliers, purity employed during experiments.

Chemical	Supplier	Purity
Boron tribromide	Sigma Aldrich	4N
Boron trichloride	Sigma Aldrich	4N
Hydrogen gas	Praxair	5N
Nitrogen gas	Praxair	5N
Gold nanolayer	Johnson Matthey & Co.	4N
Gold dust	Johnson Matthey & Co.	3N
Granular lead	Fisher Scientific	3N
Platinum dust	Johnson Matthey & Co.	4N

For a boron source material, the reagents boron tribromide (BBr_3) and boron trichloride (BCl_3) were selected and compared. Both reagents react spontaneously in air to form boric acid and hydrogen halide acid but can also be reduced in an inert atmosphere with the application of heat.[69,70] Initial experimentation employed BBr_3 based on two points of merit: 1) BBr_3 was available for purchase in small quantities (25 mL vs. 456 mL), maximizing efficiency, 2) since Br is a heavier halogen and thus has weaker bonds than Cl it would have an improved rate of reaction in the chamber.[71] Despite these advantages a failure in the experimental apparatus during the course of synthesis necessitated the use of BCl_3.

Hydrogen gas of 5N grade from Praxair was selected to reduce the trihalide boron sources. Nitrogen and argon gas, both from Praxair at 5N purity, were used as the chamber purge gases for the BBr_3 and BCl_3 experiments, respectively.

The liquid solution reagents went through a series of modifications based on experimental results. Gold was chosen as the first liquid reagent based on the work of Ahmad and Heffernan.[74] Initial experimentation began with gold deposited on the substrate via chemical vapour deposition (CVD) by Andrew George in the Department of Physics at Dalhousie University. The CVD applied a variable layer of gold depending on the synthetic experiment via thermal deposition in vacuum at a base pressure $\sim 5\times10^{-6}$ Torr. The gold (4N purity) was evaporated from a tungsten basket positioned approximately 10 cm below the quartz substrate. The thickness of the deposited gold layer was monitored by a 5 MHz quartz microbalance. The gold was then annealed at 800°C for 10 minutes in an ultra high purity argon flow using a Rapid Thermal Processing furnace. The gold film appeared pink after the annealing due to the formation

of gold nanoparticles which, being on a similar scale to the wavelength of visible light, undergo Mie scattering.[72] Later, an attempt was made to employ gold sponge from Johnson Matthey & Co. The only processing employed was to decant the gold particles selecting liquid solution reagent of the size able to adhere to the substrate by frictional/electrostatic forces.

The final selection of liquid solution reagent was platinum dust. Initial experiments employed filings from a platinum thermal couple wire, with 0.5 mm diameter. Subsequent efforts reapplied the CVD approach used to produce layers of gold as outlined above.

3.1.1.2 Vapour-Liquid-Solid Apparatus

The reaction was carried out within a Lindberg three-zone radiative furnace, model 55348. The furnace operates to a maximum temperature of 1100 °C with 3830 W, 50/60 Hz and 240 V. The cavity allowed for a removable reaction chamber of 50 mm diameter, a feature needed for ease of cleaning. The reaction was carried out in a quartz cylinder depicted schematically in Figure 3.1, with 50 mm outer diameter, 46 mm inner diameter, and length of 1 m. The chemical and thermal stability of quartz, acquired from Technical Glass Products, allowed for non-atmospheric reaction conditions. To further protect the feed and waste gas lines from thermal bleeding, the very ends of the reaction chamber, 14 cm in, were filled with a thick bundle of quartz wool. The thermal barrier was non-reactive to the reagents and limited temperature gain along the feed line seal to a maximum increase of 50 °C.

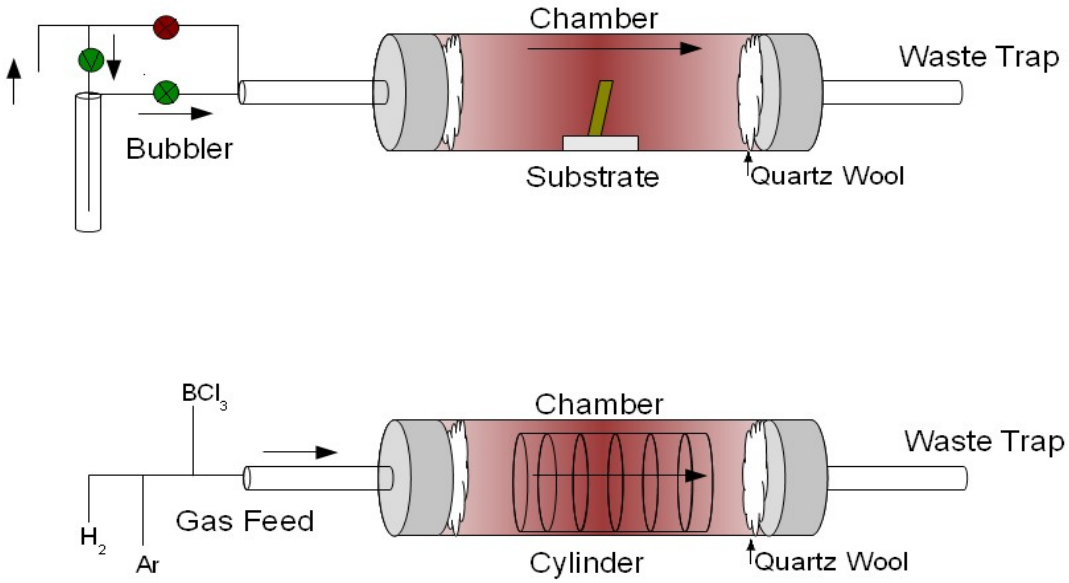

Figure 3.1: Schematic of all apparatus components. a) system arrangement for BBr_3 experiments. b) System change for BCl_3 experiments.

After each reaction the chamber acquired a fine, but sparse, layer of white deposit via vapour residue. Further there was a steady build up of an unknown black layer intermixed with brown, thought to be boron along the tube surfaces. To clean these residues a set of four solvents was employed. First boiling concentrated nitric acid was poured into the tube and swirled. After removing the waste a similar method was employed for sulphuric acid and *aqua regia* of standard 3 HCl : 1 HNO_3 by volume. As a final effort the chamber was scrubbed with nanopure water using an elongated brush. Of all methods the scrubbing proved the most effective, turning the blackened tube colourless with minor grey residue.

The waste gas created as a byproduct of the reaction travelled out of the chamber through a steel sheathed, Teflon flexi-pipe to a pair of water traps. The resulting acidic

solutions of HBr or HCl were disposed of by the Physics Department chemical waste disposal.

Andrew George designed the bubbler apparatus that housed and delivered the reagents to the reaction chamber for the first eight experiments. There were five primary requirements for the bubbler design: 1) efficient transport of BBr_3 into the reaction chamber, 2) air tight seal protecting the BBr_3 from the atmosphere, 3) non-reacivity of the bubbler and reagents, 4) thermal resistance at the operating temperature, 5) easy isolation of bubbler for reagent loading. Figure 3.2 depicts a schematic of the bubbler design.

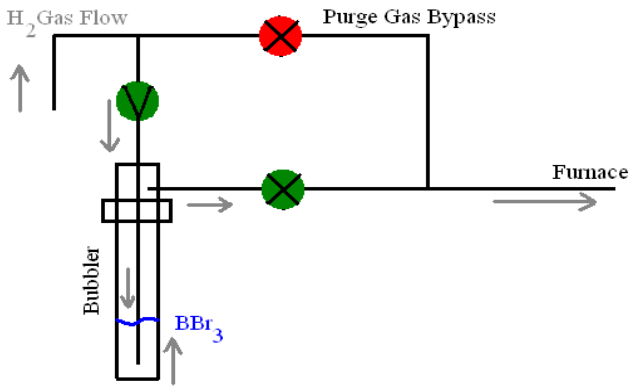

Figure 3.2: Bubbler designed by Andrew George of the High Temperature Physics lab.

The bubbler apparatus was 32 cm long and 28 cm wide. Stainless steel was considered sufficiently resistant to the reagents and thus the bubbler was assembled from 1/4 inch piping from Swagelok. The metal would easily resist the thermal bleeding from the furnace proper solving the fourth issue. The connecting joint to the reaction chamber was an aluminium locking screw with rubber o-ring, which could be removed completely allowing the reservoir to be filled. The bubbler reservoir was made of quartz, due to its

chemical durability and visual transparency. This would allow the BBr_3 to be stored in a chemically resistant environment for long term experimentation and to allow easy indication of reagent depletion. The reservoir was seated with a rubber o-ring and aluminium locking screw of similar design to the bubbler/chamber connection. To maximize the bubbler efficiency and limit contamination by air, it was designed with a bypass for purging the reaction chamber of air. Sealing the reagent line and opening the bypass allowed the whole system to be flushed in approximately 40 minutes. To control the flow of gas through the bubbler, a pair of stainless steel valves were added along the bypass and reagent line. The twin stainless steel bellow valves were purchased from Swagelok (part SS-4H) and are indicated by 'x' in Figure 3.2. The third valve, indicated with a 'V' in Figure 3.2 was the SS-4P4T a quarter-turn instrument plug valve and a more typical, but less robust product. This valve used a Teflon coated, silicone lubricated, rubber o-ring to act as a seal. An Atlantic Valve Fittings Quickconnect joint, with ethylene propylene seal, allowed for easy connection between the gas cylinders and the bubbler system via Teflon coated tubing.

Gaseous H_2 was as the carrier for the liquid component BBr_3 for efficient transport of reagents.. The $H_{2(g)}$ was introduced as the carrier gas into the bubbler, the 100 cc min^{-1} flow providing a steady influx of 0.008 mol cm^{-2} hr^{-1} $BBr_{3(l)}$ to the furnace chamber. The system was demonstrated to be air tight by pouring a soap solution along the joints while the purge gas (N_2) flowed.

When the boron source was modified from BBr_3 to BCl_3, the bubbler was replaced with a 1/4 inch stainless steel hub joint assembled by Andrew George. There were three Quickconnects from Atlantic Valve Fittings, one to the reagent H_2, one to the purge gas

Ar, and one to the reaction chamber. The remaining valve line to the cylinder of gaseous BCl_3 employed the SS-PT4T quarter-turn plug valve from Swagelok. Since the BCl_3 is incompatible with the available flow metres, the amount of gas was undetermined quantitatively. Flow rate was qualitatively determined via the observation of the water trap. Conditions were considered ideal when the atmosphere above the water became cloudy with vapour, but the water itself remained clear. This corresponded to approximately 15 bubbles of waste gas a minute, each containing an estimated 0.065 mL of vapour making the total flow 1 mL/min.

3.1.1.3 Vapour-Liquid-Solid Preparation

All materials were carefully prepared to maximize the retention of their commercial purity. The most involved step was the transfer of BBr_3 from the sealed ampule to the bubbler reservoir. BBr_3 is sensitive to moisture and decomposes spontaneously into HBr and $B(OH)_3$. HBr is a strong acid and a vapour at room temperature. Thus a multi-chamber helium glove box was employed to transfer the reactive BBr_3 into the bubbler reservoir. The glove box was regenerated prior to each BBr_3 reagent transfer and the bubbler was only admitted after three pump and purge cycles to minimize water contamination.

The substrate used for the α-boron synthesis was a quartz plate from Quartz Scientific Inc. During experiments 1-7 the plate was cut into inch square segments by the Department of Chemistry glassblower Todd Carter. For experiment 8 two slides were soaked in hydrofluric acid (HF) of unknown concentration for two hours to induce chemical etching. The concentration of the acid was unknown but is no more than 48% by

mass. One slide was then further roughened via silicon carbide polish, 180 grit for 20 min.

3.1.1.4 Vapour-Liquid-Solid Synthesis of *α*-Boron

In total there were ten attempted VLS synthetic runs, four basic sets which are summarized along with the seven CVD experiments in Table 3.2.

The Set 1 experiments focused on reproducing the works of Sitarik and Ellis,[73] and Ahmad and Heffernan.[74] The initial experimental set focused on gold as the metal solution, operated at 900 °C for 20 min.

Considering the consumption of gold to be the limiting factor, efforts were made to increase the metal liquid layer throughout Set 1 until it was realized that the eutectic system was not forming.

The second set of experiments focused on optimizing the liquid metal, with efforts directed toward lead and platinum for their improved eutectic forming ability. The results were poor, which led to exploration of the system in experiment 8. It was demonstrated, while testing the chamber for contamination in experiment 8, that the bubbler had failed during the third set of experiments.

Table 3.2: List of experimental attempts at α-boron synthesis. Sets 1 to 3 used VLS method. Sets 4 to 6 used the CVD method.

Set	Experiment	Boron Source	Temperature (°C)	Metal Liquid/Catalyst	Gas Flow (L/min)	Substrate Position	Time (min)
1	1	BBr_3	900	5 nm nano Au	0.2	Vertical	20
	2	BBr_3	900	5 nm Au	0.2	Horizontal	20
	3	BBr_3	900	Au sponge	0.2	Horizontal	20
	4	BBr_3	900	98 nm Au	0.2	Horizontal	20
	5	BBr_3	900	98 nm + sponge Au	0.2	Horizontal	20
2	6	BBr_3	900	granule Pb	0.2	Horizontal	18
	7	BBr_3	900	Pt dust	0.2	Horizontal	18
	8	BBr_3	900	none	0	Horizontal	18
3	9	BCl_3	900	5 nm Pt	0.001	Horizontal	10
	10	BCl_3	900 + 5/cm	5 nm Pt	0.001	Vertical	30
	11	BCl_3	900 + 5/cm	5 nm Pt	0.001	Vertical	60
4	12	BCl_3	900 + 5/cm	none	0.001	Vertical	2x 60
	13	BCl_3	900 + 5/cm	none	0.001	Vertical	2x 60
5	14	BCl_3	850	none	0.001	none	2x 45
	15	BCl_3	845	none	0.001	none	2x 45
6	16	BCl_3	850	none	0.001	none	2x 30
	17	BCl_3	850	none	0.001	none	2x 45
	18	BCl_3	850	B_2O_3	0.001	none	2x 30
	19	BCl_3	850	Basic Surface	0.001	none	1x15

The Set 3 experiments were attempted after replacing the liquid BBr_3 with BCl_3 gas. Experiment 9 was a repeat of experiment 7 in the hopes of improvement. When no success was observed, experiments 10 and 11 were conducted under a temperature gradient discussed in section 4.1.2.2. Observations during these experiments lead to a change in synthesis tactics and the CVD method.

The results of all experiments are presented in section 4.1.

3.1.1.5 Chemical Vapour Deposition Chemicals & Apparatus

All materials, and apparatus for α-boron CVD synthesis were identical to those outlined in the VLS synthetic discussion.

3.1.1.6 Chemical Vapour Deposition Preparation

There was no required preparation for the chemical reagents employed in the CVD experiments.

All glassware was prepared in the same manner as the VLS experiments with one exception. Seeking to capitalize on the favourable deposition along the chamber walls, a cylinder of quartz with diameter 36 mm was inserted into the larger chamber to act as a removable deposition surface. This cylinder was segmented into sections in an effort to map the effect of temperature on synthesis, and improve product recovery. The segments were of steadily increasing lengths to allow consistent assembly of the cylinder over multiple uses. The dimensions are presented in Table 3.3.

Table 3.3: Segmented Cylinder Dimensions

Segment	Dimensions/ mm
1	19
2	21
3	25
4	26
5	29
6	32

3.1.1.7 Chemical Vapour Deposition Synthesis of α-Boron

CVD synthesis covered the fourth, fifth and sixth experiment sets listed in Table 3.2. All CVD experiments consisted of two cycles of reagent flow/heating with a period of cooling between, effectively doubling the experiment time.

Set 4 focused on the deposition of boron along the chamber walls under temperature gradient conditions to determine the most efficient operating temperature. The segmented cylinder, outlined previously, provided a removable surface for boron deposition with each segment existing at a discrete temperature.

Set 5 was a production run aimed at generating product sufficient for thermodynamic analysis.

Set 6 was an attempt to understand the uncertainty of the synthesis mechanism. Initial efforts focused on the exposure of the system to air, while later optimizing the catalysing agent of the synthesis. To test atmosphere effects, a fresh cylinder was heated with reactant gas and then cooled without exposure to air before the second heating/gas flow. This result was compared with a second identical run in which the cooling step involving exposure to air. Experiments 17 and 18 attempted to produce product without exposure to atmosphere via catalysing reagents, initially B_2O_3, and finally by increasing the pH of the interior surface to seven.

The results of the CVD experiments can be found in section 4.1.2.

3.1.2 β-boron

A sample of β-boron 99.5% pure was acquired commercially from Alfa Aesar. Prior to that, attempts were made to convert α-boron into β-boron, however it was deemed more convenient and efficient to employ the commercial source given the complexity of α-boron synthesis.

3.2 Characterization

3.2.1 X-ray Diffraction Settings

All x-ray diffraction patterns were acquired on a Siemans D500 operated by Andrew George using the copper-K_α band and collected from 15° to 50°.

Most patterns were collected on the products as grown, with the substrate being placed directly into the instrument. The analysis of tube surface deposits required spreading the powder along a silicon wafer with the crystallographic plane 510 facing upward.

All XRD peak assignments were carried out using the Match!™ program[75] with the ICDD PCPDF[76] database. The α-boron pattern identification was compared against the calculated Match! Entry 00-085-0702,[77] and β-boron was identified via Match entry 00-089-2777.[78]

3.2.2 X-ray Spectroscopy Experimental Settings

Two separate instruments were employed for x-ray spectroscopy: the VLS studies with Patricia Scallion of the Institute for Research and Materials, and the CVD with Daniel MacDonald of the Geology Department.

3.2.2.1 VLS

The SEM at the Institute for Research and Materials employes a cold-field source (CFS) for the electron beam. Rather than creating electrons from thermal electric heating, a CFS uses an applied electric field to overcome the work function.[79,80] A CFS has the advantage of providing a relatively high-current electron probe with low energy spread, high brightness, and a small virtual source diameter, especially at low accelerating voltages. These advantages are offset by the requirement for ultra-high vacuum and the steady flicker, due to molecular deposition on the source of the emissions.[67]

SEM images and analysis of the VLS products were collected on the Hitachi S-4700 by Patricia Scallion, Research Technician at the IRM. Capable of imaging from 30 × to 500 k× magnification, the beam is generated by a tungsten cold field emitter and able to produce an intensity that can be as low as 500 V. The elemental composition was acquired using the Oxford Inca Energy Dispersive X-ray analysis system. All SEM images from the Hitachi S-4700 were obtained using the settings outlined in Table 3.4.

Table 3.4: VLS SEM settings.

Parameter	Value
Accelerating Voltage/kV	10-15
Generator Current/μA	20
Working Distance/mm	4-5
Operating Mode	Ultra High A
Condenser Lense CD	1 of 14
Stage Diameter/mm	12.55

3.2.2.2 CVD

EDS analysis was obtained by the JEOL 8200 microprobe, using the 128 eV resolution energy-dispersive spectrometer. The JEOL employs a Peltier-cooled silicon drift detector which means it has no beryllium window, nor does it require cryogenic liquids. It also possesses a higher count rate. All EDS analysis on the JOEL 8200 used the settings outlined in Table 3.5.

Table 3.5: CVD SEM settings.

Parameter	Value
Accelerating Voltage/kV	5
Beam Current/nA	20

3.3 Relaxation Calorimetry Preparation

3.3.1 α-Boron

The α-boron synthesis produced a granular powder which needed to be pressed into a pellet for measurement in the PPMS. Pellets were formed using a stainless steel pellet die, manufactured by the Physics Department Machine Shop. The die consisted of three components, a sleeve, a base and the piston, depicted in Figure 3.3. There was also a spacer, which was used to assist in removal of a pellet.

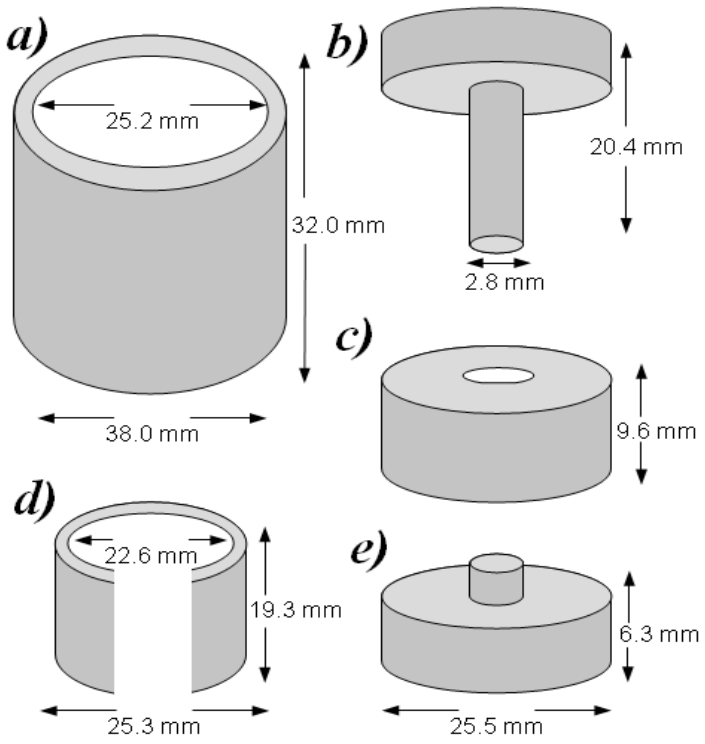

Figure 3.3: Pellet die components. a) Sheath: protects and aligns other parts; b) piston: applies force through the holder; c) Holder: contains sample; d) Spacer: helps to remove pellet; e) Stand: base of die.

Between 8 and 13 mg of α-boron was inserted into the base opening, depending on the desired pellet dimensions and mass. The pellet was pressed via the Carver Laboratory Press, model 3912 (Fred S. Carver, Inc.) with a listed maximum force of half a metric tonne. Based on the die dimensions, the resulting pressure applied to the pellet was approximately 0.8 GPa.

Initial attempts at pellet formation employed methanol as a binding agent, forming a slurry of α-boron and methanol. The resulting pellet did not survive contact with forceps leading to further attempts with a dry press approach. The dry pressing at the above pressure provided pellets that were stable over extended time and repeated cleaning with toluene to remove grease. Samples mass was determined via the Sartorius CPA225D analytical scale to within 0.01 mg.

3.3.2 β-Boron

As purchased, the β-boron crystal possessed a rough, irregular surface and thus required some processing for good thermal contact between the sample and the heater stage. To obtain good measurement results the sample requires a flat surface, which was achieved by Gordon Brown of the Dalhousie Thin Section Preparation Laboratory, Department of Earth Sciences.

The steps toward producing a flat surface were as follows. First a portion of crystalline β-boron was broken off the main body of material via freeze fracture. The resulting shard was mounted on a glass slide with epoxy using a Buehler mounter. The slide was then loaded into a G'Brot grinder to expose the grain and moved to a Durener

lead wheel polisher where a mixture of diamond dust and oil steadily polished the surface to a mirror shine after 3 hours. Residual oil and any deposited diamond grit was removed by an ultrasonic cleaner.

Unfortunately the samples polished by Gordon Brown possessed masses of 5 mg and lower which were found to provide poor quality heat capacity results at temperatures below 100 K due to low sample contribution to the total heat capacity (< 20%).

In an effort to acquire larger mass samples shards of the β-boron crystals were cut into rectangular prisms on the Bruehler Isomet low speed diamond saw of the High Temperature Physics Laboratory. The water-cooled diamond saws from Laperoft Dia-Laser (cat #12114) were 4” diameter, 0.012” thickness with a 1/2” inner diameter.

The freeze fractured samples of β-boron were mounted on aluminium stages prepared by the Chemistry Department Machine Shop. The stage had dimensions of 2.4 by 2.6 by 1.2 cm and a threaded opening of 4.2 mm in diameter for mounting via screws. The binding agent employed was Speed Set Epoxy from Lepage and was removed with dichloromethane over several hours. The PPMS stage limited base dimensions to under 3 mm and the height was limited by the thermal conductivity of the sample.

Since the hardness of boron on the Moh's scale is ~9.5, blade wear was a concern. To achieve the desired dimensions a blade was replaced approximately every two cuts depending on microcrystal grain directions. The blades displayed random variations from the ideal cut direction due to the hardness of the sample. All sample masses were determined on the Sartorius CPA225D analytical scale to within 0.01 mg with a range of 15 mg to 37 mg and are listed in more detail in sections 4.2 and 4.3.

Chapter 4 Results & Discussion

The results of the present experimentation are divided into two main sections, *α*-boron synthesis and thermodynamics.

4.1 *α*-Boron Synthesis

The *α*-boron synthetic procedures underwent continual optimization in light of results. The initial work focused on reproduction of known synthetic methods, VLS, but transitioned into novel methods employing CVD.

4.1.1 VLS Method

The results of the VLS experiments are divided into three general groups focused around Set 1, Set 2 and Set 3 (Table 3.2). Major features of the experimental sets are reproduced in Table 4.1 for reference and full experimental details are given in Table 3.2.

Table 4.1: Summary of α-boron synthesis experimental sets. Set 1, 2 and 3 used VLS method, Set 4, 5 and 6 CVD method.

Set	1	2	3	4	5	6
Experiment	1 2 3 4 5	6 7 8	9 10 11	12 13	14 15	16 17 18 19
Major Feature	Gold liquid metal reagent for VLS catalysis	Platinum liquid metal reagent for VLS catalysis	Change from $BBr_{3(l)}$ boron source to $BCl_{3(g)}$	Beginning of CVD Experiments	Production of α-boron for thermodynamic measurements	Mechanism Exploration of CVD method

4.1.1.1 Set 1 Experiments – VLS Exploration

With the focus of reproducing literature results, Set 1 experiments used gold liquid metal of varying layers, BBr_3 as a boron source, and an operating temperature of 900°C. The typical product of Set 1 experiments, depicted in Figure 4.1, was a black layer close to the substrate surface and a brown secondary layer atop it.

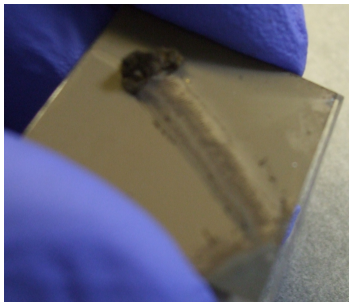

Figure 4.1: Typical Set 1 experimental results. Quartz substrate coated with a black layer atop of which rests a brown layer.

Initial focus was directed to the bottom layer due to its black colouring, as black was listed as the known colour of polycrystalline α-boron.[50] After studying the sample as grown using powder x-ray diffraction (XRD), as seen in the top pattern of Figure 4.2, the brown layer was removed by passing a knife along the black surface. The brown layer was loosely bound to the rest of the sample, easily flaking off. The mechanical removal of material did not fully separate the two layers; small amounts of brown could still be seen on the substrate, and the resulting 'shavings' contained some black material. The components as-separated were then investigated via XRD to isolate their signals.

The brown layer, shown as the bottom pattern of Figure 4.2, displayed a broad

background consistent with amorphous boron signal, but a substantial unidentified crystalline peak was apparent at approximately 27°. The gold peak at 37°,[81] which was identified in the as-grown pattern, was also barely indiscernible in the brown layer. The black layer, shown as the middle pattern of Figure 4.2, had little crystalline content but displayed the broad amorphous peak at angles expected for boron and the crystalline gold peak at 37°.

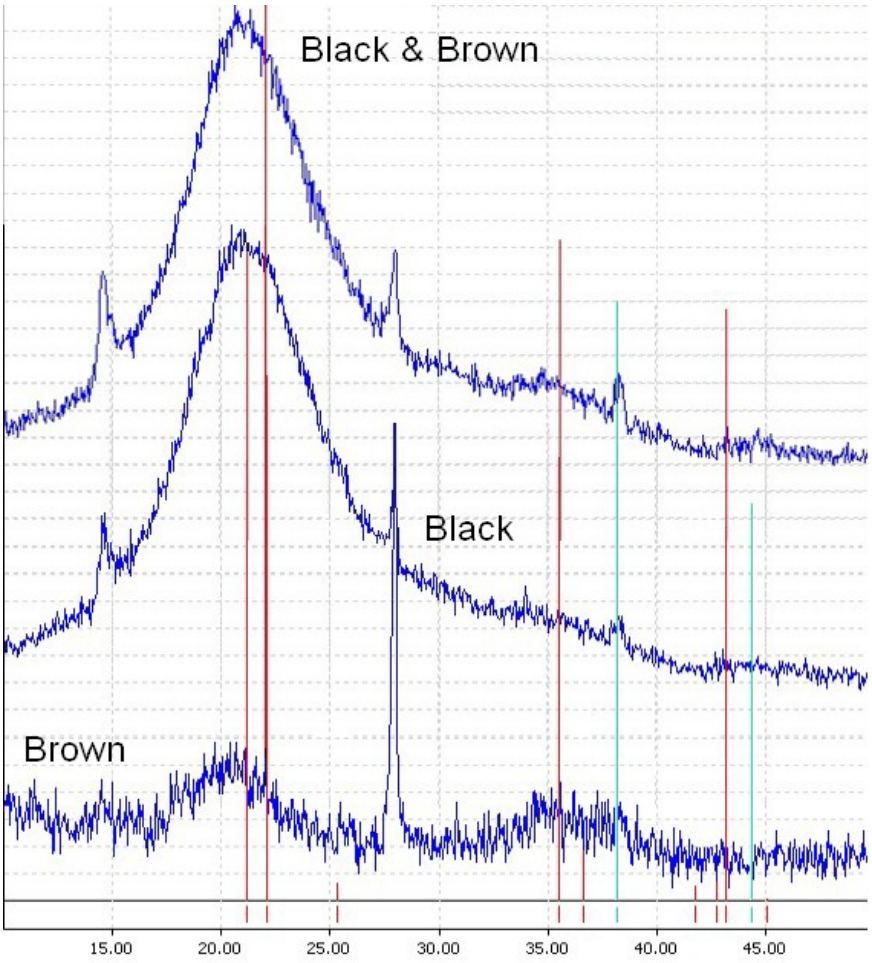

Figure 4.2: Typical experimental Set 1 powder x-ray diffraction results. Top pattern depicts the entire product as produced. Middle pattern depicts the black layer alone displaying a broad amorphous peak. Bottom pattern depicts the brown layer displaying a crystalline peak at 27°. Red lines are α-boron while the green lines indicate crystalline gold.[81]

Based on the pattern analysis it was concluded that the Set 1 synthetic procedure was unsuccessful at producing α-boron and that some quantity of gold had crystallized.

To determine the cause of the poor results of this synthesis, the theoretical Au-B phase diagram,[82] reproduced in Figure 4.3, was reviewed for underlying behaviours.

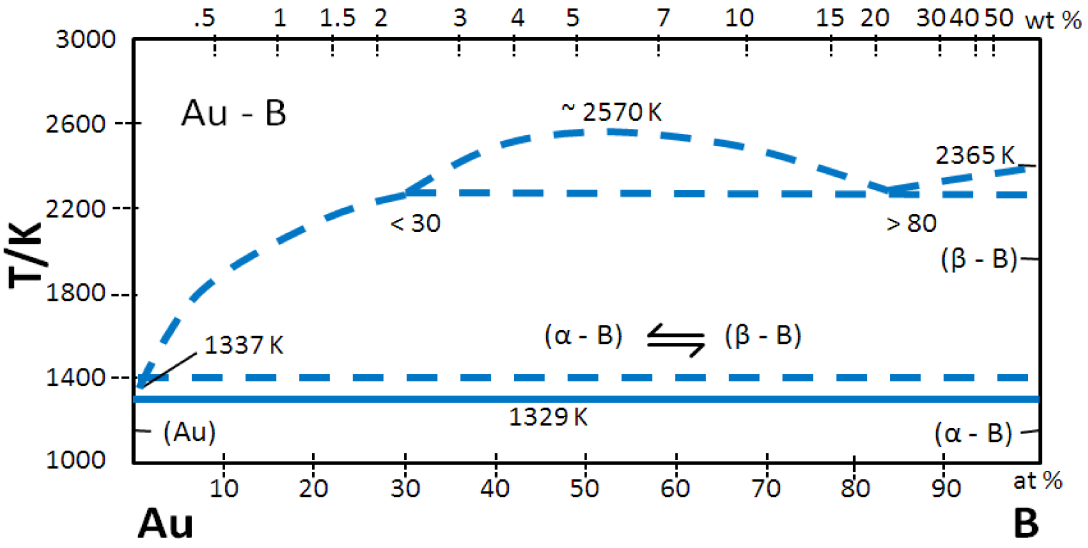

Figure 4.3: Theoretical binary phase diagram of gold and boron adapted from Okamoto et al.[82] Dotted lines represent theoretical phase separation, solid lines are experimentally known.

Based on the findings of Okamoto *et al.*,[82] gold would only be a suitable liquid solution at 1337 K (1064 °C). This theoretical operating temperature (1337 K) was within the range of the furnace however it was not attempted due to safety concerns that arose around operating above 1000 °C with flammable gases in quartz. Experimental staff cautioned that the quartz reaction chamber would become slightly air permeable above 1000 °C. It was concluded that operating at a lower temperature using a better understood liquid metal reagent would be preferred.

Considering these experimental constraints, a study of boron-metal binary phase diagrams revealed platinum as a passable candidate. The platinum-boron phase diagram is a well understood, experimental phase diagram and is shown in Figure 4.4.[83,84,85,86] The relatively low liquidus would allow for a safer operating temperature of 1063 K (790 °C). This decision was reinforced by the work of Sitarik *et al.*[50] which had employed platinum for α-boron VLS. The next Set of experiments was performed with platinum as the liquid reagent. In the interests of finding a less costly material for the reagent, lead was also used.

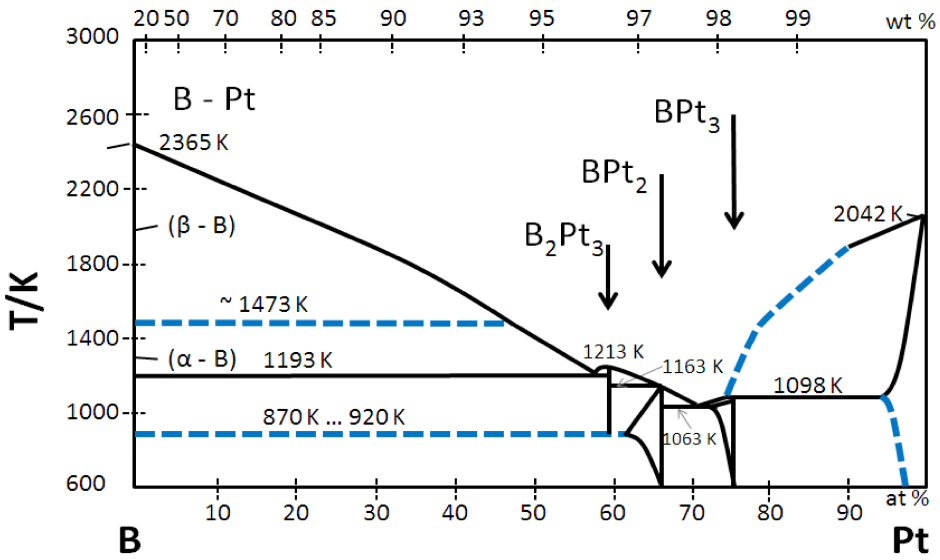

Figure 4.4: Binary phase diagram for platinum and boron. Adapted from references 83,84,85,86.

Note that both phase diagrams list a transition temperature for α-boron to β-boron at temperatures different from previously reported literature. This will be discussed more fully in chapter Chapter 4.

4.1.1.2 Set 2 Experiments – VLS Success

The Set 2 experiments began with an attempt to use granular lead powder as a reagent while awaiting a source of platinum. The attempt was unsuccessful, it yielded no deposition of any significance and was quickly abandoned.

The platinum experiments employed platinum liquid metal, $BBr_{3(l)}$ as a boron source, and operated at 900 °C. The initial results were promising; optical microscope analysis using the BH2 Olympus Metalurgical microscope and attached 12 Mpixil digital camera, displayed the whisker structures, expected by VLS theory, as seen in Figure 4.5.

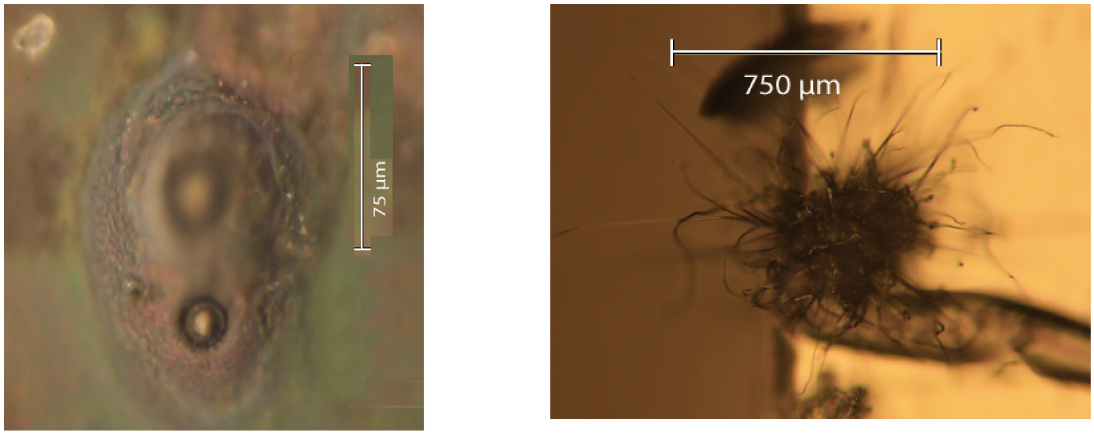

Figure 4.5: α-boron whisker growth via VLS synthesis. Left image via optical microscope. Circular depression indicates the Pt liquid-metal. Right image along edge of substrate.

The XRD pattern, given in Figure 4.6, shows that the product did not contain appreciable amounts of α-boron and instead displayed undesired contaminants which are described in detail in Figure 4.7.

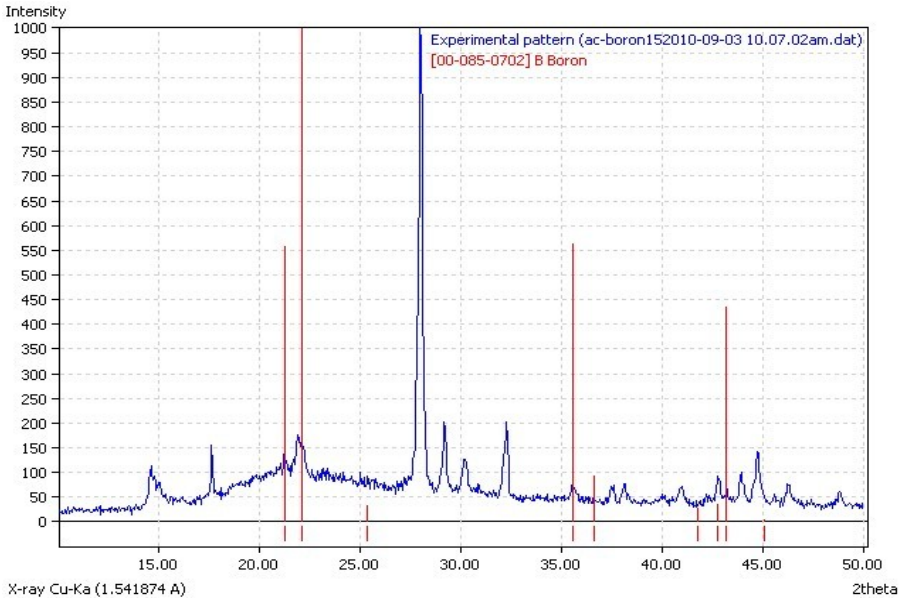

Figure 4.6: XRD pattern of experiment 7 α-boron synthesis using platinum as liquid metal. Red lines show the peak positions of α-boron,[77] indicating generation of crystalline boron in negligible amounts.

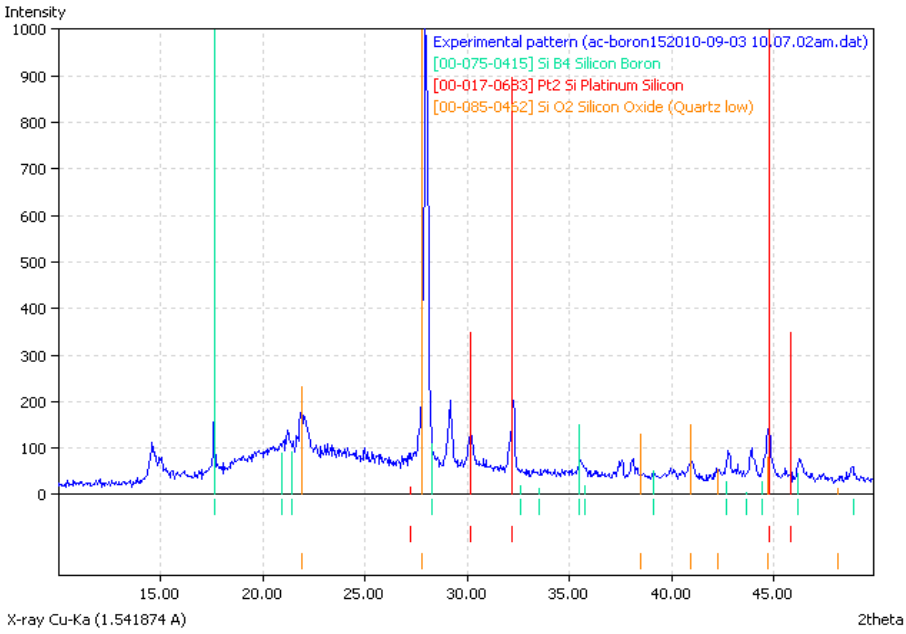

Figure 4.7: XRD pattern of attempted α-boron synthesis using platinum as liquid metal. Multiple theoretical assignments to the unknown peaks are suggested as explanation of contaminants. Red lines are Pt_2Si,[87] green are SiB_4,[88] and orange are SiO_2 (quartz).[89]

The contaminant peaks of Figure 4.7 displayed reasonable agreement with a form of platinum silicon[87], boron silicon[88] and quartz.[89] Decomposition of the quartz substrate seemed the most likely source of the contaminants, especially in light of the work by Agaogullari *et al.*[90] which describes boron vapour reducing SiO_2 to Si.

While analyzing the experimental results to determine sources of contamination, it became apparent that the bubbler apparatus had been damaged. Specifically the valve marked 'x' on Figure 4.8, the quarter-turn valve, was no longer functioning as intended. The o-ring had decayed making it impossible to seal off the bubbler reservoir from the purge gas bypass. The back pressure caused by the flow of purge gas lead to a loss of boron source, and contamination of the inner chamber with unknown side reactions.

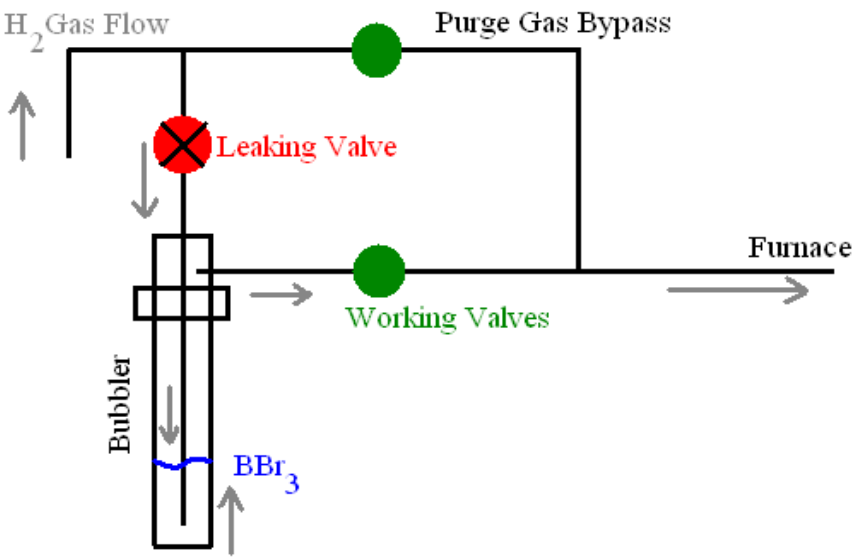

Figure 4.8: Schematic of the bubbler used in VLS experiments. Valve marked in red was discovered damaged during Set 3 experiments.

Due to the damaged bubbler and presence of contaminants experimental results demonstrated the unoptimized successful synthesis of α-boron via the VLS method while employing platinum as the liquid metal and boron tribromide as the boron source.

4.1.1.3 X-ray Spectroscopy Results

The crystalline peak at approximately 27º was apparent in all XRD analyses of the products of VLS synthesis. The XRD pattern assignment in Figure 4.7 shows that this peak fits well with that expected for crystalline quartz.[91] One explanation is that some local quartz crystallization could have occurred during the experiment, however a few factors made that scenario unlikely. First the peak strength across the sets remained intense, implying substantial crystallization. Secondly there was only one peak in the XRD pattern consistent with quartz, which gave little confidence to an accurate assignment. In response to these challenges in characterizing samples it was decided to employ x-ray spectroscopy, specifically EDS, for quantitative analysis.

Initial efforts began with SEM and focused on visual analysis to identify features and attributes that might explain the system. Figure 4.9 shows the typical Set 1 and Set 2 VLS chamber wall sample at low magnification. It became readily apparent that the long fibers and tiny granules were key features, each of which can be seen in the magnified view of Figure 4.10. Further efforts were undertaken to analyze the elemental composition of select locations since consideration of the optical image alone did not answer the unknown peak question.

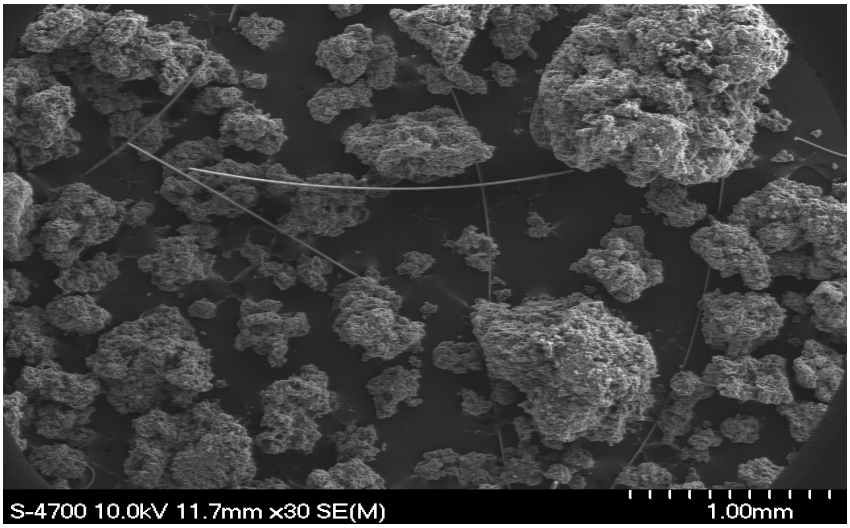

Figure 4.9: SEM image of typical Set 1 and 2 product from VLS techniques. Note long fibres and particles.

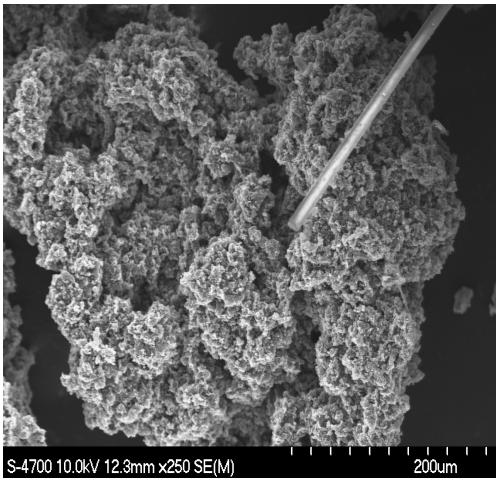

Figure 4.10: SEM image showing magnified view of a long fibre and granule. Composition of fibre was later found from EDS to be SiO_2.

Figure 4.11 displays results of the EDS analysis that indicate the percentage of observed elements in the long fibres, while Figure 4.12 gives EDS results of the granules. The prevalence of silicon and oxygen in Figure 4.11 implies the fibre-like structures are

silicon dioxide. The XRD pattern assignment of the 27º peak indicated crystalline quartz, which is now strengthened by these compositional results. Figure 4.12 shows that the granules are mostly boron with a small amount of SiO_2 impurity.

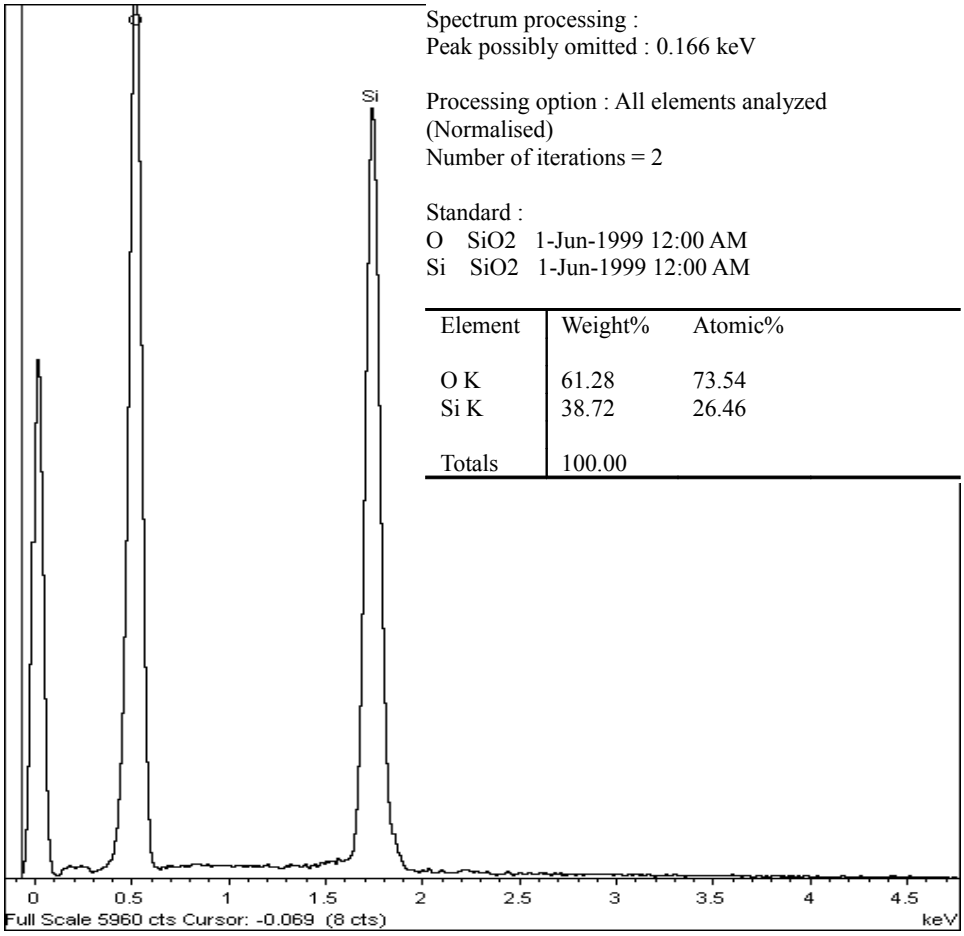

Figure 4.11: EDS results for the fibre-like structures seen in Figure 4.10. Presence of oxygen and silicon strongly suggests SiO_2. The peak at 0 indicates beryllium, used as a filtration window on the detector.

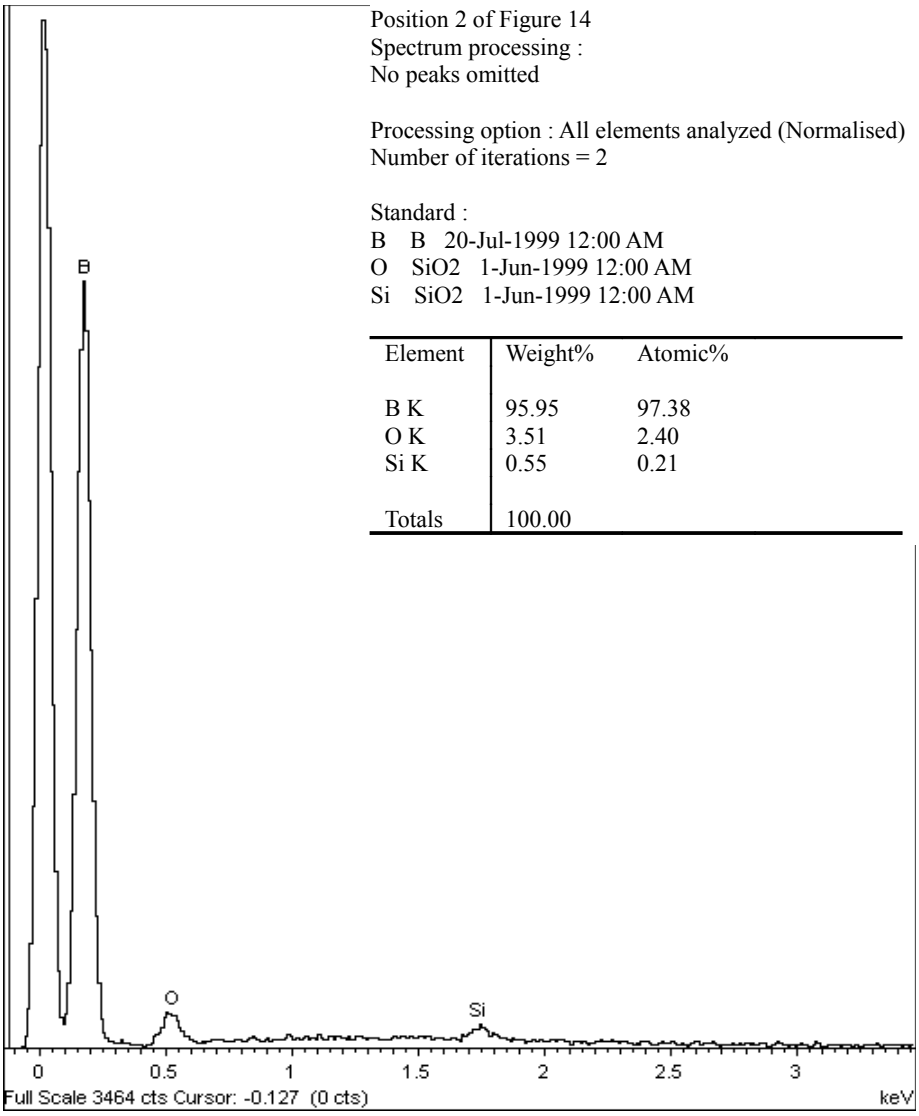

Figure 4.12: EDS results for the granule depicted in Figure 4.10. The large presence of the boron peak strongly indicates boron granules with small amounts of SiO_2 impurities. The peak at 0 indicates beryllium, used as a filtration window on the detector.

Given the fibre-like morphology, a possible source of contamination was the quartz wool used as a thermal shield in the furnace. It is possible some of the glass wool fibres entered the chamber and deposited with the product. Since the EDS results provide strong indication of SiO_2 fibres, a sample of the wool was studied via XRD to determine

the morphology. No discernible crystalline morphology was detected from XRD as can be seen in Figure 4.13.

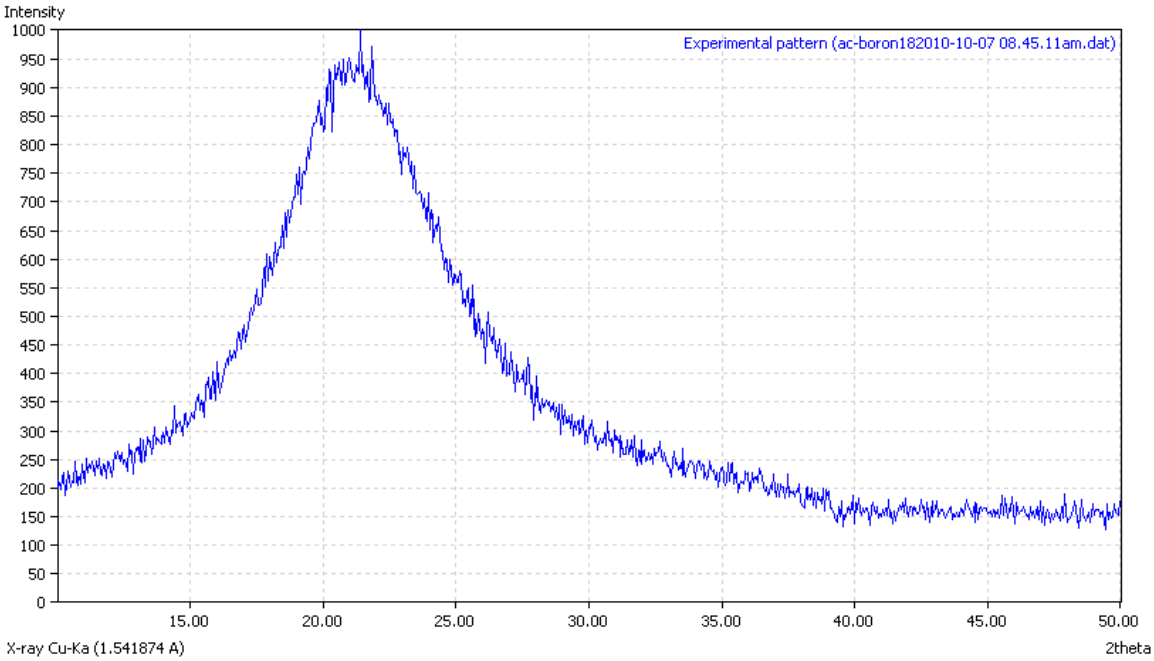

Figure 4.13: XRD pattern of quartz wool radiation shield. No discernible crystalline morphology detected.

Despite the fact that the non-crystalline glass wool cannot be directly linked to crystalline contamination in the product, it is possible that under the operating conditions of the experiments some small amount of glass wool might crystallize. Thus the fibres were removed from the sample and an XRD was collected. To do this, a small quantity of powder was deposited on weigh paper and slowly tapped onto a second and then third piece of weigh paper to separate the whiskers from the quasi-spherical boron particles. As a final step the resulting boron powder was considered under an optical microscope to locate and remove any remaining fibres with forceps. The XRD pattern of the resulting

purified sample is displayed in Figure 4.14 revealing the pattern matching pure α-boron. Note the loss of the 27° peak, attributed to the removal of crystalline quartz fibres. Care was taken in subsequent experiments to ensure that the glass fibre no longer contaminated the products.

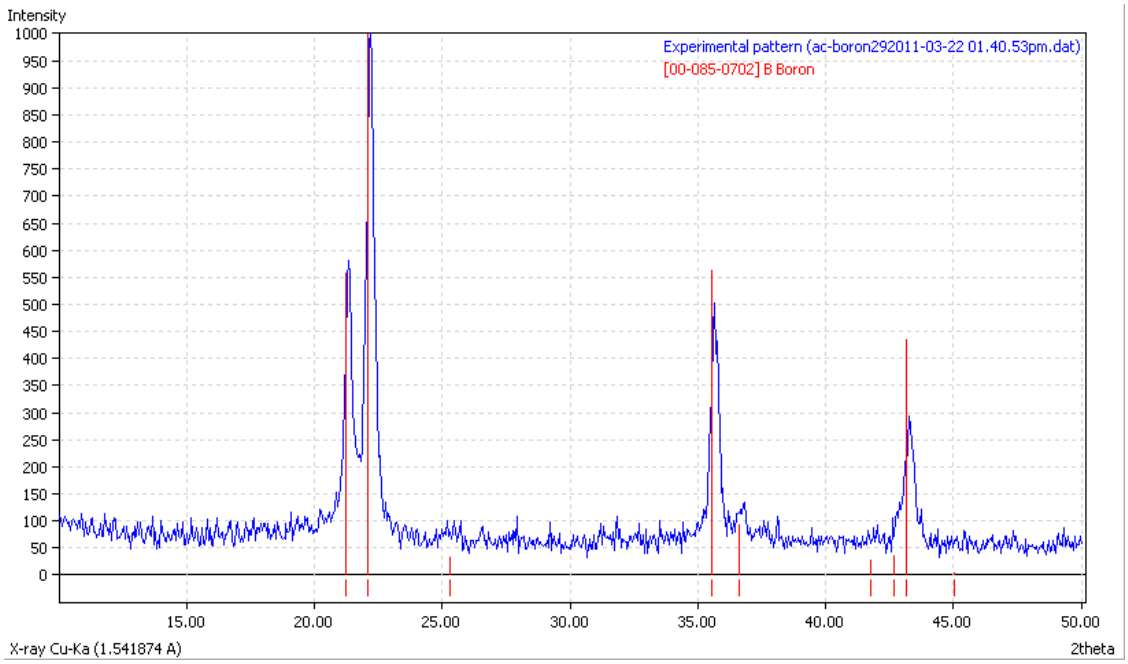

Figure 4.14: XRD pattern of purified VLS sample taken from the walls of reaction chamber. Red peaks are α-boron.[77]

As the quartz wool radiation shield was required to protect the apparatus, effort was directed to minimize the contamination from the fibres. Each experiment employed the same set of wool shields, and it was discovered that over multiple syntheses the fibres available to enter the chamber had decreased. Fortuitously the contamination issue had solved itself.

4.1.1.4 Novel Synthesis Discovery

The leaking valve mentioned in 4.1.1.2 was discovered while exploring an unexpected observation. During efforts to synthesize α-boron using VLS Set 1 and Set 2 there had been a steady deposition along the reaction chamber walls instead of on the substrate. The black deposit that was removed and studied by XRD and all samples displayed similar patterns, as seen is Figure 4.15.

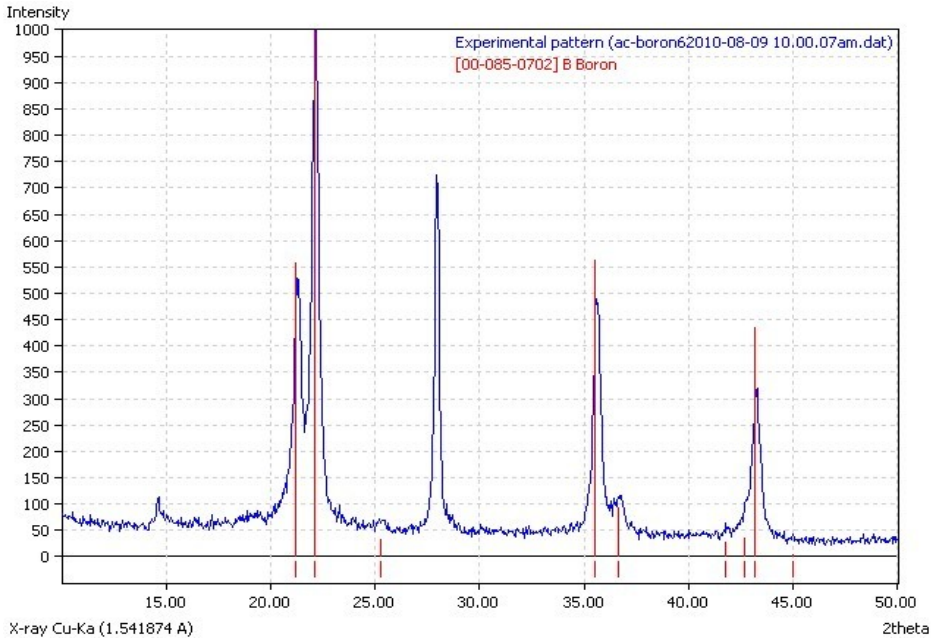

Figure 4.15: Typical XRD pattern for sample deposited on walls of reaction chamber for VLS experiments. Red peaks indicate α-boron;[77] unmarked peaks discussed in the text to be SiO_2.

The resulting pattern displayed good agreement to XRD reference α-boron,[77] save a quartz contamination, as detailed in the preceding section. Further, this product found on the walls was a marked improvement over the products recovered while attempting the well documented VLS synthesis.

The theory of VLS held that without the metal liquid (Au, Pt, etc.) boron could not crystallize into the α-phase. Despite this theoretical opposition, α-boron was collected from the chamber walls in substantial quantities from every VLS reaction, and further the growth of crystalline material was minimal on the substrate.

At the time of the experiments there was no mention in the literature of α-boron forming on quartz under these experimental conditions. The discovery of this unexpected synthetic method, a form of CVD, prompted the investigation of the secondary α-boron synthetic approach.

4.1.2 CVD Method

The evolution of the synthetic method from VLS was a careful transition based on observations and patient experimentation, not on previous experimental findings from literature. A recent addition to the field of boron synthesis closely mirrors the method that was used here. The work by Agaogullari *et al.*,[90] published in June of 2011, explains the synthesis of crystalline boron through use of CVD. The research focused on the synthesis itself, exploring the mechanism in a manner that was beyond the scope of this project. The discovery of the new synthetic method described in this thesis was driven by the desire to produce pure α-boron with minimal interest in the exact mechanism. The precise efforts employed in this work to understand the new synthetic method are outlined in the proceeding sections; many aspects are verified by the work of Agaogullari *et al.*,[90] while others are novel directions not considered in the literature.

4.1.2.1 Set 3 Experiments – CVD Transition

Initially the Set 3 experiments attempted to reproduce the successes of Set 2 VLS synthesis with the new boron source gas. However, when product was found deposited on the reaction chamber wall, the focus was to optimize CVD synthesis.

The change from using $BBr_{3(l)}$ to $BCl_{3(g)}$ as boron source necessitated a modification to the apparatus outlined in section 3.1.1.2. The change mainly consisted of replacing the bubbler with gas feed lines. Once this was complete, efforts were directed to optimize the Set 2 VLS experiments. Replication of the experimental set-up that lead to nominally favourable results did not produce appreciable success seen from the XRD pattern of the product in Figure 4.16. The growth of crystalline α-boron deposit on the walls of the chamber was not observed under the new operating conditions. The deposits only contained amorphous products as seen is Figure 4.16.

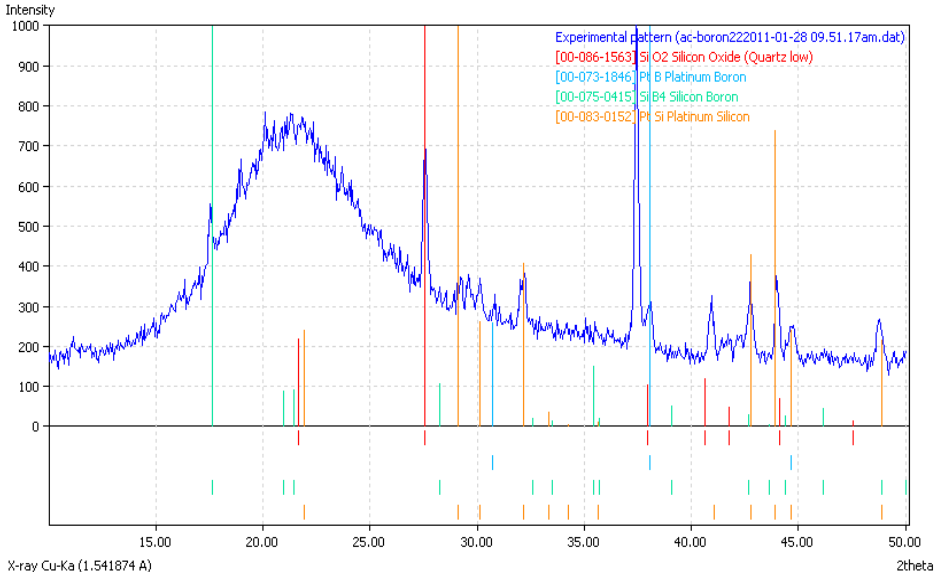

Figure 4.16: XRD pattern of typical Set 4 synthetic results employing the new BCl_3 boron source. Lack of α-boron crystallization and presence of unfavourable contaminants prompted modifications.

The presence of the contaminants platinum boron,[92] boron silicon,[88] and platinum silicon[87] from side reactions prompted the use of a temperature gradient within the reaction chamber. The centre of the furnace was 900 °C with a decrease of 5 °C per cm measured using an external thermal couple during a dry run with identical settings. The results on the substrate remained unchanged however the walls of the chamber displayed increased deposition which provided an XRD pattern as shown in Figure 4.17.

The formation of both *α*-boron and *β*-boron crystal was unexpected. The discovery of the novel approach, and lack of success reproducing the VLS result with the new boron source led to focused efforts on improving the chamber wall synthesis, *i.e.*, the CVD method.

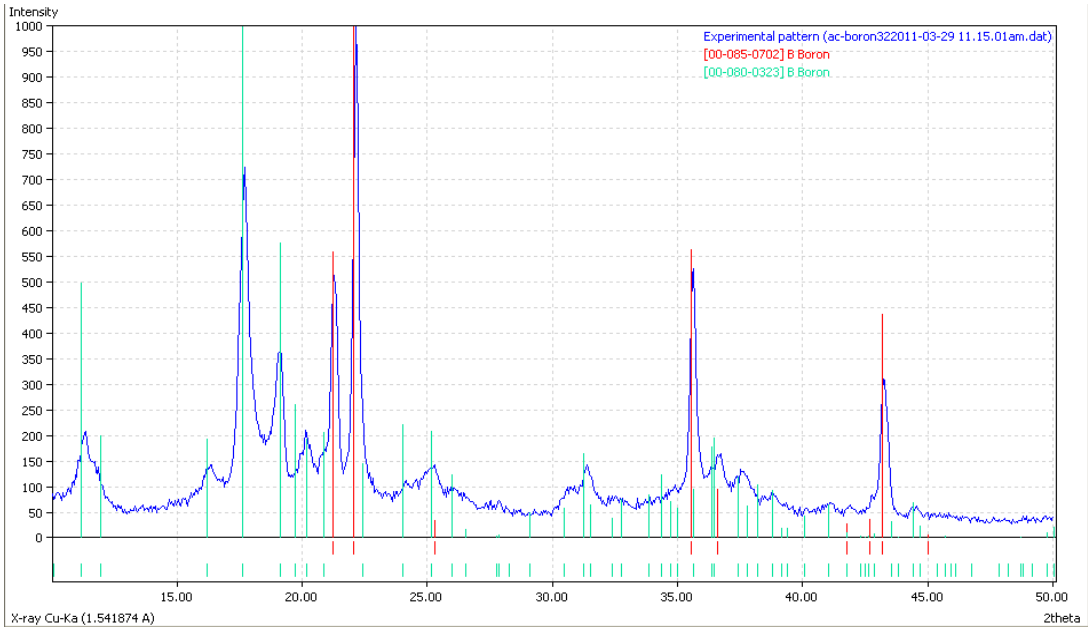

Figure 4.17: XRD pattern of product removed from the walls of the chamber under temperature gradient conditions. The crystalline sample displays both α-boron (red)[77] and β-boron (green) character.[78]

4.1.2.2 Set 4 Experiments - Temperature Profile

As mentioned previously, literature has inconsistent reports of the temperature for the transition of β-boron from α-boron. Some works list 1913 K[16] or 1985 K[17] while others find 1337 K[82] and even 1193 K[83] as the transition temperature. Previous research employing VLS synthesis placed β-boron formation at 1573 K (1300 °C).[50,73,85] Thus the presence of β-boron at 1173 K (900 °C) was considered atypical and implied that the transition between the allotropes was kinetically restricted.[18] Under these conditions it was considered plausible that lower temperatures might halt the crystallization of β-boron. The different temperatures zones of the gradient experiment may provide different synthetic results, which led to the introduction of a segmented cylinder as explained in 3.1.1.2. The insertion of a segmented cylinder into the chamber allowed collection at the product of each discrete temperature zone.

As can be seen in Table 4.2 and Figure 4.18, position 2, which corresponds to approximately 850 °C, resulted in α-boron with no measureable β-boron contamination. The percentage of β-boron was estimated by comparing the relative XRD peak intensity of β-boron at 17° and α-boron at 23°, as seen in Figure 4.19. This ratio was considered a reasonable approximation for the crystalline forms with the same basic elemental composition, to scale intensity with concentration.

Table 4.2: CVD synthesis temperature profile. Distances are measured from opening of furnace. % β is derived from the relative intensities of the 19° β -boron *peak vs the 23° α-boron peak.*

Position	Distance	% β	*T* /°C
1	22	2.8	842
2	24	0	854
3	26.3	2.5	867
4	28.85	3.9	882
5	31.6	7.1	903
6	34.6	11.6	917

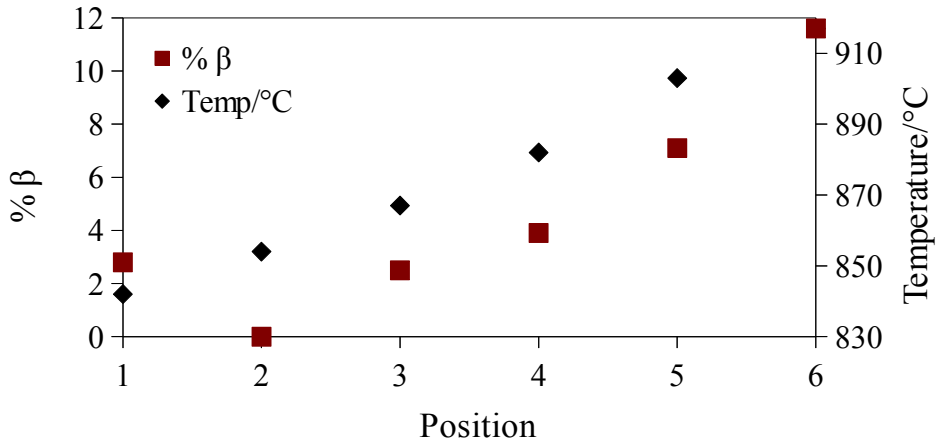

Figure 4.18: % β-boron and temperature as a function of position in CVD synthesis.

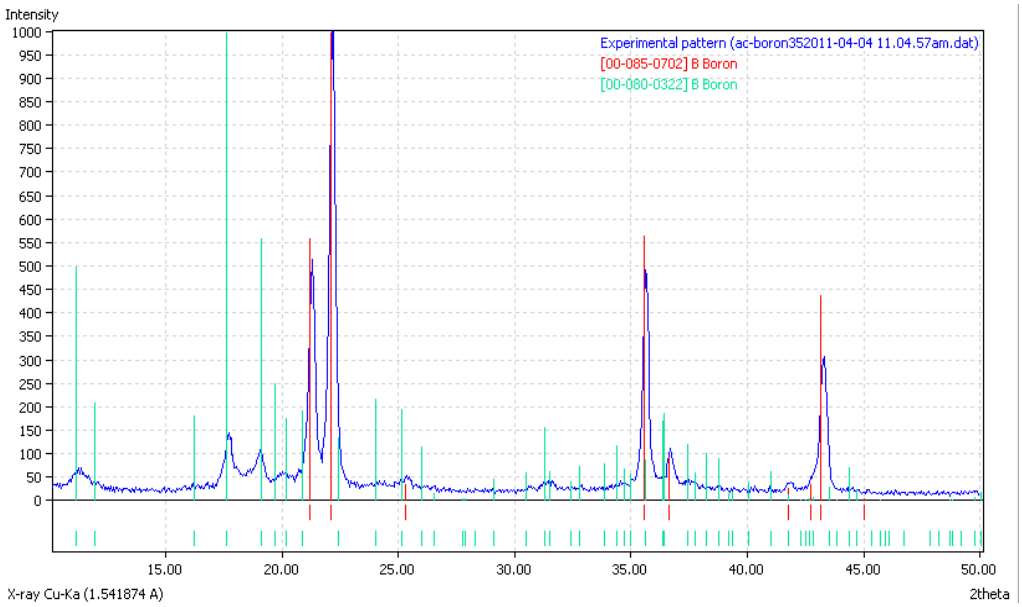

Figure 4.19: XRD pattern from sixth zone of temperature profile (917 °C) which gave the most prominent β-boron peaks of all positions.

Once the ideal temperature of 850 °C was identified, efforts turned toward production of larger amounts of pure α-boron. The non-contaminated XRD pattern is shown in Figure 4.20.

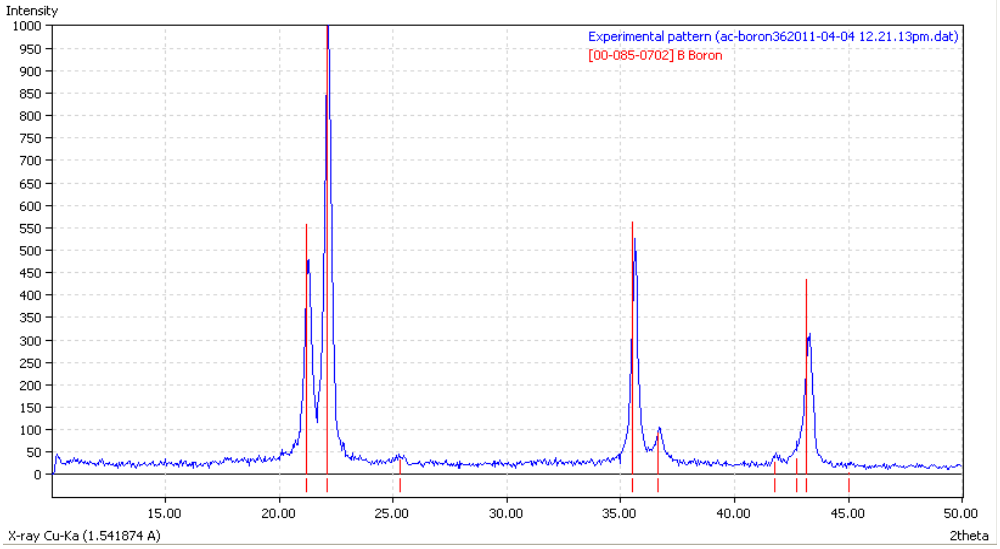

Figure 4.20: XRD pattern from the second zone of the temperature profile, which shows no appreciable β-boron presence.

The work of Agaogullari *et al.*, expressed concerns with crystalline quartz contamination of their samples, determined to be 0.175%, which were removed via hydrofluoric acid leaching.[90] The XRD pattern in Figure 4.20 indicated that the sample displayed no detectable contamination, but EDS analysis was used to find any non-crystalline impurities that might be present. The results of the EDS analysis are given in Figure 4.21.

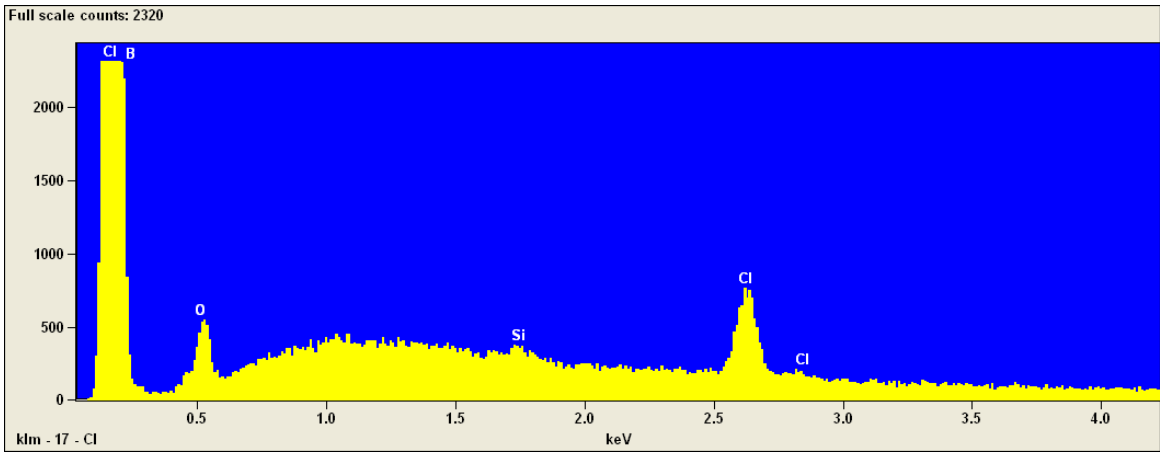

Figure 4.21: Qualitative EDS analysis of the α-boron pellet. Overlap of B/Cl peak limits quantification but the sample displays non-trivial amounts of chlorine.

The determination of *α*-boron purity by EDS was hindered by the overlap between B and Cl lines, specifically the boron K_α and the chlorine LN/LL.[93] The K_α transition represents the vacancy of a *K*-shell electron, which is filled via the *L*-shell, releasing a strong x-ray. Meanwhile the *LN* transition represents the vacancy of an L_{II}-shell, which is filled by the M_I; LL has the L_{III} open for M_I. The two combined chlorine transitions are first order, meaning they have a low scattering angle from the sample, but their probability of occurrence is so low as to rarely be a factor in measurements.[65] Due to the

fact that the CVD experiments used BCl_3 as the boron source, a small amount of chlorine was present in the material. The presence of chlorine and boron in the sample lead the EDS analysis software to attribute the boron K_α peak around 0.1 keV as the LN/LL chlorine transitions because of the chlorine K_α around 2.5 keV.

The overlapping effect was not observed during BBr_3 experimental Sets 1 & 2 as bromine does not share a transition. Further, as can be seen in earlier EDS experiments (Figure 4.12), bromine did not appear, suggesting that BBr_3 is a better boron source material, since it does not contaminate the product.

The presence of impurities lead to analysis of the α-boron sample via SEM, as shown in Figure 4.22, revealing long fibres with similar morphologies and compositions to quartz fibre as discussed in chapter 4.1.1.3. The presence of quartz fibre was unexpected given the lack of detectable crystalline quartz in XRD. Determining the atomic percent revealed 99.98% boron making contamination a quite low and beyond the expected detection capabilities of the XRD.

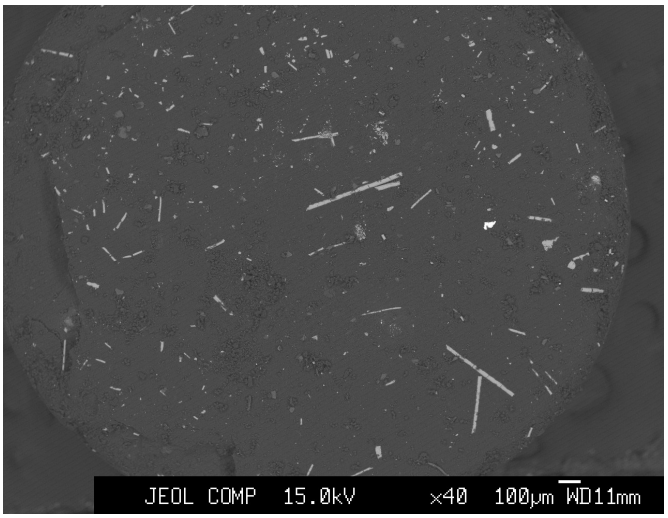

Figure 4.22: Back scattered electron SEM image of an α-boron pellet. Long fibres are quartz.

4.1.2.3 Set 5 Experiments – Production

Upon successful synthesis of pure α-boron via CVD, two separate experiments (14 & 15) generated α-boron for heat capacity measurements. Both samples were characterized by XRD and EDS as seen in Figure 4.21, 4.23 and 4.24.

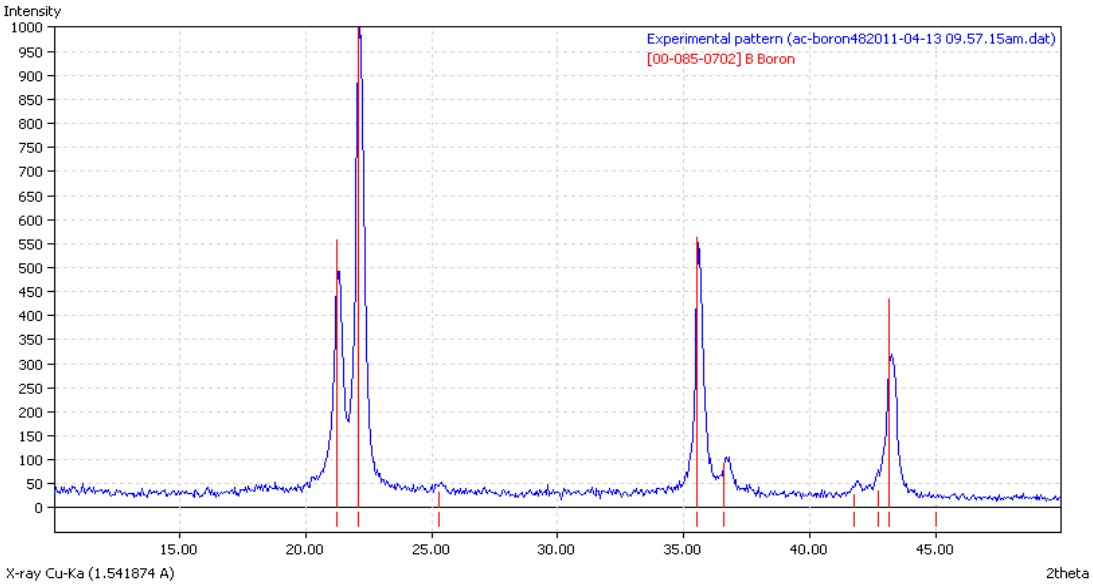

Figure 4.23: Characterization of α-boron from experiment 14.

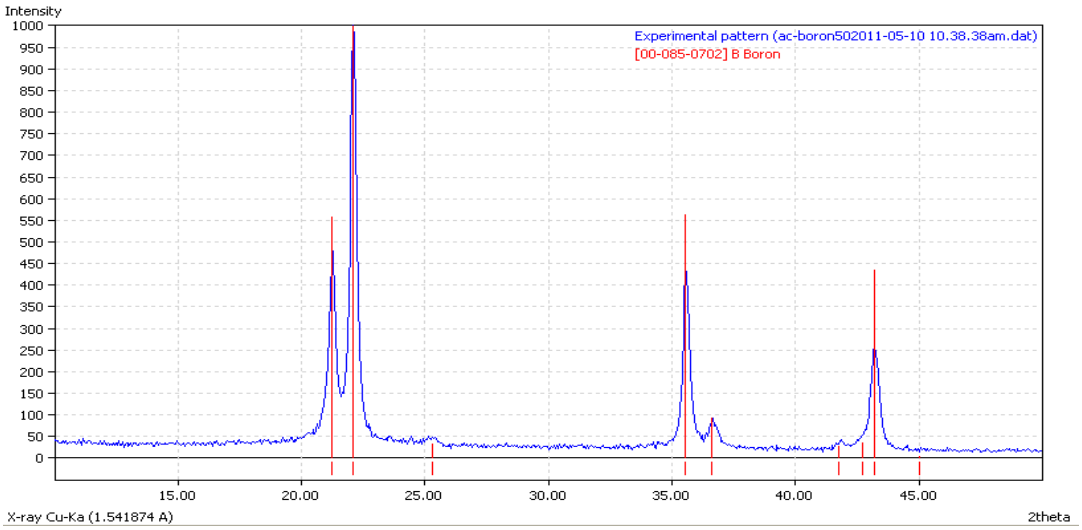

Figure 4.24: Characterization of α-boron from experiment 15.

4.1.2.4 Set 6 Experiments - Mechanism Investigation

In an attempt to explore the mechanism of α-boron synthesis, four efforts were employed: atmospheric exposure, addition of boron oxide catalyst, and cylinder surface analysis, and hydrolysis.

4.1.2.4.1 Atmospheric Exposure

As previously noted, the longer the VLS experiment, the more boron deposited on the walls of the chamber. Furthermore when transitioning to CVD experiments it was discovered that at least two experimental cycles were required to produce a good quantity of α-boron. In exploration of this trend, experiments 16 and 17 were twinned. Starting with a freshly purchased chamber, experiment 16 went through two synthetic cycles of heating with reagent flow and cooling. Unlike earlier experiments, there was minimal deposition, however because this was a new chamber, there was no exposure to atmosphere between the cycles. To further confirm exposure to atmosphere being a factor, experiment 17 employed the same chamber, which had now been exposed to atmosphere after experiencing a synthetic cycle. The result was that a large quantity of α-boron crystals was produced. Thus it was considered possible that a component in the atmosphere was responsible for the 'activation' of the quartz substrate for α-boron growth.

4.1.2.4.2 Boron Oxide Catalyst

In an effort to determine the catalysing agent implied by the results of experiments

16 and 17, a small quantity of boron oxide was placed in a fresh cylinder for experiment 18. The hypothesis was that a small quantity of boron had deposited on the quartz during the synthetic cycle and when exposed to atmosphere oxidized, it provided a deposition surface. The results showed no evidence of α-boron deposition within the cylinder. The boron oxide had become boric acid, but no α-boron was present.

4.1.2.4.3 Cylinder Surface Analysis

Final analysis was directed to the surface of the segmented quartz cylinder, which was taken to Daniel MacDonald for study via EDS. The goal was to determine if the black 'shadow' that deposited on the chamber walls was boron, or silicon.

It was noted in the work by Agaogullari *et al.*[90] that SiO_2 would be reduced to Si by elemental boron. Further, an earlier study by Nishizawa *et al.*[94] had demonstrated that adsorption of boron on the surface of SiO_2 was less than1% that of Si alone. Considering these factors, and the black, colour of the 'shadow', it was considered viable that a reduced section of SiO_2 was the substrate. The result of this analysis can be seen in Figure 4.25.

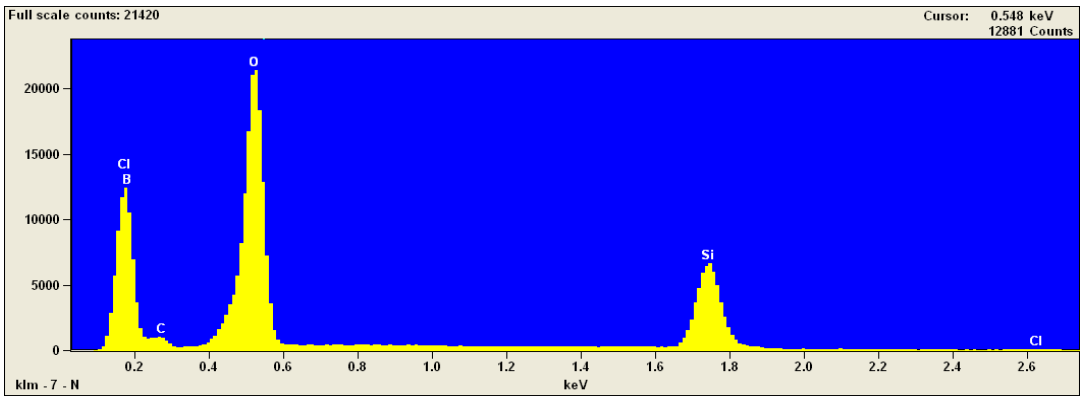

Figure 4.25: Qualitative EDS analysis of the black cylinder wall deposit. Overlap of B/Cl peak limits quantification but the sample displays strong boron character suggesting the black deposit includes boron.

The previously mentioned overlapping transitions of B/Cl in EDS limited efforts to qualitative determinate the amount of boron. However the presence of strong boron signal in the region of black deposition suggested the 'shadow' was boron and not silicon, thus discounting the proposed mechanism.

4.1.2.4.4 Hydrolysis

Experiment 19 was an attempt to add hydroxide to the surface of the quartz tube through saturation with sodium hydroxide. The hypothesis was that water in the atmosphere produced a surface layer of hydroxide on the quartz during exposure which would bind the reagent BCl_3 to the surface through the formation of HCl. No results were collected as the constriction of the waste line, explained below in more detail, caused pressure build up leading to a small fire within the chamber when the end cap released.

4.1.2.5 Waste Product

The change in boron source material from BBr_3 to BCl_3 introduced an unexpected waste product in the water traps. The white powdery substance formed initially within the entry pipe of the trap constricting the flow of waste gas. Over the time scale of hours the powder would dissolve into the acidic solution of HCl. The formation of this product was a safety concern as the constriction of the line lead to pressure build up in the system. Investigation of the material via XRD, as seen in Figure 4.26, revealed a good fit for synthetic sassolite ($B(OH)_3$).[95]

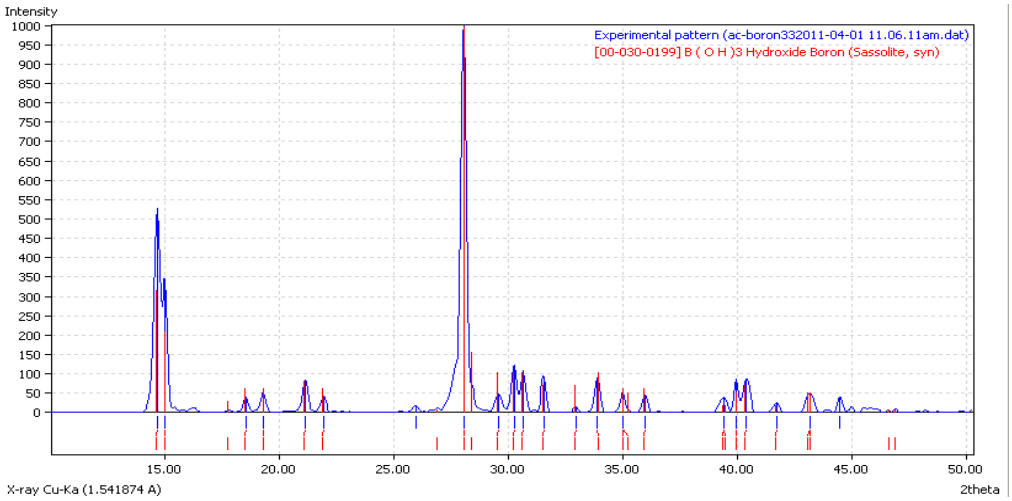

Figure 4.26: XRD pattern for white powder constricting the waste line. Red lines indicate synthetic sassolite $B(OH)_3$.[95]

As sassolite has no chlorine component, the presence of the material only after the boron source gas was altered implies a less direct mechanism. As the deposition synthesis mechanism was not a major focus of this work, the formation of sassolite was considered theoretically and no further experimentation to determine mechanism was attempted. The leading theory suggests that sassolite, being the mineral form of the weak boric acid, would dissociate in the water trap. However the strength of the halogen acids would lead to their dissociation first which could saturate the trap. Since the flow of BCl_3 gas was higher than the flow of BBr_3 liquid, it is plausible that the increase in waste acid volume required an increase in trap volume to allow full containment of all products.

The determination of the waste product assisted in developing the stoichiometric equation for the synthesis. The work by Agaogullari *et al.*[90] had found the dissociation of boron trichloride and hydrogen into boron and hydrochloric acid to be:

$$BCl_{3(g)} + \frac{3}{2} H_{2(g)} \rightarrow B_{(s)} + 3HCl_{(g)} \quad . \qquad (4.1)$$

Agaogullari *et al.* had employed a continuous vacuum rather than a water trap. The addition of water to the waste stream made the formation of sassolite possible here via:

$$3BCl_{3(g)} + 3H_{2(g)} + 3H_2O_{(l)} \rightarrow 2B_{(s)} + 9HCl_{(g)} + B(OH)_{3(s)} \quad . \tag{4.2}$$

4.1.3 Synthesis Summary

VLS synthesis was successfully reproduced, using BBr_3 and platinum but yields and purities were insufficient to provide suitable samples for calorimetric measurements. The allotrope α-boron was successfully synthesized via the newly discovered CVD mechanism at 850 °C using BCl_3 with a final purity of 99.98%. Preliminary mechanistic investigation revealed exposure to atmosphere as a potentially vital step in the synthesis, but no conclusive evidence has been established. Note that β-boron was not synthesized but purchased commercially at 99.5% purity.

4.2 α-Boron Heat Capacity

Heat capacity measurements began upon successful synthesis of powdered α-boron crystals. The heat capacity of α-boron was measured at 10^{-4} Torr from 0.4 K to 400 K after pressing the crystal powder, as explained in section 3.3. Four separate samples were prepared from two synthetic runs. Samples of masses 9.45 mg, 10.25 mg and 10.18 mg were from experiment 14, while a 9.83 mg sample was from experiment 15. Sample masses were relatively large to encourage sample contributions to the heat capacity greater than 20%. Measurements were considered acceptable with a degree of thermal

contact between the sample and the platform greater than 80%. Figure 4.27 gives heat capacity of α-boron as a function of temperature over the entire temperature range (data in Appendix A) while Figure 4.28 displays the contribution of sample against the background. The accuracy of the PPMS was found to be 1% along the range of 5 K to 300 K and 5% for the range 0.7 K to 5 K with respect to literature standards of sapphire and copper.[58] Uncertainties in the measurement were calculated using standard propagation errors from the addenda, sample mass and sample heat capacity. The uncertainty displayed precision similar to the accuracy with errors of 5% from 0.35 K to 5 K and 1% from 5 K to 400 K.[58]

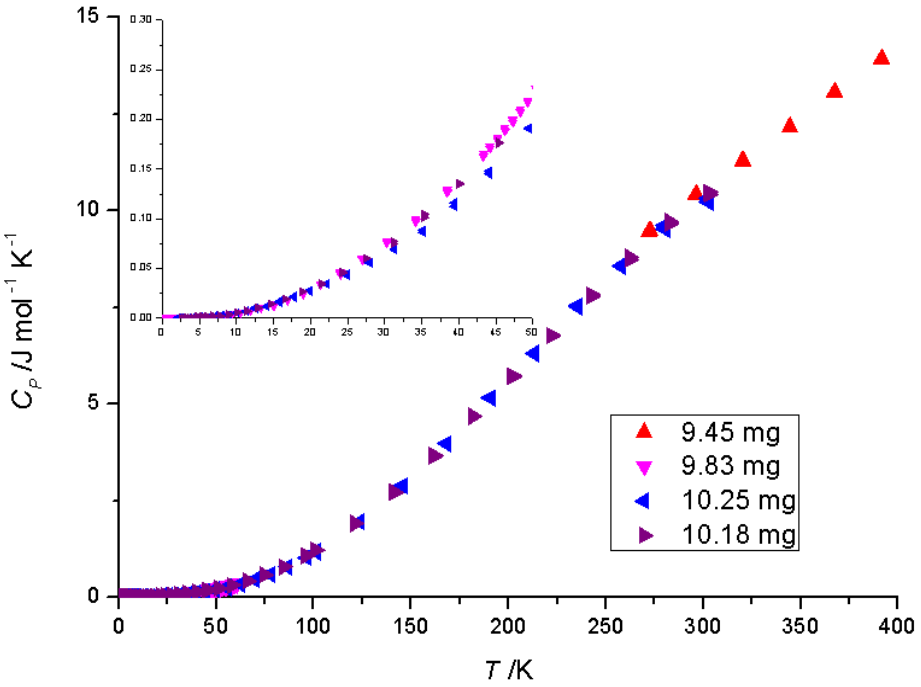

Figure 4.27: Experimentally determined α-boron heat capacity from 0.35 to 400 K. The measurements were collected on four samples of different mass seen in the legend. 9.83 mg used ^{3}He as the cryogenic liquid and synthetic run 15. All others used ^{4}He and synthetic run 14. Insert shows the area between 0 K and 50 K. Error bars are not visible as the symbol is larger.

During the course of experimental measurements it became apparent the thermally conducting grease responsible for the connection between the sample and platform was wicking into the pressed pellets of α-boron. This effect had a deleterious impact on the measurements for two reasons: first the systematic loss of sample coupling to the platform would result in unreliable measurements of the heat capacity, and secondly the presence of grease within the α-boron pellet meant the samples could not be reused. To minimize this wicking effect, the heat capacity was measured along a similar temperature range but with lower starting temperatures to decrease grease mobility.

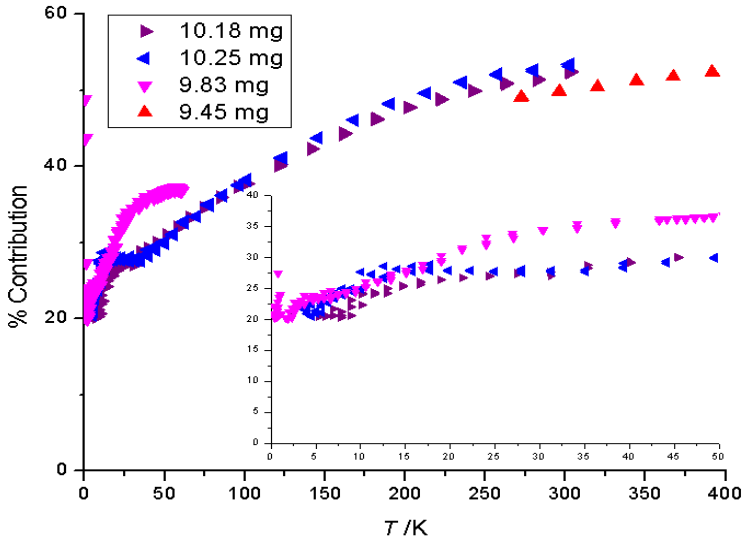

Figure 4.28: Experimentally determined α-boron heat capacity contribution to the total heat capacity from 0.35 to 400 K. Insert shows the area between 0 K and 50 K.

4.2.1 Literature Comparison

Within the literature there are only two published studies of α-boron heat capacity, compiled 10 years apart as a collaboration between the groups of Tsagareishvili *et al.*[96] and Naumov *et al.*[97] The earlier work of Tsagareishvili *et al.*[96] reported α-boron heat

capacity in 1986 using a 2.0640 g sample across the range from 16.05 K to 714.5 K via isothermal calorimetry. The resulting temperature-dependent heat capacity had a gap between 320 K to 400 K, and showed no alignment between the lower and upper data sets. The higher values also showed no sign of levelling off. The later work of Naumov *et al.*[97] in 1997 reexamined the temperature range from 16.05 K to 317.96 K with adiabatic calorimetry. Both of the literature results can be seen in Figure 4.29.

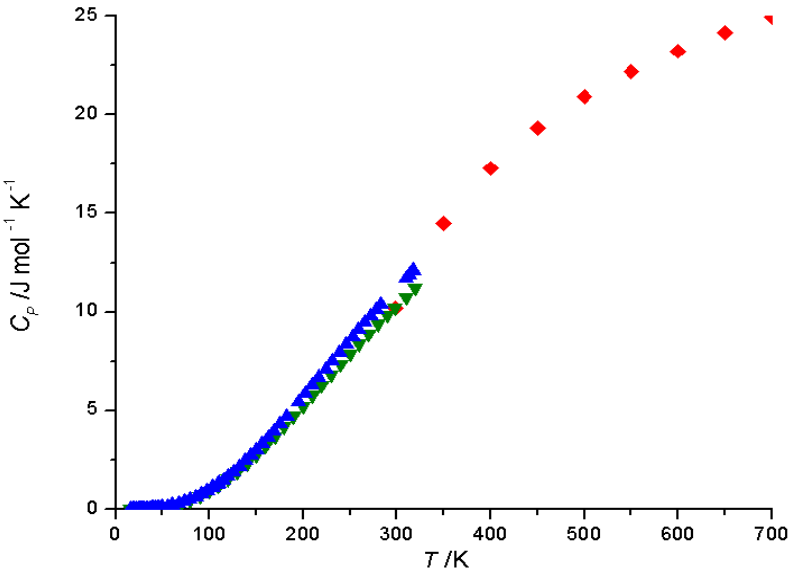

Figure 4.29: α-boron heat capacity at constant pressure from literature. ▼ and ◆ are from Tsagareishvili et al.,[96] and ▲ are from the later result of Naumov et al.[97]

Naumov *et al.*[97] extended their heat capacity results to 1450 K via Debye calculations. The resulting heat capacities at constant volume were approximated to C_P due to the high calculated Debye temperatures (1200 to 1600 K). A small shoulder was observed in the Naumov *et al.*[97] and Tsagareishvili *et al.*[96]data at approximately 33 K which required graphing along C_P/T vs. T^2 to be resolvable. The shoulder remained

unidentified in the literature and is not apparent in current measurements as can be seen in Figure 4.30.

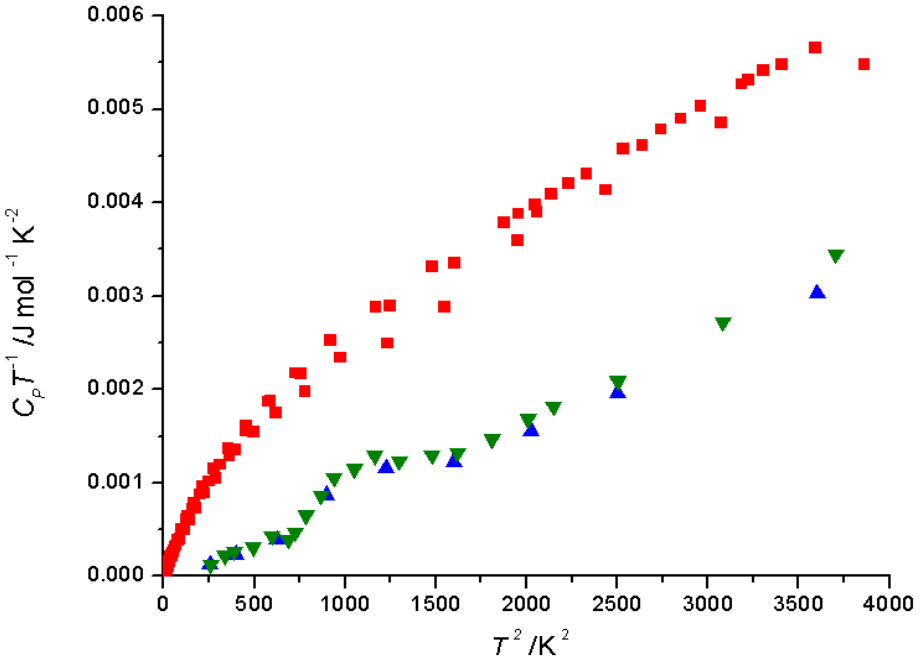

Figure 4.30: α-boron heat capacity with respect to temperature from literature and experiment. ▲ Naumov et al.,[97] and ▼ Tsagareishvili et al.[96] ■ are current experimental work. The Naumov et al. peak is located around T = 33 K, T^2 = 1089 K^2.

Both Tsagareishvili *et al.*[96] and Naumov *et al.*[97] smoothed their data to produce a more general curve but Tsagareishvili *et al.*[96] did not report the original data. The work of Tsagareishvili *et al.*[96] also contains sparse information on their source of α-boron or the steps taken to verify purity. Further the chamber of the calorimeter was not sealed from atmosphere so the 2.0640 g sample was also coated with 0.4900 g of Al_2O_3 to protect it from oxidation. This measure was unsuccessful as Tsagareishvili *et al.*[96] halted their experimentation at 714.5 K due to considerable sample mass increase. The exact mass increase was not mentioned. Despite the later work by Naumov *et al.*[97] being accomplished by the same authors as the previous work by Tsagareishvili *et al.*[96] there

was no mention of the 1986 reference. It was decided due to a combination of all mentioned factors to discount the early work of Tsagareishvili *et al.*[96] when comparing literature and experimental heat capacities.

Comparing current experimental work with the findings of Naumov *et al.*[97] (Figure 4.31) demonstrates reasonable agreement within the range of 100 K to 200 K; however outside this range results differ. The current measurements generally display higher heat capacity results than literature for $T < 100$ K, and for $T > 200$ K the current results fall below the published results. Figure 4.31 shows the literature results with the current experimental findings up to 300 K while Figure 4.32 shows the difference between experimental and literature results.

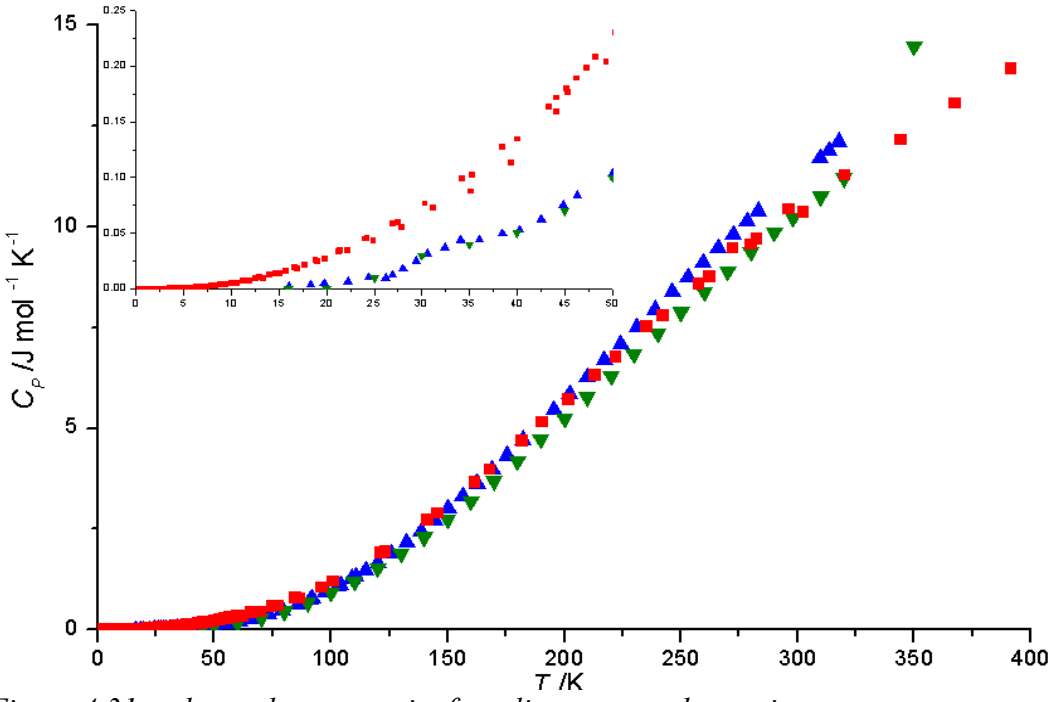

Figure 4.31: α-boron heat capacity from literature and experiment. ▼ are Tsagareishvili et al.,[96] ▲ Naumov et al.,[97] ■ are current experimental work. The insert shows the range from 0 K to 50 K.

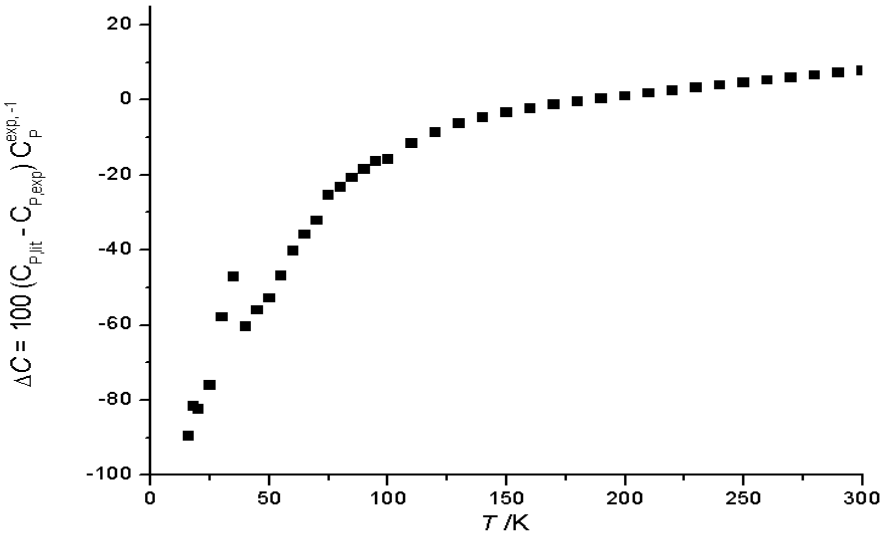

Figure 4.32: Percent deviation between Naumov et al.,[97] and current experimental α-boron measurements from 0 to 400 K.

The percent deviation of heat capacity values, ΔC, is calculated via

$$\Delta C = \left(\frac{C_{P,lit} - C_{P,\exp}}{C_{P,\exp}} \right) 100 \tag{4.3}$$

where $C_{P,lit}$ is the literature result at some temperature and $C_{P,exp}$ is the current measurement at that temperature.

As α-boron is relatively unexplored, there are difficulties in objectively studying these differences however, comparison of the employed experimental techniques offers some insight. Naumov *et al.*[97] used adiabatic calorimetry, and although a powerful technique it was time intensive and therefore resulted in less data density and fewer individual runs than can be carried out with more modern equipment. The samples were formed via annealing of amorphous boron powder at 1470 K. This synthetic approach remains largely unknown in the literature and confirmation of purity was restricted to XRD making it difficult to compare the sample purities.[97] Overall the agreement between

the better literature values[97] and the present data is good for 100 K to 200 K and the present relaxation calorimetry is more reliable than adiabatic calorimetry at low temperatures.

4.3 *β*-Boron Heat Capacity

β-boron heat capacity was collected in the temperature range from 0.4 K to 400 K from samples cut as outlined in section 3.3. Sample masses ranged from 5.26 mg to 37.57 mg and were all prepared from the same commercial sample. As the sample was a consolidated polycrystalline solid there was no need for pressing and thus there were no pores for the thermally conducting grease to wick into, meaning the samples could be reused. Of key interest, samples 35.70/35.64 mg and 37.57/31.62 mg were the same respectively. The loss of mass in the 35.70/35.64 case was the removal of a 0.06 mg chip of epoxy. The 37.57/31.62 mg change was caused by the reshaping of the original sample dimensions. The heat capacity results can be seen in Figure 4.33 (data in Appendix B) while the sample contribution is presented in Figure 4.34. Samples are listed in order of measurement collection and only measurements with sample contributions above 20% and coupling to the platform of 80% are presented.

Samples were run multiple times to check measurement consistency As noted the accuracy of the PPMS was found to be 1% along the range of 5 K to 300 K and 5% for the range 0.7 K to 5 K with respect to literature standards of sapphire and copper.[58] While the uncertainties in the measurement, calculated using standard propagation errors from the addenda, sample mass and sample heat capacity, displayed precision similar to the

accuracy with errors of 5% from 0.35 K to 5 K and 1% from 5 K to 400 K. However, data below 10 K demonstrated divergent results in the heat capacity for the samples, as shown an insert to Figure 4.33. One trend gives a local maximum around 1.5 K while the other approaches zero without the maximum. The two trends are from different freeze fracture samples from the commercial *β*-boron.

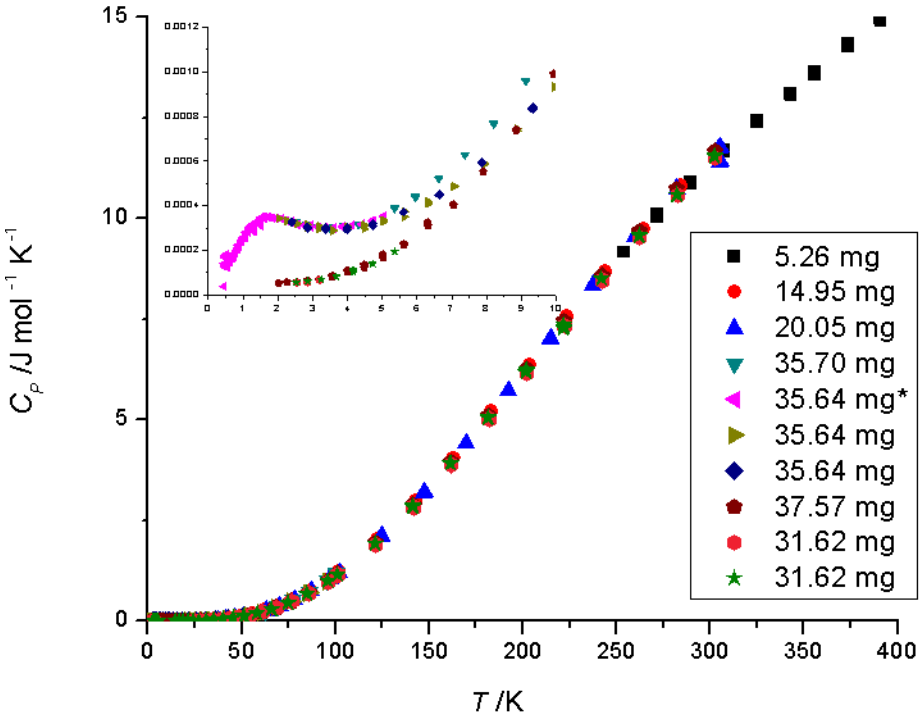

Figure 4.33: β-boron heat capacity from 0 to 400 K. All samples are labelled in the legend with their masses in mg. The 35.64 mg used ^{3}He, all others used ^{4}He as a cryogenic liquid. The samples are listed in the order collected (top run first). Insert shows β-boron heat capacity from 0 to 10 K.*

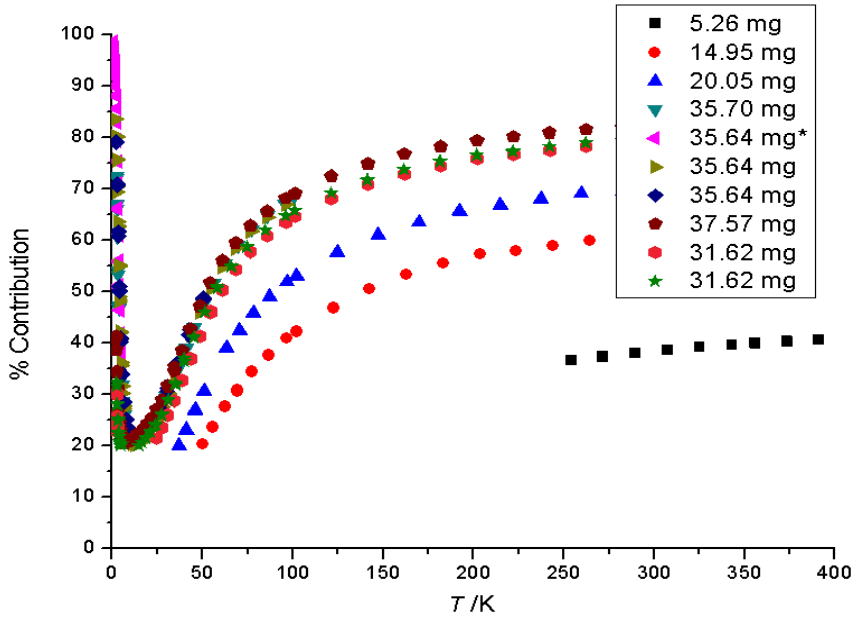

Figure 4.34: β-boron heat capacity contribution to the total heat capacity from 0.35 to 400 K.

In an effort to determine the differences in the two samples, XRD and EDS of each were collected. Figure 4.35 and 4.36 depict the EDS while Figure 4.37 and 4.38 show the XRD results, for samples of masses 35.64 mg and 31.62 mg respectively. The XRD studies reveal inconsistent peak additions compared to previous investigation, which are caused by a change in detectors. Figure 4.37 and 4.38 were collected on area detectors which revealed peaks of preferred orientation. Preferred orientation occurs when the sample has crystal planes aligned in a non-random arrangement. A fully randomized crystal sample produces a ring of x-ray signal in a detector while a fully ordered crystal produces a single dot. Between the two extremes, the area detector displays broken rings. As a traditional detector only observes a section of the fully

disordered rings, crystals with preferred orientation can resolve beyond the measured range. With no readily describable difference between the samples, the thermodynamic analysis of the following section was attempted using both the 35.64 mg and 31.62 mg results as separate comparisons.

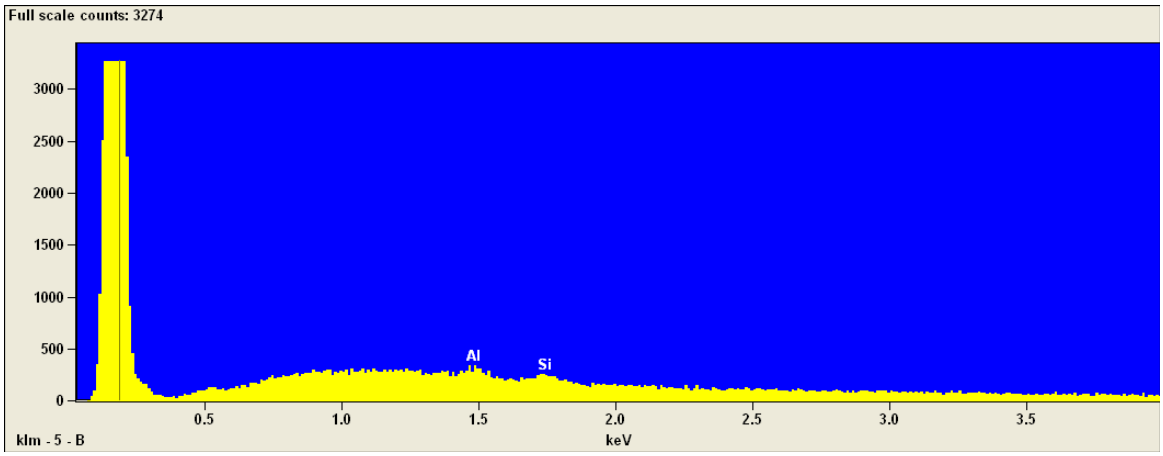

Figure 4.35: Qualitative EDS analysis of β-boron 35 mg sample. Shows minimal impurity.

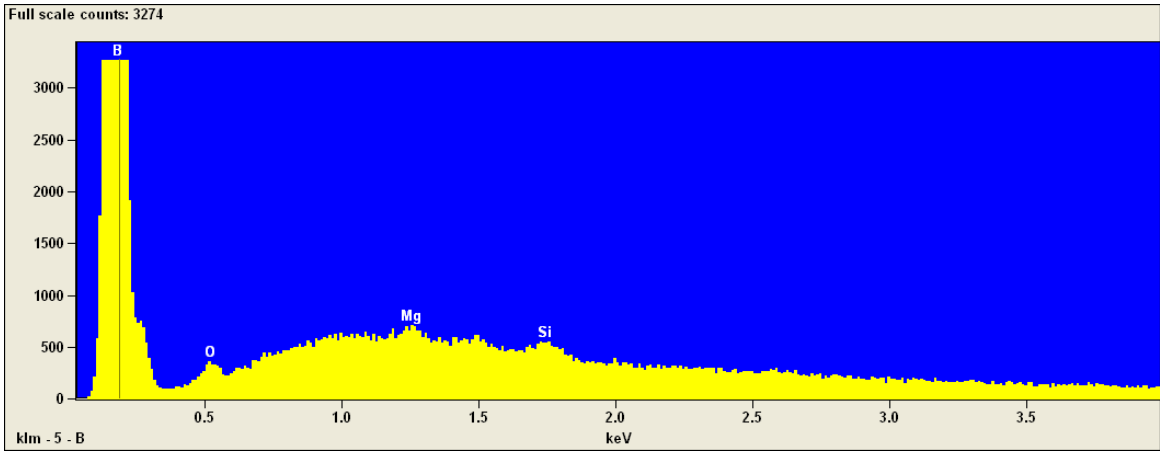

Figure 4.36: Qualitative EDS analysis of the 31 mg β-boron sample. Shows minimal impurity.

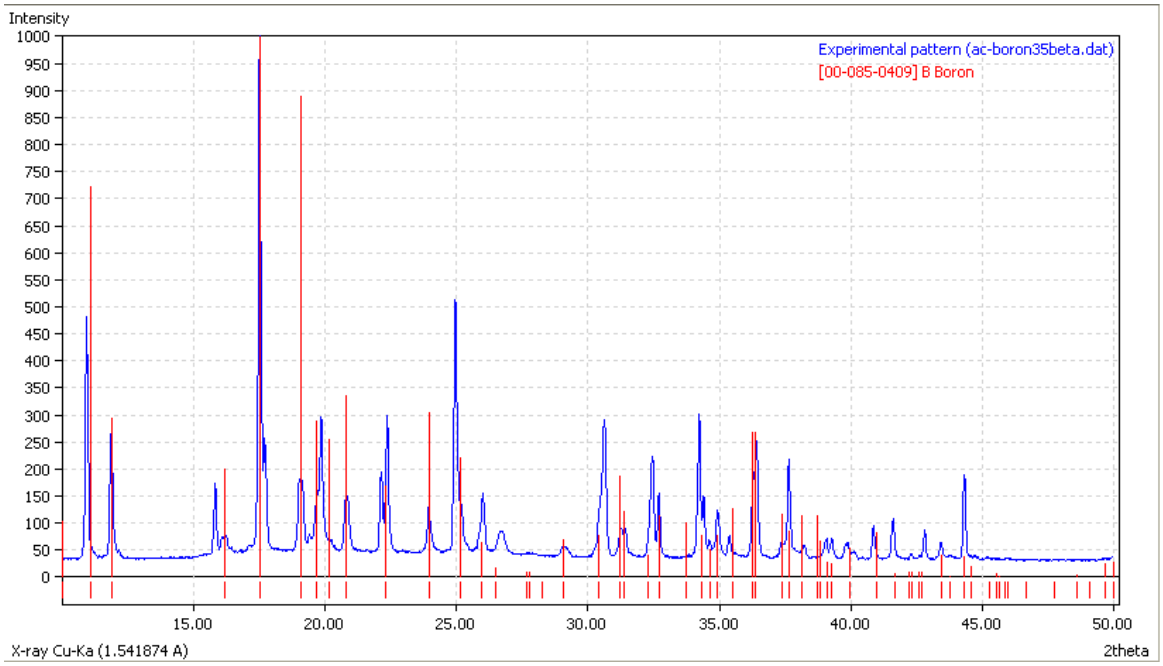

Figure 4.37: Qualitative XRD analysis of the 35 mg β-boron sample.

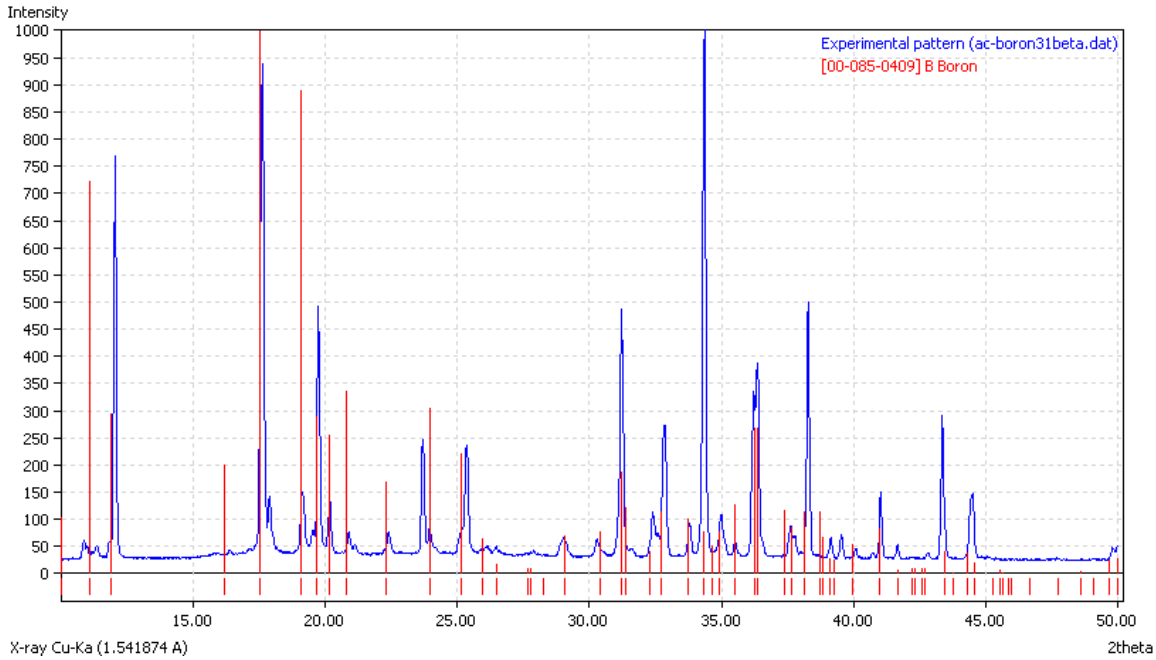

Figure 4.38: Qualitative XRD analysis of the 31 mg β-boron sample.

4.3.1 Literature Comparison

Current measurements of β-boron were compared to the adiabatic calorimetry work of Johnston *et al.*[98] Using 33.774 g of β-boron synthesized via recrystallization on tantalum wire and characterized via XRD, the findings of Johnston *et al.* showed good agreement with the current experiment at temperatures from 50 K to 300 K. At values below 50 K the previous work displays an almost sinusoidal character, showing an unidentified local maxima in the heat capacity situated around 26 K with no correspondence in the present measurements. The Johnston *et al.* data can be seen in Figure 4.39 while 4.40 shows the deviation of the current measurements from the literature. Overall the literature and experimental results are in alignment within better than 5% for $T > 100$ K. Below $T > 100$ K there is a larger difference between the literature and present experimental results.

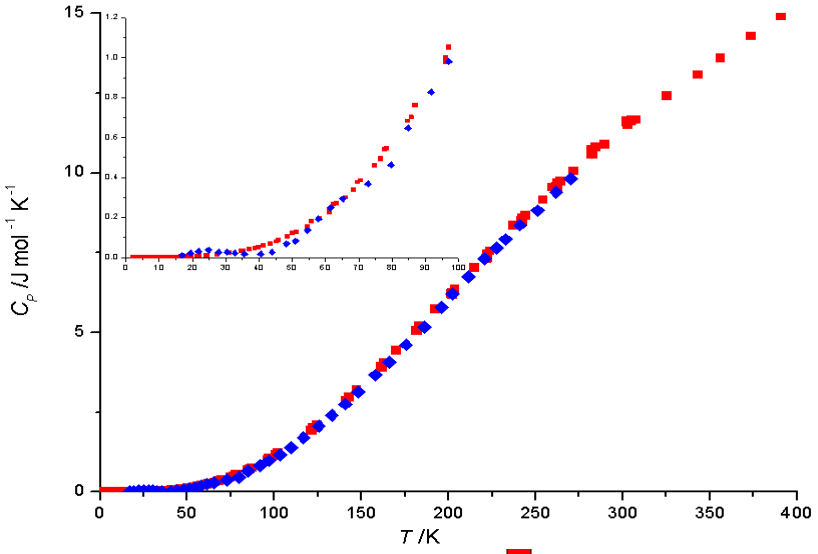

Figure 4.39: Heat capacity of experimental findings, ■ , and data from Johnston et al.[98] ◆ Insert shows range from 0 to 100 K and displays the anomaly of the literature data

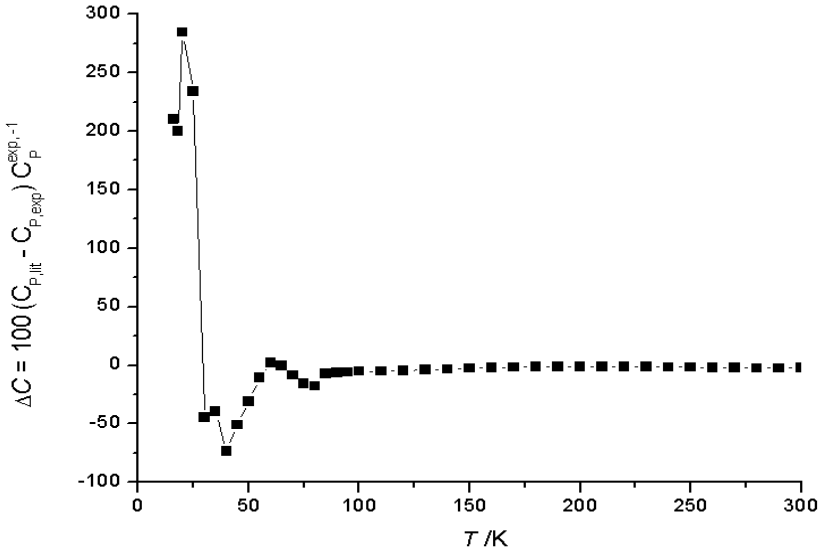

Figure 4.40: Percent deviation between Johnston et al.[98] and experimental measurements. Above T = 100 K agreement is within 5%.

To explain the low temperature anomaly in the Johnston *et al.* data, the experimental design of the previous work was explored in more detail. The Johnston *et al.* calorimeter used a constant-volume helium thermometer, which was not described further.[99] They also employed a temperature scale different from the then U.S Bureau of Standards, which was to be discussed and compared at some other yet unknown date, but to my knowledge was not published.[99] A sampling of work[99,100,101,102,103] was collected in an effort to observe if the sinusoidal nature of the measurements at low temperature were a common feature of other published work from that lab. Studies of boric acid,[99] titanium,[100] dilithium oxide,[101] decaborane,[102] and boric oxide,[103] revealed heat capacity shoulders[99,102,103] at lower temperatures, and a periodic drift around the smoothing line similar to the β-boron work.

Contemporaries of the time also questioned the low-temperature results of Johnston *et al.*[98]. Bogdanov *et al.*[104] inferred that an impurity of the Johnston sample caused the shallow maximum. Only the Bogdanov *et al.* smoothed results were reported and were found to be in poor agreement with current results. The NIST-JANAF tables compiled by Chase[105] consider both findings near the detection limit of the calorimeter as a likely source for the conflicting results. Evans *et al.*[106] of the National Standards Bureau, now NIST, found the work of Johnston *et al.*[98] to be sufficient quality for inclusion as a standard, but cautioned that the low temperature results might be anomalous.

One possible explanation for the previously reported maximum in the C_P vs. T data is the transition of boron into a superconducting state. Such a transition is within the realm of possibility as many materials become superconducting at extremely low temperature. A literature survey of recent work in the field of boron superconductivity reveals a β-boron superconducting transition at 6 K and 175 GPa.[107,108] However, it is known[15] that boron can be in the γ form at such high pressures. Furthermore, the work by Johnston *et al.* was completed at atmospheric pressure so the heat capacity anomaly is unlikely to be related to a superconducting state.

The drop calorimetry data from McDonald and Stull[109] extended the range of C_P determination for 2.539 g of β-boron from room temperature to 1700 K, while Stount, Mar and Boo[110] measured C_P of an unknown quantity of β-boron from 1700 K to 2200 K. Drop calorimetry relies on measuring the change in temperature of a bath after a heated sample is added. Prior to dropping into the monitored bath, the sample itself is contained within a sealed chamber held at some elevated temperature with a connecting passage.[110]

All literature values displayed good agreement with each other and the measurements along overlapping regions as can be seen in Figure 4.41 and 4.40.

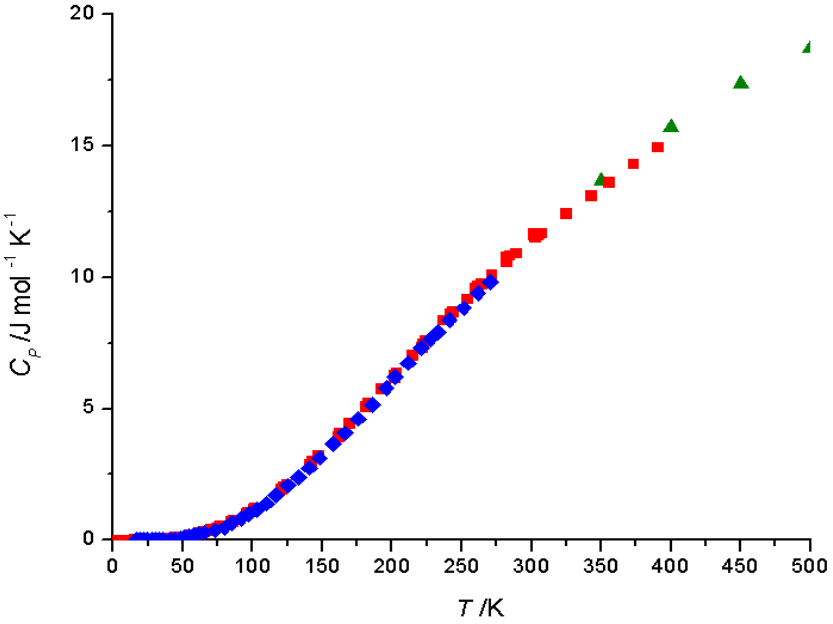

Figure 4.41: Composite heat capacity of β-boron from 0 to 500 K. Current measurements ■ along with literature results from Johnston et al.[98] ◆ and MacDonald and Stull[109] ▲ .

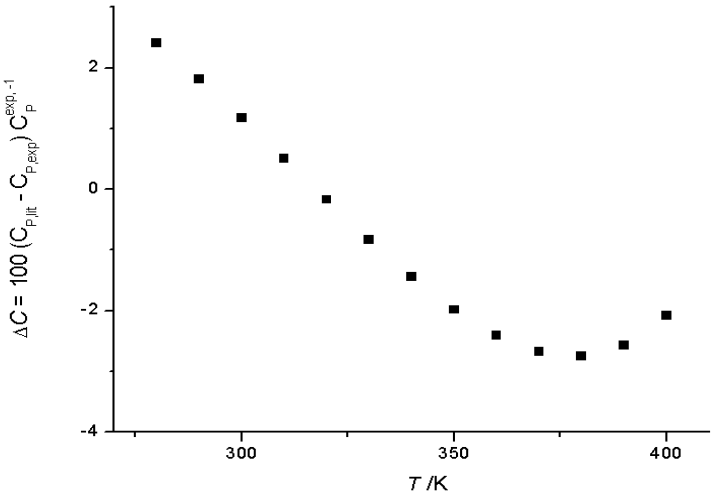

Figure 4.42: Percent deviation of heat capacity for β-boron between McDonald and Stull[109] compared with present experimental measurements from 300 to 400 K.

4.4 *α to β* Phase Transition

The *α*-boron and *β*-boron heat capacity data can be used to calculate the thermodynamics of phase transition as per the theory presented in section 2.1.5. As stated earlier, to accomplish this calculation requires thermodynamic information on a spontaneous transition from *α*-boron and *β*-boron. The only published data appeared to be from the studies of Machaladze[17] who determined the enthalpy of phase transition via differential scanning calorimetry to be -1.05 kcal/mol (-4.39 kJ/mol) at T = 1985 K. The heat capacity of *α*-boron needs to be extrapolated to the transition temperature to carry out the full analysis, since current reliable experimental data are only available to 400 K.

4.4.1 Extrapolation of *α*-boron Heat Capacity

The extrapolation of heat capacity to 2000 K was achieved by using the present experimental *β*-boron heat capacity data to make some assumptions about heat capacity measurements above 400 K. As explained in section 4.3.1 there was good agreement between literature and current *β*-boron measurements from 50 to 400 K, and literature data up to 2200 K.[109,110] The *β*-boron C_P data consisted of the literature values in the higher temperature range, from 400 K to 2200 K, and the current measurements from 0 K to 400 K. To extrapolate *α*-boron to 2200 K, it was assumed that *α* and *β* phases of boron possess the same relative shape for both heat capacity curves. This assumption was based on two concepts; first, that *α*-boron underwent no transitions until the phase change to *β*-boron at 1985 K and second, that pure elemental systems should have little variation in

the overall trend of C_P. The result of these assumptions was that β-boron heat capacity curve could be mapped from experimental data and applied to α-boron with the inclusion of a scaling factor. A function for the α-boron curve was assembled stepwise using a geometric estimation of the integral resulting in the equation of a line

$$y_{2\alpha}=\left(\left(\frac{y_{2\beta}-y_{1\beta}}{x_{2\beta}-x_{1\beta}}\right)(x_{2\alpha}-x_{1\alpha})+y_{1\alpha}\right)0.9884 \quad , \tag{4.4}$$

where the y and x terms represent the sequential coordinates of given heat capacity and temperature respectively for α-boron or β-boron and the constant is an empirical scaling factor, 0.9884. Equation (4.4) could be used to extrapolate the α-boron heat capacity by finding the change between any two points in β-boron (x_1,y_1 to x_2,y_2) and applying such to α-boron. The determination of the scaling factor was based on the intrinsic differences in the heat capacity through the measured range and crucial theoretical considerations outlined below.

The Dulong-Petit law of heat capacity explains the ability of a solid to store heat via the movement of atoms along the x, y and z axes.[72] The energy of the system is thus stored along the connecting bonds as vibrations resulting in

$$U_{max}=3RT \tag{4.5}$$

for molar quantities, which can be combined with equation (2.2) to give

$$C_{V,max}=3R \tag{4.6}$$

where R is the ideal gas constant. The result of this is an upper limit on heat capacity at constant volume in atomic solids of approximately 25 J mol $^{-1}$ K $^{-1}$. In an effort to check the first approximation the literature values of heat capacity at constant pressure were manipulated mathematically to the constant volume form to compare against 3R. The calculation required the isothermal compressibility (β_T) and volume coefficient of thermal expansion (α) employed in the form[72]

$$C_V = C_P - \frac{\alpha^2 VT}{\beta_T} \tag{4.7}$$

with V and T being the volume and temperature respectively. The work by Lundstrom *et al.*[111] provided an average volume expansion coefficient of 1.9 × 10^{-5} K^{-1} while Ma *et al.*[112] determined the isothermal compressibility of 30.7 GPa. During the course of converting β-boron C_P to C_V it became apparent that the derived C_V exceeded the usual 3R limit, meaning that β-boron literature exceeded general theory casting doubt on the results.

The calculated theoretical disagreements introduced by this result were addressed via consideration of the β-boron system with the intent of locating other sources of heat capacity. The work of Callmer[44] and Slack *et al.*[45] mention partially occupied sites in the crystal structure of β-boron. With increase in temperature it is possible these POS might gain sufficient thermal energy to become mobile. Another possibility, Werheit[113] and Kuck *et al.*[28] explained that at temperatures above 600 K, β-boron electrons can be thermally excited into the conduction band. The ability of electrons to move through the material in a manner similar to a metal results in an increased ability to store energy which raises the Dulong-Petit limit. No transition from semiconducting to conducting is observed and

investigation into POS thermal excitation is not available, however these possibilities offer explanations for the unusual β-boron heat capacity results. Since α-boron displays no unexpected features there is no reason to expect the theoretical 3R limit will not apply. This assumption is shared by the work of Naumov *et al.*[97] which also binds their extrapolation for α-boron to the 3R limit. (The findings of the Naumov *et al.* extrapolation will be discussed more below.) To ensure the upper C_P bound, the scaling factor in equation (4.4) was selected resulting in a final extrapolation as can be seen in Figure 4.43.

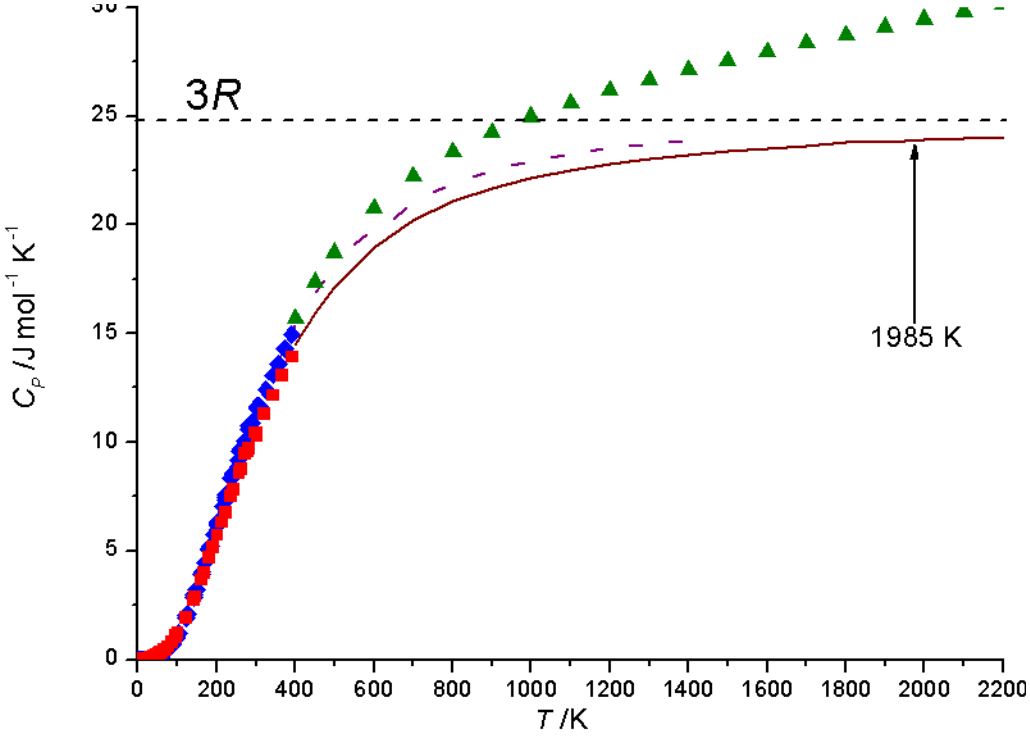

Figure 4.43: Extrapolation of α-boron heat capacity using equation (4.4) *from 400 K to 2200 K. The 3R limit is depicted as the black dashed line. The* ■ *are α-boron, and* ◆ *β-boron measurements respectively from the present work. The* ▲ *are β-boron literature values.*[109,110] *The current extrapolation is depicted as the solid line and the dashed line is the extrapolation by Naumov et al.*[97]

4.4.2 ΔH_t, ΔS_t and ΔG_t of α to β phase transition

The values ΔG_t, ΔH_t, ΔS_t of α to β phase transition were calculated as functions of temperature as per equations (2.9), (2.10) and (2.11). As outlined in section 2.1.5, this required the thermodynamic cycle and equation (2.12) and the C_P data from α and β-boron. The previously mentioned variations in the β-boron low-temperature C_P results were each employed independently throughout the (2.12) calculations providing no significant difference between the final results. ($\Delta H_t\ (T=0)$ = -10,010.29 J mol^{-1} for 35.64 mg and -10,004.75 J mol^{-1} for 31.62 mg.) The final result of the transitional stability calculation can be seen in Figure 4.44 across the range 0 K to 2200 K. The transition of α-boron to β-boron was found to be thermodynamically favourable along 0 K to 2200 K reaching -15 kJ mol^{-1} ± 1 kJ mol^{-1} at T = 1985 K.

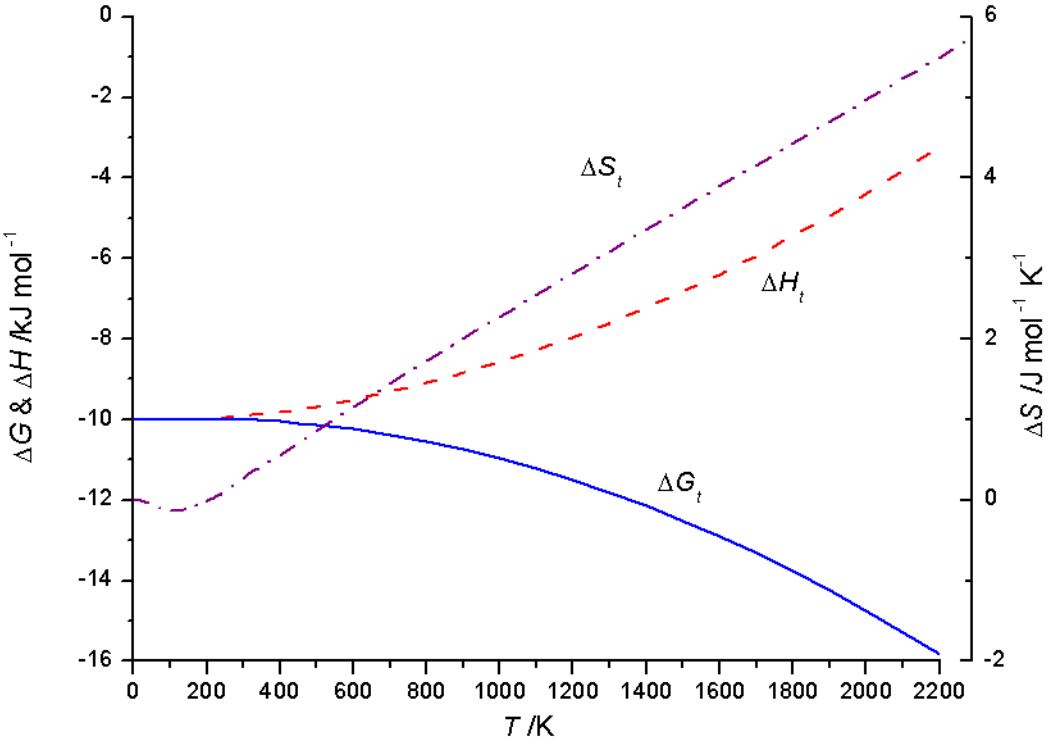

Figure 4.44: ΔG_t, ΔH_t, and ΔS_t values of the α to β phase transition across the temperature range 0 to 2200 K.

Errors were propagated from measurements with assumptions of 10% for the $\Delta H_t(T=1985\ \text{K})$, for the DTA experiment,[17] as the major source of error.

This finding of β-boron stability followed logical agreement with observed trends during the course of experimentation such as: 1) the often documented ability to convert α-boron to β-boron, but no mention of the reverse, 2) the difficulty synthesizing α-boron recorded in previous literature and current work, 3) the discovery of lower temperature synthesis of β-boron mentioned in 4.1.2.

The temperature range from 0 to 400 K demonstrated the most variability in the results, as can be seen in Figure 4.45. There are three distinguishing features: 1) the local minimum in the enthalpy and entropy change at 100 K, 2) the Gibbs energy change maximum at 200 K, 3) the sign change in entropy change values.

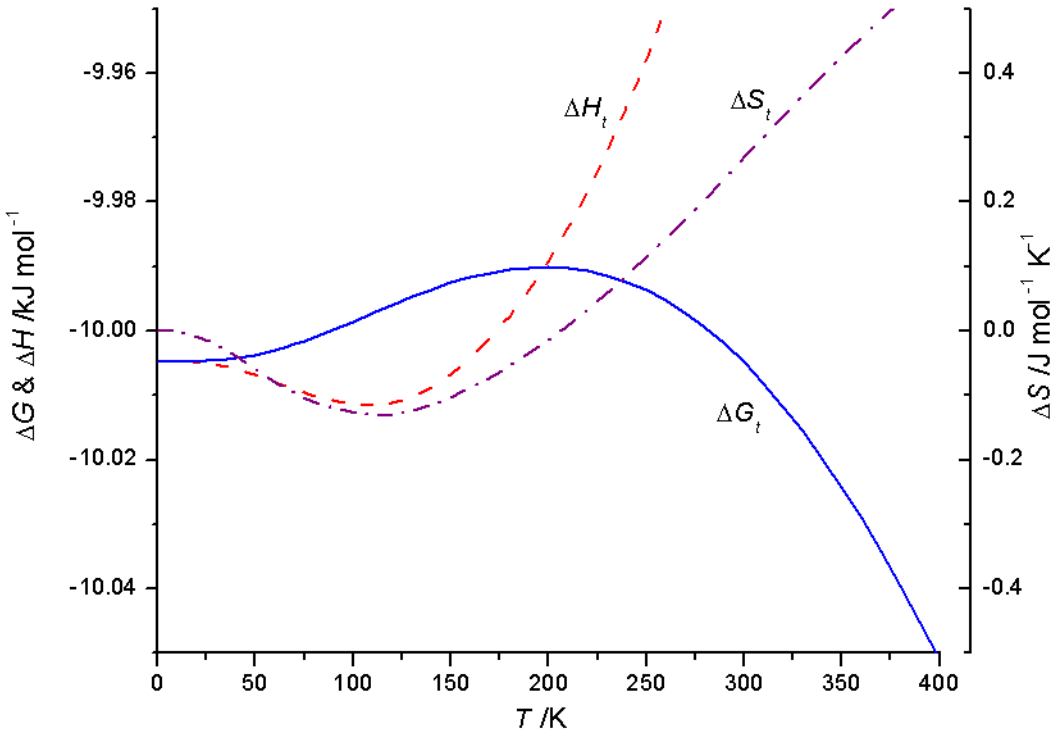

Figure 4.45: ΔG_t, ΔH_t, and ΔS_t values of the α to β-boron phase transition across the temperature range 0 to 400 K.

The local minima correspond to a crossover in the heat capacity curves. For $T <$ 100 K, α-boron had an overall higher heat capacity while β-boron possessed a greater ability to store heat above 100 K as can be seen in Figure 4.46 and 4.47, respectively.

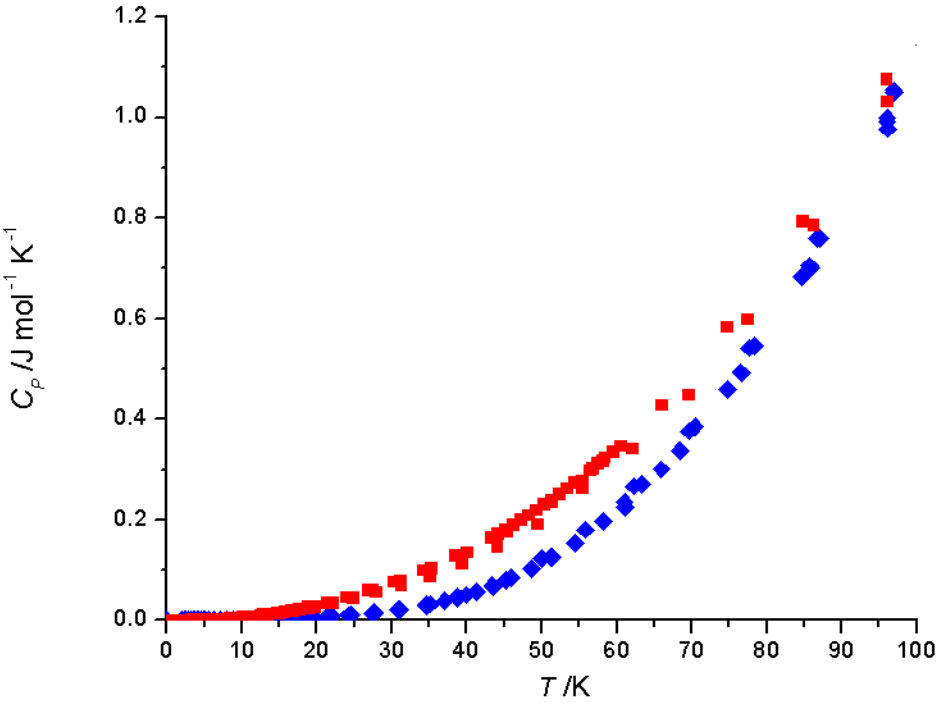

Figure 4.46: Experimental heat capacity comparison from 0 K to 100 K. α-boron ■ while β-boron ◆ . α-boron has a higher heat capacity along this temperature range.

A possible source of the crossover in heat capacity could be the activation of β-boron electronic effects mentioned in section 4.4.1 allowing the heat capacity of β-boron to exceed α-boron.[113] Another possibility is that the greater complexity of the β-boron unit cell, especially the POS, may allow a larger number of energy storage modes than the simpler α-boron.

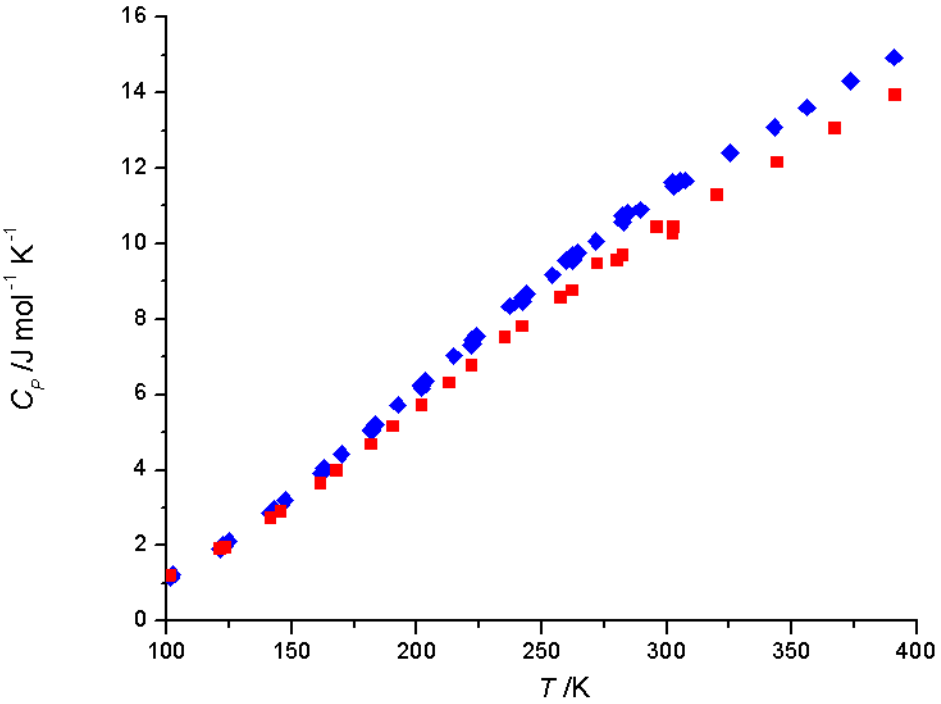

Figure 4.47: Experimental heat capacity comparison from 100 K to 400 K. α-boron ■ and β-boron ◆. β-boron has a higher heat capacity along this temperature range.

The entropy of transition dips below zero across the range 0 to 100 K where *α*-boron possesses a higher heat capacity. The trend in entropy values indicated the transition from *α*-boron to *β*-boron would result in a net loss of system disorder. A possible source of this is the loss of thermal disorder as the stored thermal energy is lost during the transitions between allotropes.

The local maximum in the Gibbs energy at 200 K corresponds to the sign change of the entropy curve. Before 100 K the entropy of transition was less than zero due to the difference in heat capacity. Between 100 K and 200 K the values climbed out of the well created by the local minimum resulting in an inflection point of 200 K for the Gibbs

curve. Throughout the range of the local maximum, the Gibbs energy remains negative due to the magnitude of the enthalpy of transition.

Although the thermodynamic results indicate a spontaneous transition from α-boron to β-boron over the entire temperature range studied, the ability to synthesize α-boron indicates the transition is kinetically restricted. Thus analogy can be drawn between the phase transition of α-boron to β-boron and diamond to graphite: each precursor is meta-stable but kinetically restricted from transitioning.

4.4.3 Literature Comparison

To analyze the current thermodynamic findings three comparisons were made to literature: first the extrapolation by Naumov *et al.*[97] was combined with current experimental data for α-boron to test the previously described extrapolation. The results that can be seen in Figure 4.48 across the range 0 K to 2200 K. Secondly, the literature findings of Johnston *et al.*,[98] McDonald *et al.*,[109] and Stout *et al.*[110] for β-boron were assembled along with the full range of α-boron heat capacity from Naumov *et al.*[97] which is displayed in Figure 4.49. Finally the effect β-boron heat capacity exceeding $3R$ was considered.

The ΔG_t calculated from Naumov *et al.*[97] and combined literature[97,98,109,110] corroborates the current experimental findings displaying a negative ΔG_t across the temperature. The transition values (T = 1985 K) of -13 kJ mol^{-1} ± 1 kJ mol^{-1} and -12 kJ mol^{-1} ± 1 kJ mol^{-1} for Naumov *et al.* and combined literature respectively are nearly within error of the current results. (-15 kJ mol^{-1} ± 1 kJ mol^{-1})

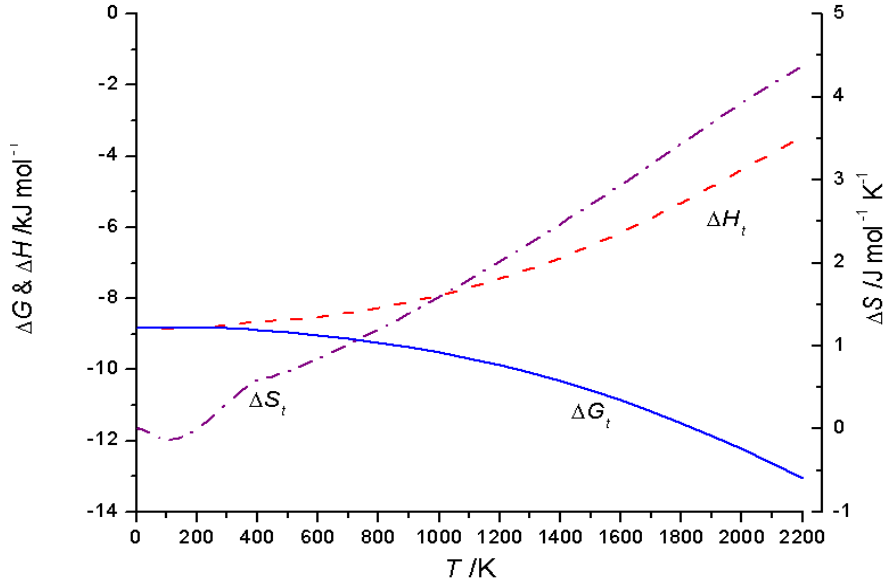

Figure 4.48: Naumov *et al.*[97] *extrapolation for α-boron derived ΔG_t, ΔH_t, and ΔS_t values of the α to β phase transition across the temperature range 0 to 2200 K. Below 400 K current experimental results were employed.*

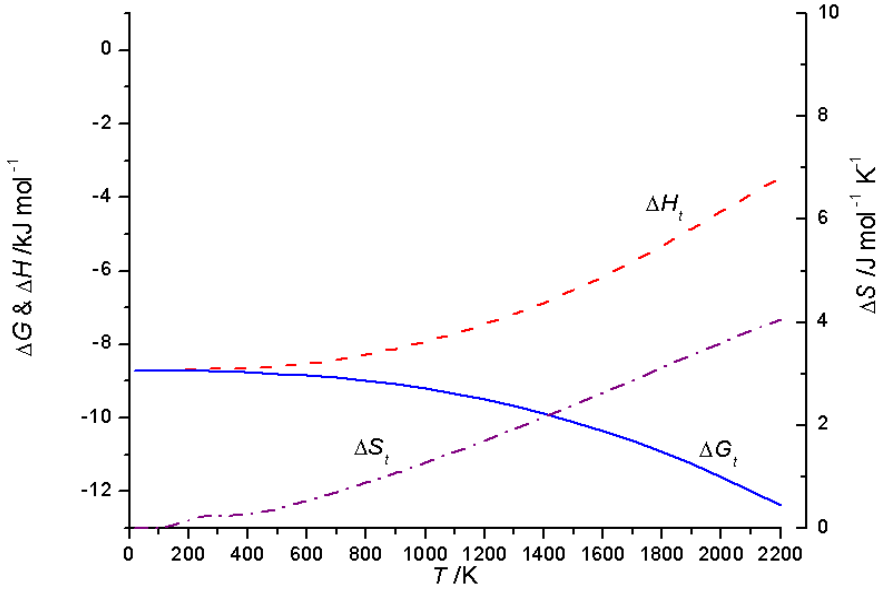

Figure 4.49: Literature only based heat capacity[97,98,109,110] *derived ΔG_t, ΔH_t, and ΔS_t values of the α to β phase transition across the temperature range 0 to 2200 K.*

A closer study of the temperature range 0 to 400 K in reveals differences in the entropy and enthalpy curves of the combined literature study. Due to the previously mentioned anomaly of the low temperature *β*-boron heat capacity there is no consistent trend in the relative magnitude of each allotrope. This inconsistency causes the literature entropy and enthalpy values to have less absolute magnitude and display no local minimum at 100 K. As the Naumov *et al.* comparison used current measurements at $T <$ 400 K the findings mirror that of current experimental work.

The heat capacity measurements of McDonald *et al.*,[109] and Stout *et al.*[110] exceeded the 3*R* limit. Possible explanations were considered in section 4.3.1 however to check the findings of the thermodynamic stability the *β*-boron heat capacity from 400 K to 2200 K was reduced via the scaling factor 0.84 to meet the 3*R* limit seen in Figure 4.50. The resulting heat capacity curves resulted in no change to the overall trend, shown in Figure 4.51, save a ΔG_t (T=1985K) of -8 kJ mol^{-1} ± 1 kJ mol^{-1}. Thus the findings still hold valid should the literature values of McDonald *et al.*,[109] and Stout *et al.*[110] be in error.

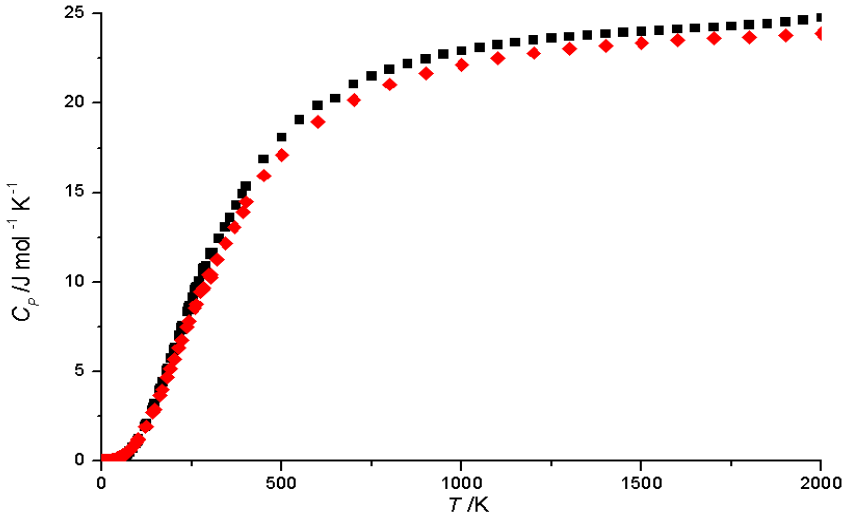

Figure 4.50: α-boron ♦ and β-boron ■ heat capacity from 0 K to 2000 K. β-boron values rescaled to meet the 3R limit and used in Figure 4.51 *to reexamine* $\Delta G_t(T)$.

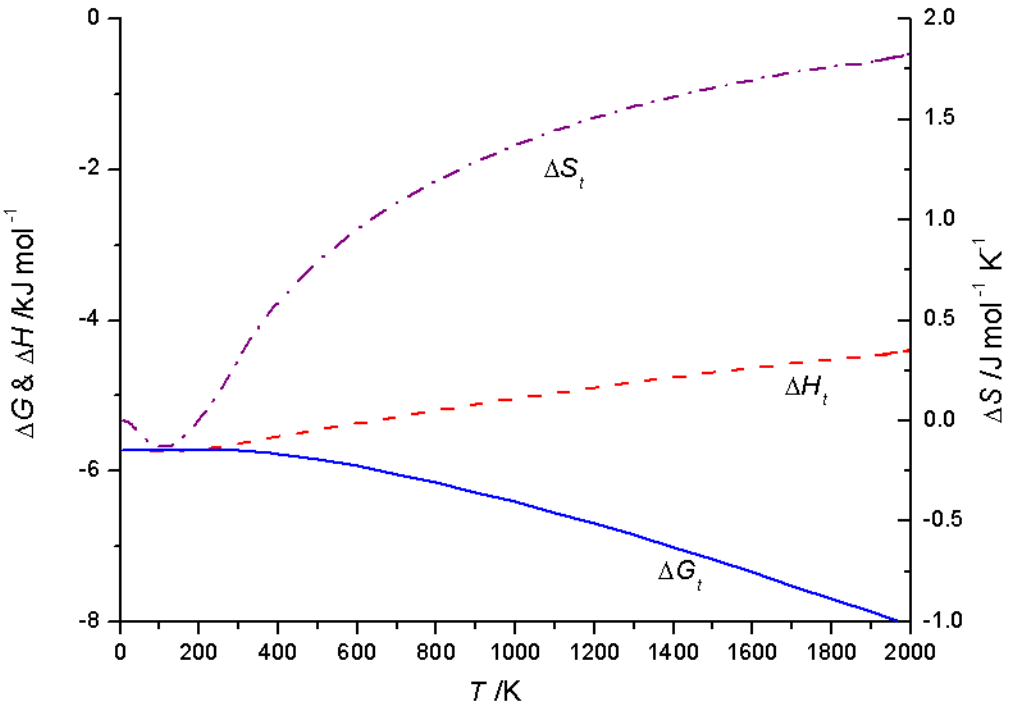

Figure 4.51: Depressed β -boron heat capacity derived ΔG_t, ΔH_t, and ΔS_t values of the α to β phase transition across the temperature range 0 to 2000 K.

4.4.4 Disorder and Transitional Stability

All calculations so far have been carried out assuming , that the various samples exist as perfect crystals at T = 0 K and thus S = 0 J mol^{-1} K^{-1} applies to this system. However as has been mentioned previously, a theoretically perfect β-boron crystal has 105 atoms in the unit cell whereas in reality there are 106.66. The remaining 1.66 atoms of boron occupy the partially occupied sites that give β-boron so many of the novel properties discussed. The work by Callmer[44] and Slack *et al.*[45] found a total of six discrete

POS which can be approximated to three sites per boron atom. To transform this potential for disorder into the entropy of the crystal at $T = 0$ K requires statistical thermodynamics in the form of

$$S = R\ln(\Omega) \tag{4.8}$$

where R is the ideal gas constant, and Ω is the number of micro-states of the system contributing to disorder.[48] Figure 4.52 depicts the thermodynamic functions ΔG_t, ΔH_t, ΔS_t when $\Omega = 3$ per unit cell of 106.66 atoms resulting and thus $S_t\ (T=0) = 0.1$ J mol^{-1} K^{-1} through equation (4.8).

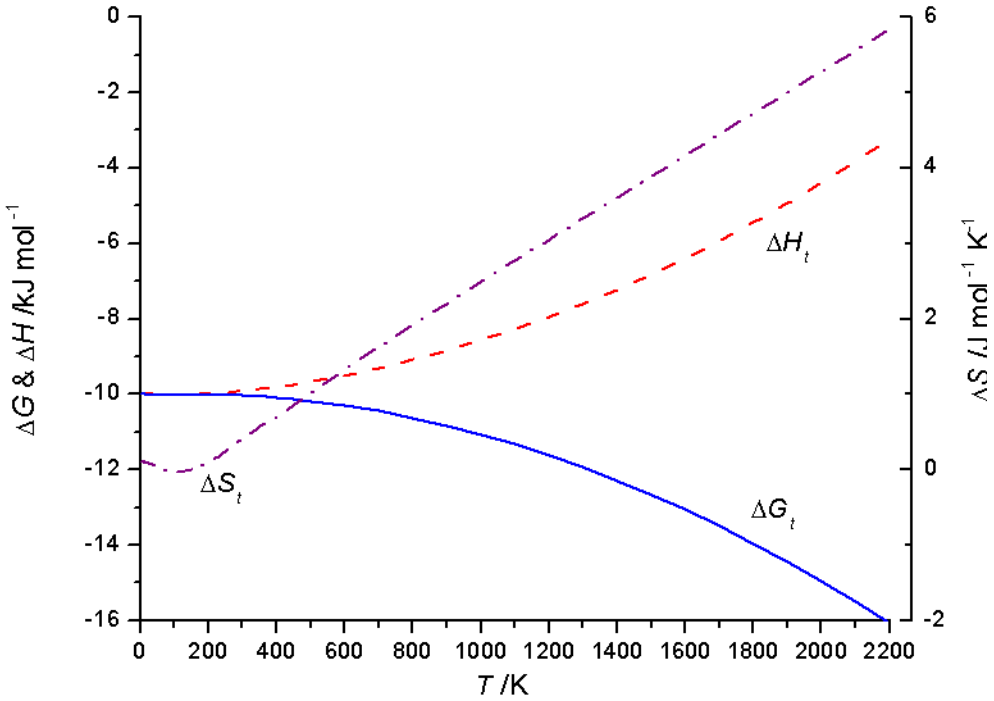

Figure 4.52: A repetition of the calculations assuming β-boron POS distorts the perfect crystal resulting in a $S_t\ (T=0) = 0.1$ J mol^{-1} K^{-1} from 0 K to 2200 K.

The resulting values display the same negative slope as the perfectly ordered case reaching -15 kJ mol^{-1} ± 1 kJ mol^{-1} at 1985 K. As the perfect order and the disorder cases both display the same trends, it is a valid approximation to consider the actual system to be somewhere between the two bounds which resides within the margin of error.

Chapter 5 Conclusions

α-boron was synthesized through the novel approach of chemical vapour deposition. Boron trichloride was reduced by hydrogen to boron vapour and deposited onto quartz glass at the ideal temperature of 850 °C with a flow rate of 1 mL/min of vapour. The heat capacity at constant pressure was measured for synthesized α-boron and commercial β-boron across the temperature range of 0.2 K to 400 K using relaxation calorimetry via the Physical Property Measurement System. It was found that α-boron possesses a higher heat capacity than β-boron in the range 0.2 K to 100 K while the reverse is true for 100 to 400 K. Through thermodynamic analysis it was found that the transition from α-boron to β-boron was thermodynamically favourable from 0 K to 1985 K with a value of $\Delta G_t(T = 300\ K) = -10\ kJ\ mol^{-1} \pm 1\ kJ\ mol^{-1}$ and $\Delta G_t(T = 1985\ K) = -15\ kJ\ mol^{-1} \pm 1\ kJ\ mol^{-1}$.

Exploration of the precise mechanism as well as optimization of α-boron synthesis via CVD offers intriguing possibilities for the future. The heat capacity anomaly observed in β-boron below 10 K was not fully determined although possibilities such as superconducting transitions and sample error were considered. The thermodynamic study had a foundation upon the work of Machaladze[17] for the enthalpy of the spontaneous allotrope transition and extrapolation of the heat capacity beyond the currently measured range. Extending the range of measurements and checking the enthalpy of transition would provide valuable insight.

References

1 Oganov, A.R.; and Solozhenko, V.L.; *J. of Superhard Materials*; **2009**; *31*; (5); 285.

2 Gurin, V. and Korsukova, M.; *J. Solid State Chem.;* **2004;** *177.*

3 Hillebrecht, H.; and Albert, B.; *Angew. Chem. Int. Ed.*; **2009**; *48*; 8640.

4 Thênard, J.L.; and Gay-Lussac, L.J.*; Mémoires de Physique et de Chimie, de la Société d'Arcueil;* **1809***; 2*, 339.

5 Davy, H.; *Phil. Trans. R. Soc. Lond.;* **1808;** *98;* 333.

6 Moissan, H.; *Ann. Chim. Phys.;* **1895;** *6;* 296.

7 Weintraub, E; *Trans. Am. Electrochem. Soc.*; **1909**; *16*; 165.

8 Sainte-Claire Deville, H. and Wöhler, F.; *Ann. Physik;* **1857;** *176;* (4); 635.

9 Wöhler, F. and Sainte-Claire Deville, H.; *Ann. Chim. Phys.;* **1858;** *52;* (3); 63.

10 Laubengayer, A.W., Hurd, D.T., Newkirk, A.E., and Hoard, J.L.; *J. Am. Chem. Soc.;* **1943;** *65;* 1924.

11 Amberger, E. and Ploog, K.; *J. Less-Common Metals;* **1971;** *23;* 21.

12 Sands, D.E. and Hoard, J.L.; *J. Am. Chem. Soc.;* **1957;** *79;* 5582.

13 McCarty, L.V., Kasper, J.S., Horn, F.H., Decker, B.F., and Newkirk, A.F.; *J. Am. Chem. Soc.;* **1958;** *80;* 2592.

14 Talley, C.P.; *Acta Cryst.;* **1960;** *13;* 271.

15 Oganov, A.; Chen, J.; Gatti, C.; Ma, Y.; Ma1, Y.; Glass, C.; Liu, Z.; Yu, T.; Kurakevych, O. and Solozhenko; V.; *Nature;* **2009**; *457*; 863.

16 Runow, P.; *Journal of Materials Science*; **1972**; *7*; 499.

17 Machaladze, T.; *Proceedings of the Academy of Sciences of Georgia, Chemical Series*; **2005**; *31*; (3-4); 331.

18 Ogitsu, T.; Gygi, F.; Reed, J.; Motome, Y.; Swegler, E. and Galli, G.; *J. Am. Chem. Soc.;* **2009;** *131;* 1903-1909.

19 Shirai, K.; Masago, A. and Katayama-Yoshida, H.; *Phys. Status Solidi B*; **2007;** *244;* 303.

20 van Setten, M.; Uijttewaal, M.; de Wijs, G.; and de Groot, R.; *J. Am. Chem. Soc.*, **2007**, *129*, 2458.

21 Chase, M. W. Jr.; *J. Phys. Chem. Ref.* Data 9; **1998;** *2*; 457.

22 Widom, M. and Mihalkovic, M.; Phys. Rev.; **2008;** *B77;* 064113.

23 Jemmis, E. and Prasad, D.; *Current Science;* **2008;** *95;* (9); 1277-1283.

24 Masago, A.; Shirai, K. and Katayama-Yoshida H.; *Physical Review B;* **2006;** *73*, 104102.

25 McCarty, L.; Kasper, J.; Horn, H.; Decker, B., and Newkirk, A.; *J. Amer. Chem. Soc.*; **1958;** *80;* (10), 2392.

26 Tsagareishvili, G.; and Tavadze, F.; *Prog. Crystal Growth and Charact.*; **1988**; *16*; 341.

27 Sulfenger, D. B.; Kennard, C. H. L.; *Sci. Am.;* **1966;** *215;* (96); 107.

28 *Landolt-Bornstein*, Non-Tetrahedrally Bonded Binary Compounds II: Supplement to Vol. III/17g (Print Version), Revised and Updated Edition of Vol. III/17g (CD-ROM) (Numerical Data and Functional Relationships in Science and Technology-New Series) by S. Kuck, H. Werheit, O. Madelung, (2000).

29 Cohen, M.; and Zettl, A.; *Physics Today;* **2010;** November; 34.

30 Afanas'ev, V.; and Karpinos, D.; Institute of Materials Science, Academy of Sciences of the UkrSSR.; **1966**; *7;* 43; 49.

31 Guo S.Q.; *Journal of the European Ceramic Society;* **2009***; 29;* 995.

32 Bolgar, A.S.; and Blinder, A.V.; *Poroshkovaya Metallurgiya;* **1989;** *2;* (314); 60.

33 Fahrenholtz, W. and Hilmas, G.; *Journal of the American Ceramic Society;* **2007**; *90;* 5.

34 Munro, A; *J. Res. Natl. Inst. Stand. Technol.*; **2000**; *105;* 709.

35 Nagamatsu, J.; Nakagawa, N.; Muranaka, T.; Zenitani, Y.; Akimitsu, J.; *Nature*; **2001;** *410;* 63.

36 Braccini, V.; Nardelli, D.; Penco, R. and Grasso, G.; *Physica C: Superconductivity;* **2007**; *456;* 1–2; 209.

37 Katada, K.; *Jpn . J. Appl. Phys.*; **1966;** *5;* 582.

38 Ott., H. M. And Lipsitt H. A.; *Phys. Stat. Sol.*; **1966**; *13*; 439.

39 Lindquist, P. F.; Hammond, M. L.; and Bragg, R.H.; *Phys. Stat. Sol.*; **1966**; *17*, K25.

40 Kobayashi, M.; J. of Mat. Sci.; **1988**; *23*; 4392.

41 Will, G. and Kiefer, G.; *Anorg. Allg. Chem.*; **2001**; *627*, 2100-2104.

42 Bullett, D.W.; *J. Phys. C: Solid State Phys.*; **1982**; *15*; 415.

43 Jemmis, E.; and Balakrishnarajan, M.; *J. Am. Chem. Soc.*; **2001**; *123*; 4324.

44 Callmer, B.; *Acta Cryst. B;* **1977;** *33;* 1951-1954.

45 Slack, G.A.; Hejna, C.I.; Garbauskas, M.F.; and Kasper, J.S.; *J. of Solid State Chem*; **1988**; *76*; 52.

46 Hoard, J.L.; Hughes, R.E.; and Sands, D.E.; *J. Amer. Chem. Soc.*; **1958**; *80*; 4507.

47 Vlasse, M.; Naslin, R.; Kasper, J.S.; and Ploog, K.; *Journal of Solid State Chemistry*; **1979**; *28*; 289.

48 *Chemical Thermodynamics Principles and Applications;* Ott, J., and Boerio-Goates;

Academic Press: San Diego, California, (2000).

49 Wagner, R. S.; Ellis, W. C.; *Trans. Metallurgical Society of AIME.* **1965**, *233*, 1053-1064.

50 Sitarik, J.P., Masters Thesis; *VLS Growth of Single Crystal Boron*; Electrical Engineering Department; Ohio State University, 1965.

51 *Preparation and Chemistry of Elemental Boron;* Newkirk, A. E.; Advances in Chemistry Series, # 32; American Chemical Society: Washington, DC, (1961).

52 Tavadze, F.N.; and Tsagareishvili, G.V.; *Prog. Crystal Growth and Character.*; **1988**; *16*; 41.

53 *Principles of Chemical Vapor Deposition;* Dobkin, D., and Zuraw, M.; Kluwer Academic Publishers: Dordrecht, Netherlands, (2003).

54 *Physical Property Measurement System: Hardware and Options Manual*, Quantum Design; (2003).

55 Apiezon® technical data sheet, N grease

56 Apiezon® technical data sheet, H grease

57 Kennedy, C.A.; and White, M.A.; *Solid State Communications;* **2005***; 134*; 271.

58 Kennedy, C.A.; Stancescu, M.; Marriott, R.A; and White, M.A.; Cryogenics*;* **2007***; 47*; 107.

59 Thompson, J.C.; and McDonald, J.W.; *Physical Review*; **1963**; *132*; (1); 82.

60 Slack,G.A.; *Physical Review*; **1965**; *139*; (2A); A507.

61 Bachmann, R.; DiSalvo Jr, F. J.; Geballe, T.H.; Greene, R. L.; Howard, R. E.; King, C. N.; Kirsch, H. C.; Lee, K. N.; Schwall, R. E.; Thomas, H. U.; and Zubeck, R. B.; *Rev Sci Instrum;* **1972,** *43,* 205.

62 Hwang, J.S.;Lin, K. J.; and Tien, C.; *Rev. Sci. Instrum.*, 1997, 68, *(1)*, 94.

63 Lashley, J.; Hundley, M.; Migliori, A.; Sarrao, J.; Pagliuso, P. ; Darling, T.; Jaime, M.; Cooley, J.; Hults, W. ; Morales, L.; Thoma, D.; Smith, J.; Boerio-Goates, J.; Woodfield, B.; Stewart, G.; Fisher, R.; and Phillips, N.; *Cryogenics*; **2003,** *43;* 369–378.

64 *Physical Methods in Supramolecular Chemistry;* White, M.A.; Chapter 4 in Volume 8; Eds. Lehn, J.M.; Atwood, J.L. ; and MacNicol, D.D. Pergamon Press (1996).

65 *Fundamentals of Powder Diffraction and Structural Characterization of Materials*; Pecharsky,V.K.; Zakalij, P.Y.; Springer Science+Business Media, Inc. New York, (2005).

66 Knoll, M.; *Zeitschrift für technische Physik;* **1935,** *16,* 467–475.

67 *Scanning Electron Microscope;* Vladár, A. E.; and Postek, M. T.*;* Handbook of Charged Particle Optics, 2nd; ed; *Orloff, J.; Ed;* CRC: Cleveland, Ohio, (2008).

68 Fitzgerald, R.; Keil, K.; and Heinrich, K.; *Science*; **1968**; *159*; 528.

69 International Chemical Safety Card 0616

70 International Chemical Safety Card 0230

71 Politzer, P.; Lane, P.; Concha, M.C.; Ma, Y.; and Murray, J.; *J. Mol. Model*; **2007**; *13*; 305.

72 *Physical Properties of Materials 2nd Ed*; White, M. A.; CRC Press: Boca Raton, FL, (2012).

73 Sitarik, J.P.; Ellis, W. C.; *Journal of Applied Physics*; **1965,** *37;* (6); 2399-2401.

74 Ahmad I.; and Heffernan W.; *J. Electrochem. Soc.*; **1971,** *118;* (10); 1670-1675.

75 1.3c; 2003 to 2006; Crystal Impact

76 International Centre for Diffraction Data, PC: Powder Diffraction File, 2003.

77 ICSD PCPDF Reference: 00-085-0702, ICSD using POWD-12++ 12, 503 from 1997

78 ICSD PCPDF Reference: 00-089-2777, Calvert, L., National Research Council of Canada, Ottawa, Canada, ICDD Grant-in-Aid, from 1977

79 Danilatos, G. D.; *Adv. Electron. Electron Phys.*, **1988,** *71*, 109–250..

80 Crewe, A. V.; Isaacson, M.; and Johnson, D.; *Rev. Sci. Instrum.*, **1969,** *40*, 241–246.

81 ICSD PCPDF Reference: 00-065-2870, Calculated from NIST using POWD-12++ 3, 605 1935

82 *Gold Boron Binary Phase Diagram;* Okamoto, H.; and Massalski, T. B.; Binary Alloy Phase Diagrams, T.B. Massalski (ed.), Vol. 1, Am. Soc. Met: Ohio, Metals Park, (1986).

83 Wald, F.; and Rosenberg, A.J.; *Trans. Metallurgical Society of AIME.* **1965**, *233*, 796.

84 Brodowsky, H.; and Sagunski, H.; *Ber. Bunsenges. Phys. Chem.,* **1983,** *87*, 803.

85 *α-Boron - Synthesis, Structure and Properties*; *Horn, F.H.;* J.A. Kohn, W.F. Nye, G.K.

Gaul; Eds.; Plenum Press, Inc.; New York, (1960).

86 *Binary Phase Diagram Handbook;* Moffatt, W.G.; General Electric Comp.; New York, Schenectady, (1983).

87 ICSD PCPDF Reference: 00-085-0462, Calculated from ICSD using POWD-12++ 219, 107 1997

88 ICSD PCPDF Reference: 00-085-0462, Calculated from ICSD using POWD-12++ 187, 54 (1997)

89 ICSD PCPDF Reference: 00-086-1563, Calculated from ICSD using POWD-12++ 65, 920 (1997)

90 Agaogullari, D.; Balci, O.; Dunman, I.; and Ovecoglu, M.L.; *Metallurgical and Materials Transactions B*; **2011**; *42B*; 568.

91 ICSD PCPDF Reference: 00-085-0462, Calculated from ICSD using POWD-12++ 35, 550 1979

92 ICSD PCPDF Reference: 00-085-0462, Calculated from ICSD using POWD-12++ 14, 733 1997

93 Bearden, J. A.; *Rev. Mod. Phys.*; **1967**; *39*; (1); 78 .

94 Nishizawa, J.; Aoki, K.; and Akamine T.; *Apply. Phys. Letter.*; **1990**; *56*; (14); 1334.

95 ICSD PCPDF Reference: 00-030-0199, Wang, P., Polytechnic Institute of New York, Brooklyn, New York, USA, ICDD Grant-in-Aid, 1979

96 Tsagareishvili, D. Sh.; Tsagareishvili, G.V.; Omidze, I.S.; Jobava, J. Sh.; Naumov, V.N.; Nogteva, V.V; and Paukov, I.E.; *Journal of Less Common Metals*; **1986;** *117*, (1-2), 143.

97 Naumov, V. N.; Nogteva, V. V.; Paukov, I. E.; Tsagareishvili, G. V.; *Zhurnal Fizichesko Khimii*, **1997**; *71*; (9); 1596.

98 Johnston, H. L.; Hersh, H. N. and Kerr, E. C.; *J. Am. Chem. Soc.;* **1951,** *73;* (3), 1112.

99 Johnston, H.L.; and Kerr, E.C.; *J. Am. Chem. Soc.*; **1950**; *72*; 4733.

100 Kothen, C.W.; and Johnston, H.L.; *J. Am. Chem. Soc.*; **1953**; *75*; 3101.

101 Johnston, H.L.; and Bauer, T.W.; *J. Am. Chem. Soc.*; **1951**; *73*; 1119.

102 Kerr, E.C.; Hallett, N.C.; and Johnston, H.L.; *J. Am. Chem. Soc.*; **1951**; *73*; 1117.

103 Kerr, E.C.; Hersh, H.N.; and Johnston, H.L.; *J. Am. Chem. Soc.*; **1950**; *73*; 4738.

104 Bogdanov, V. I.; *Fizika Tverdogo Tela*; **1970**; *12*; (11); 3333.

105Chase, M. W.; *J. Phys. Chem. Ref. Data.*; **1983**; *9*; 178 (NIST-JANAF Thermochemical Tables)

106 Evans, W.H.; Wagman, D.D.; and Prosen, E.J.; *Natl. Bur. Standards;* **1958**; *6252*; 226.

107 Shirai, K.; Dekura, H.; Masago, A.; *Journal of Physics: Conference Series*; **2009,** *176,* 012001.

108 Eremets, M. I.; Sruzhkin, V. V.; Mao, H. and Hemley, R. J.; *Science;* **2001,** *293,* 272.

109 McDonald, R.A.; and Stull, D.R.; *J. Chem. Eng. Data;* **1962**, *7;* (1); 84 .

110 Stout, N.D.; Mar, R.W.; and Boo, W.O.; *High Temperature Science*; **1973**; *5*; 241.

111 Lundstrom, T.; Lonnberg, B.; and Bauer, J.; *Journal of Alloys and Compounds*; **1998**; *267*; 54.

112 Ma, Y.; Prewitt, C.T.; Zou, G.; Mao, H.; and Hemley, R.J.; *Physical Review B*; **2003**; *67*; 174116.

113 Werheit, H.; *Japanese Journal of Applied Physics*; **1994**; *10*; 66 .

Appendix A : *α*-boron

Sample Label	20110414 H-Sample 444	MASS:Sample Mass (mg)	9.45

T /K	C_P /J mol^{-1} K^{-1}	T /K	C_P /J mol^{-1} K^{-1}	T /K	C_P /J mol^{-1} K^{-1}
272.72	9.49	320.25	11.3	367.35	13.1
272.18	9.47	320.28	11.3	367.47	13.1
272.18	9.45	320.30	11.3	367.48	13.1
296.17	10.4	344.36	12.1	391.48	13.9
296.26	10.4	344.40	12.1	391.54	13.9
296.28	10.4	344.41	12.2	391.52	13.9

Sample Label	20110603 N-Sample 711	MASS:Sample Mass (mg)	9.83

T /K	C_P /J mol^{-1} K^{-1}	T /K	C_P /J mol^{-1} K^{-1}	T /K	C_P /J mol^{-1} K^{-1}
0.37	0.000000974	1.45	0.0000136	5.89	0.00102
0.37	0.00000165	1.45	0.0000127	5.89	0.00102
0.37	0.00000566	1.45	0.0000137	5.89	0.00108
0.41	0.00000175	1.63	0.0000197	6.61	0.00150
0.41	0.00000197	1.63	0.0000167	6.62	0.00140
0.42	0.00000184	1.63	0.0000185	6.62	0.00143
0.46	0.00000204	1.83	0.0000263	7.44	0.00199
0.46	0.00000648	1.83	0.0000246	7.44	0.00197
0.46	0.00000188	1.83	0.0000255	7.45	0.00202
0.51	0.00000254	2.05	0.0000354	8.36	0.00272
0.51	0.00000249	2.05	0.0000352	8.37	0.00272
0.51	0.00000204	2.05	0.0000397	8.37	0.00277
0.58	0.00000236	2.31	0.0000527	9.40	0.00371
0.58	0.00000257	2.31	0.0000520	9.40	0.00369
0.58	0.00000223	2.31	0.0000576	9.41	0.00381
0.64	0.00000280	2.60	0.0000761	10.58	0.00516
0.65	0.00000286	2.60	0.0000770	10.58	0.00539
0.65	0.00000314	2.60	0.0000842	10.59	0.00518
0.72	0.00000418	2.92	0.000116	11.89	0.00714
0.72	0.00000385	2.92	0.000116	11.90	0.00723
0.72	0.00000249	2.92	0.000122	11.90	0.00712
0.81	0.00000372	3.28	0.000171	13.37	0.00979
0.81	0.00000650	3.28	0.000170	13.38	0.0100
0.81	0.00000482	3.29	0.000177	13.38	0.0096
0.91	0.00000554	3.69	0.000245	15.05	0.0133
0.91	0.00000439	3.69	0.000247	15.05	0.0136
0.91	0.00000659	3.69	0.000266	15.06	0.0132
1.02	0.00000840	4.14	0.000369	16.92	0.0176
1.02	0.00000625	4.14	0.000370	16.92	0.0176
1.02	0.00000595	4.15	0.000372	16.93	0.0183
1.15	0.00000907	4.66	0.000519	19.03	0.0241
1.15	0.00000725	4.66	0.000507	19.03	0.0243
1.15	0.00000635	4.66	0.000536	19.05	0.0254
1.29	0.00000977	5.24	0.000744	21.33	0.0336
1.29	0.00000911	5.24	0.000727	21.34	0.0331
1.29	0.0000103	5.24	0.000738	21.36	0.0331

Sample Label	20110603 N-Sample 711	MASS:Sample Mass (mg)	9.83

T /K	C_P /J mol^{-1} K^{-1}	T /K	C_P /J mol^{-1} K^{-1}	T /K	C_P /J mol^{-1} K^{-1}
24.02	0.0462	45.25	0.179	53.39	0.264
24.04	0.0446	46.23	0.189	53.41	0.260
24.05	0.0440	46.24	0.191	54.39	0.275
26.98	0.0598	46.27	0.188	54.41	0.272
26.99	0.0586	47.25	0.199	54.42	0.276
27.02	0.0578	47.27	0.200	55.40	0.286
30.28	0.0763	47.29	0.197	55.43	0.288
30.33	0.0764	48.27	0.208	55.44	0.284
30.37	0.0767	48.29	0.210	56.43	0.298
34.19	0.100	48.31	0.207	56.46	0.300
34.20	0.0980	49.28	0.218	56.46	0.295
34.21	0.0973	49.30	0.219	57.47	0.310
38.46	0.129	49.32	0.217	57.47	0.312
38.48	0.127	50.32	0.230	57.51	0.312
38.48	0.126	50.34	0.231	58.48	0.324
43.29	0.162	50.36	0.231	58.50	0.321
43.32	0.166	51.33	0.239	58.51	0.325
43.33	0.163	51.35	0.241	59.50	0.335
44.20	0.171	51.37	0.238	59.52	0.337
44.21	0.173	52.34	0.250	59.54	0.333
44.23	0.171	52.37	0.252	60.57	0.346
45.21	0.180	52.39	0.249	60.64	0.345
45.23	0.181	53.36	0.262		

Sample Label	20110709 N-Sample 444	MASS:Sample Mass (mg)	10.25

T /K	C_P /J mol^{-1} K^{-1}	T /K	C_P /J mol^{-1} K^{-1}	T /K	C_P /J mol^{-1} K^{-1}
44.12	0.145	96.14	1.03	213.13	6.32
44.12	0.145	96.17	1.03	235.32	7.53
49.44	0.190	96.24	1.03	235.47	7.51
49.46	0.190	101.04	1.18	235.49	7.51
49.47	0.191	101.04	1.18	257.72	8.57
55.43	0.252	101.08	1.18	257.84	8.58
55.44	0.252	123.42	1.95	257.89	8.56
55.46	0.254	123.43	1.95	280.08	9.61
62.13	0.340	123.44	1.95	280.24	9.54
62.14	0.340	145.55	2.88	280.24	9.52
62.16	0.343	145.78	2.90	302.46	10.3
69.64	0.447	145.79	2.89	302.59	10.2
69.68	0.448	167.97	3.97	302.59	10.2
69.68	0.447	168.19	3.98		
77.53	0.598	168.20	3.98		
77.54	0.597	190.50	5.16		
77.57	0.600	190.68	5.16		
86.29	0.784	190.69	5.15		
86.29	0.784	212.99	6.30		
86.34	0.787	213.08	6.32		

Sample Label	20110709 N-Sample 444	MASS:Sample Mass (mg)	10.25

T /K	C_P /J mol^{-1} K^{-1}	T /K	C_P /J mol^{-1} K^{-1}	T /K	C_P /J mol^{-1} K^{-1}
44.12	0.145	96.14	1.03	213.13	6.32
44.12	0.145	96.17	1.03	235.32	7.53
49.44	0.190	96.24	1.03	235.47	7.51
49.46	0.190	101.04	1.18	235.49	7.51
49.47	0.191	101.04	1.18	257.72	8.57
55.43	0.252	101.08	1.18	257.84	8.58
55.44	0.252	123.42	1.95	257.89	8.56
55.46	0.254	123.43	1.95	280.08	9.61
62.13	0.340	123.44	1.95	280.24	9.54
62.14	0.340	145.55	2.88	280.24	9.52
62.16	0.343	145.78	2.90	302.46	10.3
69.64	0.447	145.79	2.89	302.59	10.2
69.68	0.448	167.97	3.97	302.59	10.2
69.68	0.447	168.19	3.98		
77.53	0.598	168.20	3.98		
77.54	0.597	190.50	5.16		
77.57	0.600	190.68	5.16		
86.29	0.784	190.69	5.15		
86.29	0.784	212.99	6.30		
86.34	0.787	213.08	6.32		

Sample Label	20110714 N-Sample 451	MASS:Sample Mass (mg)	10.18

T /K	C_P /J mol^{-1} K^{-1}	T /K	C_P /J mol^{-1} K^{-1}	T /K	C_P /J mol^{-1} K^{-1}
31.20	0.0752	74.83	0.584	181.72	4.67
35.31	0.101	74.83	0.584	181.88	4.67
35.33	0.104	84.77	0.790	181.89	4.69
35.34	0.101	84.82	0.794	201.88	5.72
40.03	0.135	84.82	0.793	202.06	5.72
40.05	0.135	96.04	1.07	202.07	5.70
40.06	0.134	96.10	1.08	222.03	6.77
45.37	0.177	96.11	1.07	222.22	6.77
45.38	0.176	101.18	1.22	222.24	6.76
45.39	0.177	101.19	1.22	242.18	7.83
51.41	0.236	101.20	1.22	242.37	7.79
51.42	0.234	121.24	1.90	242.37	7.78
51.43	0.235	121.37	1.91	262.23	8.79
58.25	0.317	121.38	1.91	262.42	8.74
58.26	0.315	141.41	2.71	262.42	8.73
58.27	0.317	141.54	2.72	282.50	9.73
66.02	0.427	141.55	2.72	282.65	9.68
66.02	0.429	161.57	3.64	282.66	9.66
66.04	0.428	161.71	3.67	302.66	10.5
74.79	0.582	161.73	3.67	302.79	10.4
				302.79	10.4

Appendix B: β-boron

Sample Label	2011113 - 5	IASS:Sample Mass (mg	5.26

T /K	C_P /J mol^{-1} K^{-1}	T /K	C_P /J mol^{-1} K^{-1}	T /K	C_P /J mol^{-1} K^{-1}
254.20	9.16	307.35	11.7	355.91	13.6
254.23	9.17	307.43	11.7	356.05	13.6
254.41	9.17	307.45	11.7	356.06	13.6
271.65	10.1	325.17	12.4	373.40	14.4
271.77	10.1	325.24	12.4	373.58	14.3
271.79	10.0	325.24	12.4	373.58	14.3
289.54	10.9	343.03	13.1	390.94	15.0
289.64	10.9	343.09	13.1	391.08	14.9
289.65	10.9	343.09	13.1	391.08	14.9

Sample Label	20110127 - 15	MASS:Sample Mass (mg)	14.95

T /K	C_P /J mol^{-1} K^{-1}	T /K	C_P /J mol^{-1} K^{-1}	T /K	C_P /J mol^{-1} K^{-1}
49.96	0.123	96.91	1.06	203.55	6.36
49.96	0.124	96.91	1.06	203.60	6.36
49.96	0.123	96.95	1.06	203.64	6.36
55.79	0.180	102.02	1.22	223.82	7.57
55.80	0.181	102.04	1.22	223.86	7.56
55.80	0.179	102.11	1.23	223.87	7.55
62.31	0.266	122.36	2.02	244.07	8.66
62.31	0.266	122.38	2.01	244.08	8.66
62.31	0.268	122.45	2.03	244.10	8.67
69.60	0.375	142.70	2.97	264.33	9.74
69.60	0.375	142.73	2.97	264.35	9.75
69.61	0.379	142.81	2.99	264.37	9.75
77.71	0.540	162.98	4.05	284.50	10.8
77.72	0.541	163.02	4.05	284.59	10.8
77.72	0.546	163.10	4.05	284.61	10.8
86.78	0.757	183.27	5.21	304.87	11.7
86.79	0.758	183.32	5.20	304.88	11.7
86.81	0.764	183.39	5.20	305.29	11.7

Sample Label	20110207 - 20	MASS:Sample Mass (mg)	20.05

T /K	C_P /J mol^{-1} K^{-1}	T /K	C_P /J mol^{-1} K^{-1}	T /K	C_P /J mol^{-1} K^{-1}
37.09	0.0395	87.14	0.758	214.81	7.03
41.28	0.0580	87.18	0.764	214.86	7.02
41.28	0.0574	96.94	1.05	214.90	7.02
41.30	0.0573	96.95	1.05	237.30	8.36
45.94	0.0854	96.98	1.05	237.33	8.35
45.95	0.0863	102.07	1.21	237.34	8.34
45.96	0.0854	102.09	1.21	259.81	9.56
51.12	0.126	102.22	1.22	259.82	9.55
51.13	0.126	124.66	2.11	259.84	9.57
51.13	0.126	124.72	2.11	282.26	10.7
63.28	0.270	124.86	2.12	282.31	10.7
63.28	0.269	147.23	3.20	282.33	10.7
63.31	0.272	147.28	3.20	304.82	11.8
70.42	0.384	147.40	3.21	304.83	11.8
70.43	0.384	169.78	4.43	304.83	11.4
70.45	0.387	169.83	4.43	304.84	11.4
78.34	0.544	169.93	4.43	305.34	11.8
78.34	0.545	192.29	5.73	305.36	11.4
78.37	0.548	192.33	5.73		
87.14	0.758	192.42	5.73		

Sample Label	20110223 - 35	MASS:Sample Mass (mg)	35.7

T /K	C_P /J mol^{-1} K^{-1}	T /K	C_P /J mol^{-1} K^{-1}	T /K	C_P /J mol^{-1} K^{-1}
2.53	0.000322	9.13	0.000961	32.90	0.0274
2.53	0.000327	10.15	0.00121	32.91	0.0277
2.53	0.000327	10.16	0.00122	36.60	0.0391
2.81	0.000316	10.16	0.00122	36.60	0.0390
2.82	0.000303	11.30	0.00155	36.62	0.0393
2.82	0.000316	11.30	0.00155	40.75	0.0561
3.13	0.000307	11.30	0.00156	40.76	0.0562
3.13	0.000306	12.57	0.00198	40.79	0.0567
3.13	0.000306	12.57	0.00198	45.33	0.0820
3.49	0.000306	12.58	0.00198	45.34	0.0821
3.49	0.000296	13.99	0.00254	45.36	0.0826
3.49	0.000296	14.00	0.00254	50.44	0.120
3.89	0.000309	14.00	0.00255	50.45	0.120
3.89	0.000312	15.57	0.00333	50.49	0.121
3.89	0.000306	15.57	0.00333	56.13	0.177
4.32	0.000315	15.58	0.00334	56.14	0.177
4.32	0.000316	17.33	0.00436	56.17	0.178
4.32	0.000313	17.33	0.00437	62.46	0.256
5.35	0.000386	17.34	0.00438	62.46	0.256
5.35	0.000386	19.28	0.00577	62.50	0.258
5.35	0.000390	19.29	0.00576	69.49	0.367
5.95	0.000436	19.30	0.00578	69.50	0.367
5.95	0.000443	21.47	0.00774	69.54	0.369
5.95	0.000445	21.47	0.00772	77.31	0.522
6.63	0.000519	21.48	0.00777	77.31	0.522
6.63	0.000520	23.88	0.0104	77.37	0.524
6.63	0.000521	23.88	0.0103	85.98	0.731
7.37	0.000627	23.90	0.0104	85.98	0.732
7.37	0.000627	26.56	0.0142	86.07	0.732
7.38	0.000628	26.57	0.0143	95.63	1.01
8.20	0.000772	26.58	0.0142	95.64	1.01
8.21	0.000764	29.56	0.0197	95.74	1.01
8.21	0.000771	29.57	0.0193	100.47	1.18
9.13	0.000962	29.58	0.0200	100.47	1.18

Sample Label	He - 3	MASS:Sample Mass (mg)	35.64

T /K	C_P /J mol^{-1} K^{-1}	T /K	C_P /J mol^{-1} K^{-1}	T /K	C_P /J mol^{-1} K^{-1}
0.44	0.000141	1.00	0.000258	2.40	0.000329
0.44	0.0000375	1.00	0.000257	2.40	0.000326
0.45	0.000173	1.01	0.000260	2.56	0.000318
0.46	0.000132	1.07	0.000255	2.57	0.000313
0.46	0.000126	1.07	0.000280	2.57	0.000314
0.47	0.000130	1.07	0.000265	2.74	0.000312
0.47	0.000168	1.14	0.000282	2.75	0.000311
0.49	0.000131	1.15	0.000278	2.75	0.000311
0.51	0.000138	1.16	0.000301	2.94	0.000305
0.51	0.000132	1.22	0.000305	2.94	0.000313
0.52	0.000183	1.22	0.000312	2.94	0.000311
0.54	0.000164	1.23	0.000305	3.14	0.000307
0.54	0.000127	1.31	0.000321	3.14	0.000305
0.56	0.000145	1.32	0.000309	3.14	0.000306
0.56	0.000163	1.32	0.000281	3.36	0.000305
0.56	0.000121	1.41	0.000327	3.36	0.000299
0.61	0.000148	1.41	0.000326	3.37	0.000302
0.61	0.000145	1.41	0.000328	3.60	0.000303
0.61	0.000145	1.50	0.000327	3.60	0.000303
0.63	0.000177	1.50	0.000310	3.60	0.000299
0.64	0.000175	1.50	0.000346	3.86	0.000308
0.65	0.000163	1.60	0.000354	3.86	0.000303
0.68	0.000165	1.60	0.000351	3.86	0.000304
0.68	0.000162	1.61	0.000341	4.13	0.000310
0.70	0.000170	1.72	0.000352	4.13	0.000313
0.72	0.000181	1.72	0.000347	4.13	0.000311
0.72	0.000169	1.72	0.000347	4.42	0.000316
0.72	0.000171	1.83	0.000345	4.42	0.000319
0.77	0.000191	1.83	0.000348	4.42	0.000313
0.78	0.000196	1.83	0.000343	4.73	0.000330
0.78	0.000185	1.95	0.000345	4.73	0.000335
0.82	0.000201	1.95	0.000345	4.73	0.000332
0.84	0.000212	1.96	0.000340	5.05	0.000354
0.84	0.000223	2.10	0.000343	5.05	0.000350
0.88	0.000218	2.10	0.000344	5.05	0.000356
0.88	0.000217	2.10	0.000341		
0.88	0.000226	2.23	0.000333		
0.94	0.000236	2.24	0.000333		
0.95	0.000246	2.24	0.000333		

Sample Label	20110119 - 35	MASS:Sample Mass (mg)	35.64

T /K	C_P /J mol^{-1} K^{-1}	T /K	C_P /J mol^{-1} K^{-1}	T /K	C_P /J mol^{-1} K^{-1}
2.03	0.000344	7.07	0.000488	27.59	0.0143
2.03	0.000343	7.92	0.000585	27.60	0.0145
2.03	0.000343	7.92	0.000588	30.89	0.0206
2.27	0.000334	7.92	0.000592	30.91	0.0208
2.27	0.000333	8.87	0.000736	30.92	0.0208
2.27	0.000330	8.88	0.000737	34.61	0.0300
2.54	0.000317	8.88	0.000745	34.61	0.0300
2.54	0.000320	9.94	0.000929	34.63	0.0303
2.54	0.000321	9.94	0.000931	38.77	0.0450
2.85	0.000316	9.94	0.000936	38.78	0.0449
2.85	0.000301	11.13	0.00120	38.79	0.0467
2.85	0.000303	11.13	0.00120	43.42	0.0673
3.19	0.000308	11.14	0.00120	43.43	0.0673
3.20	0.000298	12.46	0.00157	43.45	0.0681
3.20	0.000297	12.47	0.00157	48.65	0.101
3.58	0.000286	12.47	0.00159	48.66	0.101
3.58	0.000290	13.96	0.00209	48.69	0.102
3.58	0.000290	13.97	0.00209	54.48	0.153
4.00	0.000298	13.97	0.00209	54.50	0.154
4.00	0.000307	15.64	0.00277	54.53	0.155
4.01	0.000294	15.64	0.00277	61.04	0.229
4.49	0.000314	15.65	0.00281	61.05	0.229
4.49	0.000312	17.52	0.00377	61.08	0.231
4.49	0.000295	17.52	0.00378	68.38	0.338
5.03	0.000326	17.53	0.00383	68.39	0.337
5.03	0.000336	19.63	0.00517	68.42	0.340
5.04	0.000328	19.63	0.00519	76.60	0.491
5.63	0.000375	19.64	0.00517	76.61	0.491
5.64	0.000350	21.99	0.00710	76.67	0.493
5.64	0.000373	21.99	0.00712	85.80	0.699
6.31	0.000420	22.01	0.00719	85.81	0.700
6.31	0.000416	24.63	0.0100	85.91	0.700
6.32	0.000409	24.63	0.0100	96.11	0.988
7.05	0.000485	24.65	0.0101	96.12	0.987
7.06	0.000485	27.58	0.0143	96.21	0.989

Sample Label	20110722 - 35	MASS:Sample Mass (mg)	35.64

T /K	C_P /J mol^{-1} K^{-1}	T /K	C_P /J mol^{-1} K^{-1}	T /K	C_P /J mol^{-1} K^{-1}
2.40	0.000324	6.64	0.000451	21.71	0.00696
2.40	0.000330	7.86	0.000590	21.73	0.00715
2.40	0.000330	7.86	0.000592	25.70	0.0115
2.85	0.000299	7.87	0.000597	25.71	0.0115
2.85	0.000306	9.32	0.000838	25.73	0.0118
2.85	0.000302	9.32	0.000833	30.44	0.0197
3.37	0.000300	9.33	0.000842	30.45	0.0196
3.37	0.000303	11.04	0.00121	30.48	0.0201
3.37	0.000292	11.04	0.00120	36.04	0.0355
3.99	0.000302	11.06	0.00120	36.05	0.0353
3.99	0.000291	13.08	0.00179	36.07	0.0354
3.99	0.000290	13.08	0.00179	42.65	0.0635
4.73	0.000310	13.10	0.00182	42.72	0.0628
4.73	0.000319	15.49	0.00278	42.73	0.0661
4.73	0.000318	15.49	0.00279	50.42	0.116
5.61	0.000371	15.51	0.00281	50.45	0.119
5.61	0.000372	18.33	0.00437	50.52	0.117
5.62	0.000374	18.34	0.00437		
6.62	0.000450	18.36	0.00444		
6.63	0.000447	21.70	0.00696		

Sample Label	20110711 - 37	MASS:Sample Mass (mg)	37.57

T /K	C_P /J mol^{-1} K^{-1}	T /K	C_P /J mol^{-1} K^{-1}	T /K	C_P /J mol^{-1} K^{-1}
2.02	0.0000528	11.11	0.00134	61.05	0.237
2.02	0.0000536	11.11	0.00133	68.35	0.341
2.02	0.0000539	12.44	0.00180	68.35	0.341
2.26	0.0000570	12.45	0.00179	68.40	0.343
2.27	0.0000572	12.45	0.00180	76.55	0.499
2.27	0.0000566	13.94	0.00243	76.55	0.499
2.54	0.0000591	13.94	0.00242	76.62	0.502
2.54	0.0000583	13.94	0.00244	85.73	0.710
2.54	0.0000584	15.62	0.00326	85.73	0.712
2.84	0.0000643	15.63	0.00326	85.81	0.714
2.84	0.0000633	15.63	0.00326	96.06	1.00
2.84	0.0000656	17.50	0.00439	96.06	1.00
3.18	0.0000690	17.51	0.00439	96.07	1.00
3.19	0.0000681	17.51	0.00440	101.11	1.16
3.19	0.0000685	19.62	0.00594	101.12	1.17
3.57	0.0000862	19.62	0.00594	101.27	1.17
3.57	0.0000848	19.64	0.00596	121.27	1.94
3.57	0.0000793	21.96	0.00810	121.28	1.94
3.99	0.000108	21.97	0.00809	121.46	1.94
4.00	0.000110	21.97	0.00812	141.44	2.88
4.00	0.000104	24.60	0.0112	141.46	2.88
4.48	0.000131	24.60	0.0112	141.67	2.88
4.48	0.000137	24.61	0.0113	161.59	3.95
4.48	0.000122	27.56	0.0155	161.60	3.95
5.02	0.000182	27.56	0.0156	161.79	3.95
5.02	0.000174	27.57	0.0157	181.74	5.10
5.02	0.000165	30.87	0.0221	181.75	5.10
5.62	0.000227	30.88	0.0222	181.91	5.10
5.62	0.000230	30.88	0.0223	201.91	6.25
5.62	0.000222	34.58	0.0318	201.91	6.26
6.31	0.000325	34.59	0.0317	202.03	6.27
6.31	0.000310	34.60	0.0329	222.04	7.45
6.31	0.000313	38.73	0.0467	222.05	7.45
7.04	0.000408	38.74	0.0467	222.16	7.46
7.05	0.000400	38.75	0.0471	242.13	8.58
7.05	0.000403	43.39	0.0694	242.14	8.58
7.90	0.000551	43.40	0.0695	242.20	8.58
7.91	0.000554	43.43	0.0701	262.24	9.68
7.91	0.000554	48.61	0.104	262.25	9.68
8.85	0.000741	48.63	0.104	262.27	9.68
8.85	0.000736	48.66	0.105	282.33	10.7
8.85	0.000742	54.47	0.157	282.34	10.7
9.92	0.000992	54.48	0.157	282.35	10.7
9.92	0.000992	54.52	0.159	302.41	11.7
9.93	0.000989	61.01	0.235	302.43	11.7
11.10	0.00134	61.02	0.235	302.44	11.7

Sample Label	20110716 - 31	MASS:Sample Mass (mg)	31.62

T /K	C_P /J mol^{-1} K^{-1}	T /K	C_P /J mol^{-1} K^{-1}	T /K	C_P /J mol^{-1} K^{-1}
2.55	0.0000550	48.64	0.0993	141.54	2.83
2.55	0.0000539	48.66	0.0993	141.54	2.83
2.55	0.0000550	48.67	0.100	141.70	2.83
2.85	0.0000566	54.49	0.150	161.72	3.88
2.85	0.0000574	54.51	0.150	161.72	3.88
2.86	0.0000555	54.52	0.152	161.85	3.89
3.19	0.0000675	61.05	0.225	181.88	5.01
3.20	0.0000680	61.06	0.225	181.88	5.01
3.20	0.0000644	61.09	0.227	181.99	5.02
24.63	0.00989	68.39	0.332	202.04	6.17
24.63	0.00990	68.40	0.332	202.04	6.17
24.64	0.00997	68.43	0.335	202.16	6.17
27.58	0.0141	76.61	0.483	222.19	7.34
27.59	0.0141	76.61	0.485	222.20	7.34
27.59	0.0142	76.64	0.487	222.28	7.34
30.90	0.0203	85.80	0.693	242.33	8.47
30.91	0.0201	85.82	0.691	242.34	8.47
30.91	0.0205	85.87	0.697	242.38	8.46
34.61	0.0293	96.11	0.977	262.45	9.54
34.62	0.0294	96.11	0.978	262.46	9.54
34.62	0.0295	96.12	0.978	262.47	9.54
38.76	0.0438	101.17	1.13	282.57	10.6
38.78	0.0439	101.17	1.14	282.59	10.6
38.78	0.0442	101.30	1.14	282.59	10.6
43.43	0.0657	121.37	1.90	302.70	11.5
43.44	0.0658	121.37	1.90	302.71	11.5
43.47	0.0664	121.53	1.90	302.71	11.5

Sample Label	20110723 - 31	MASS:Sample Mass (mg)	31.62

T /K	C_P /J mol^{-1} K^{-1}	T /K	C_P /J mol^{-1} K^{-1}	T /K	C_P /J mol^{-1} K^{-1}
2.53	0.0000573	27.40	0.0144	101.08	1.16
2.53	0.0000567	27.41	0.0144	101.09	1.16
2.53	0.0000555	27.42	0.0146	101.18	1.16
2.86	0.0000608	31.05	0.0218	121.23	1.93
2.86	0.0000611	31.05	0.0216	121.24	1.93
2.86	0.0000601	31.07	0.0217	121.25	1.93
3.25	0.0000682	35.21	0.0322	141.11	2.84
3.25	0.0000684	35.22	0.0322	141.35	2.86
3.25	0.0000694	35.22	0.0326	141.37	2.86
3.67	0.0000826	39.91	0.0504	161.32	3.92
3.68	0.0000816	39.92	0.0504	161.56	3.93
3.68	0.0000809	39.94	0.0520	161.57	3.92
4.17	0.000111	45.26	0.0790	181.44	5.05
4.17	0.000107	45.27	0.0790	181.66	5.06
4.17	0.000101	45.31	0.0797	181.67	5.07
4.73	0.000141	51.29	0.125	201.68	6.19
4.73	0.000138	51.30	0.125	201.80	6.24
5.36	0.000194	51.35	0.126	201.84	6.20
14.62	0.00247	58.15	0.196	221.69	7.27
14.62	0.00248	58.17	0.196	221.82	7.36
14.63	0.00249	58.21	0.198	221.87	7.31
16.58	0.00346	65.93	0.300	242.03	8.51
16.58	0.00346	65.94	0.300	242.03	8.51
16.59	0.00347	66.00	0.302	242.04	8.51
18.80	0.00489	74.75	0.459	262.12	9.57
18.80	0.00490	74.76	0.458	262.23	9.58
18.81	0.00494	74.83	0.462	262.23	9.58
21.32	0.00697	84.71	0.682	282.14	10.6
21.32	0.00697	84.71	0.682	282.23	10.6
21.33	0.00703	84.80	0.685	282.23	10.6
24.16	0.00993	96.04	0.993	302.40	11.6
24.17	0.00997	96.05	0.992	302.45	11.5
24.19	0.0100	96.05	0.993	302.45	11.6